

# 1 **Coupled Hydrological and Biogeochemical Modelling of Nitrogen** 2 **Transport in the Karst Critical Zone**

3 Zhicai Zhang<sup>1,3,7</sup>, Xi Chen<sup>2\*</sup>, Qinbo Cheng<sup>3</sup>, Siliang Li<sup>2</sup>, Fujun Yue<sup>2,5</sup>, Tao Peng<sup>4</sup>, Susan  
4 Waldron<sup>5</sup>, David Oliver<sup>6</sup>, Chris Soulsby<sup>7</sup>

5 <sup>1</sup>State Key Laboratory of Hydrology-Water Resources and Hydraulic Engineering, Hohai University, Nanjing  
6 210098, China

7 <sup>2</sup>Institute of Surface-Earth System Science, Tianjin University, Tianjin 300072, China

8 <sup>3</sup>College of Hydrology and Water Resources, Hohai University, Nanjing 210098, China

9 <sup>4</sup>Institute of Geochemistry Chinese Academy of Sciences, Guiyang, 550081, China

10 <sup>5</sup>School of Geographical and Earth Sciences, University of Glasgow, Glasgow G12 8QQ, United Kingdom

11 <sup>6</sup>Biological & Environmental Sciences, Faculty of Natural Sciences, University of Stirling, Stirling FK9 4LA,  
12 United Kingdom

13 <sup>7</sup>School of Geosciences, University of Aberdeen, Aberdeen AB24 3UF, United Kingdom  
14  
15

16 **Abstract** Transport of nitrogen (N) in karst areas is more complex than in non-karst areas due  
17 to marked heterogeneity of hydrodynamic behaviour in the karst critical zone. Here, we  
18 present a novel, distributed, coupled hydrological-biogeochemical model that can simulate  
19 water and nitrogen transport in the critical zone of karst catchments. This new model was  
20 calibrated using integrated hydrometric, water stable isotope, and nitrogen-N concentration  
21 data at the outflow of Houzhai catchment in Guizhou province of Southwest China.  
22 Hydrological dynamics appears to control N load from the study catchment. Combining flow  
23 discharge and water stable isotopes significantly constrained model parameterisation and  
24 mitigate the equifinality effects of parameters on the simulated results. Karst geomorphology  
25 and land use have functional effects on spatiotemporal variations of hydrological processes  
26 and nitrogen transport. In the study catchment, agricultural fertilizer was the largest input  
27 source of N, accounting for 86 % of the total. Plant uptake consumed about 45 % of inputs,  
28 primarily in the low-lying valley bottom areas and the plain covered by relatively thick soils.

29 Thus, a large amount of N released from soil reservoirs to the epikarst (via fractures or  
30 sinkholes) is then exported to the underground channel in the limestone area to the south. This  
31 N draining into groundwater could lead to extensive, potentially long-term contamination of  
32 the karst system. Therefore, improving the efficiency of fertilization and agricultural  
33 management in valleys/depressions is an urgent need to reduce N losses and contamination  
34 risk.

35

## 36 **1. Introduction**

37 Carbonate bedrock is a significant continental surface, comprising ~12 % of ice-free land  
38 and providing water resources for about 25 % of the Earth's population (Ford and Williams,  
39 1989). The southwest China karst region is one of the largest globally continuous karst areas,  
40 covering  $\sim 540 \times 10^3 \text{ km}^2$  over eight provinces. Agro-forestry and mineral extraction dominate  
41 land use, with subsistence-agriculture where soils exist (terraced gentler hillslopes/valley  
42 floors), and forest in uncultivated steeper mountains. From ~1950-1980 deforestation for  
43 creating cultivation space caused accelerated soil erosion, a changed hydrological balance  
44 and, shaped by agricultural practices, poorer water quality. Anthropogenic N fluxes have also  
45 been increasing as a result of population growth, agricultural intensification, fossil  
46 fuel-related acid deposition in industrialised- and agriculturally-intensified regions. Moreover,  
47 significant soil percolation and subsequent rapid preferential flow in the critical zone provides  
48 limited buffering for contaminant attenuation before re-emergence. It is therefore important to  
49 understand what controls water quality, and the source and attenuation of contaminants in this  
50 sensitive landscape. Models can help understanding of how nitrogen is cycled and transported

51 and the key factors and processes that control its dynamics. Modelling results provide  
52 quantitative estimates of how a system will respond to changes in pollutant inputs to aid  
53 environmental management (Ranzini et al., 2007).

54 The transfers of N in karst areas are more complex than those in non-karst areas because  
55 of the marked spatial heterogeneity of hydrodynamic behaviour. Lumped parameter models  
56 conceptualising reservoirs of the critical zone in series and/or parallel have been popularly  
57 used to simulate flow and nitrate movements and [its](#) biogeochemical reaction in karst areas  
58 (Husic et al., 2019). However, these lumped models lack functionality in relation to the spatial  
59 heterogeneity of hydrological-N processes characterising karst landforms, geology and land  
60 cover. Distributed hydrological-nutrient models, like SWAT (Arnold et al., 1998), have been  
61 widely used to simulate hydrological and nutrient responses to changes of land surface  
62 conditions. Expanding the grid-pattern hydrological model functions using process-oriented  
63 biogeochemical modules, such as the DeNitrification-DeComposition (DNDC) module (Li et  
64 al., 2000), facilitates comprehensive simulation of nitrogen transformation, vertical movement  
65 of water and nitrogen in soils and effluxes of carbon and nitrogen gases (Ferrant et al., 2011;  
66 Zhang et al., 2016, 2017a; Zhang et al., 2018). However, these models are developed for  
67 matrix flow systems therefore cannot be directly applied in karst areas. In karst areas, the high  
68 permeability of rock fractures leads to considerable changes in water storage and water age by  
69 facilitating mixing of new and old water during rainfall events (Zhang et al., 2019).  
70 Channelled flow in sub-surface conduits also exchanges reversibly with small fractures in the  
71 surrounding matrix depending on the hydraulic gradient between them (Hartmann et al.,  
72 2014). Sinkholes are special features in karst areas, which receive both [diffused](#) and

73 concentrated autogenic recharge, and then drain through a shaft or an underlying solution  
74 conduit (Tihansky, 1999). Therefore, over different, linked porous media, biogeochemical  
75 processing capacities can vary drastically (Jones and Smart, 2005; Opsahl et al., 2017; Yue et  
76 al., 2015). Until now, only a few models can appropriately delineate the unique  
77 hydrological-nitrogen cycle of karst systems.

78 A particular challenge in coupled hydrological-biogeochemical modelling is the  
79 increased risk of equifinality as model parameters increase (Zhang et al., 2016; Zhang and  
80 Shao, 2018). However, recently using tracer-aided models has helped ensure robust  
81 hydrological modules in coupled models. Using water stable isotopes or other tracers (e.g.  
82 chloride) in calibration, in addition to the more commonly used target of flow, can help  
83 constrain parameterisation at the catchment scale whilst giving increased confidence of  
84 accurate process representation of runoff sources (Birkel et al, 2015). Tracer-aided models can  
85 also strengthen conceptualisation of hydrological functions and transport of water particles, in  
86 terms of water age, dominant flow paths and hydrological connectivity in different model  
87 compartments. Such quantitative hydrological understanding can be functionally linked to  
88 solute transport in water quality models (McDonnell and Beven, 2014; Sprenger et al., 2015).  
89 These advantages of stable isotopes have been successfully exploited in enhancing the  
90 reliability of modelling dominant hydrological processes in non-karst catchments (Soulsby et  
91 al., 2015; Piovano et al., 2018) - but the efficiency of the tracer-aided functions applied in the  
92 hydrological-biogeochemical model in karst catchments is unknown.

93 Our previous work in the Chenqi catchment, a sub-catchment of the Houzhai catchment,  
94 Guizhou province of Southwest China, has focused on a typical karst landscape and

95 associated karst critical zone architecture (Vertically, the earth critical zone refers to a  
96 permeable layer from the tops of the trees to the bottom of the groundwater. Here, karst  
97 critical zone encompasses vegetation, soils, epikarst and deep aquifer.). In this prior work, we  
98 developed a distributed hydrological model (Zhang et al. 2011). In this study, we extend this  
99 model to facilitate multi-criteria calibration based on detailed observations of water stable  
100 isotope composition; we also couple biogeochemical modules to the hydrological structure to  
101 simulate spatially distributed fluxes of N, and apply the model to the larger Houzhai  
102 catchment. We address the three questions: (1) How do interacting karst geomorphological  
103 features, such as fractures and conduits, sinkholes, and surface streams and subsurface  
104 channel, control hydrological-nitrogen processes? (2) How effective is the tracer-aided model  
105 in reducing modelling uncertainty? (3) How much N in the catchment N budget is contributed  
106 from different sources in the critical zone and from different land uses?

107

## 108 **2. Study area and Data**

### 109 *2.1. Study area and descriptions of critical zone structure*

#### 110 *2.1.1 Study area*

111 The Houzhai catchment, located in Puding County, Guizhou Province of southwest  
112 China, has an area of 73.5 km<sup>2</sup> (Fig.1). The site has a subtropical wet monsoon climate. The  
113 mean annual temperature is 20.1<sup>0</sup>C. The highest monthly average temperature is in July, and  
114 the lowest is in January. Annual precipitation is 920 mm, with a distinct summer wet season  
115 and a winter dry season. Monthly average humidity ranges from 74 % to 78 %. The lithology  
116 is ~90 % Triassic argillaceous limestone and dolomite. The elevation of the study area varies

117 from 1218 to 1565 m above sea level, high in the east and low in the west (Fig.1). The karst  
118 topography in this catchment includes many exposed funnels and sinkholes and a  
119 well-developed underground channel network. Buried karst is located in the valleys and  
120 poljes, which are surrounded by karst mountainous peaks. The east mountainous area has the  
121 typical cone and cockpit karstic geomorphology of southwest China. The cone peaks are  
122 generally 200-300 m above the adjacent sinkhole depressions while the cone surface relief  
123 and slope are much steeper.

#### 124 *2.1.2 Vegetation and soils*

125 The land use and cover in the catchment include forests (mostly a mix of trees and  
126 shrubs), cultivated fields, villages and open water (Fig.2a). The soils are classified as  
127 limestone soil, paddy soil, and yellow soil (Fig.2b). Field investigations of soil thickness  
128 and hydraulic properties have been undertaken. The soil thickness ranges 0~2.0 m,  
129 increasing from steep hillslope (0-50cm) to gentle plain areas (1-2m).

#### 130 *2.1.3 Epikarst*

131 Below soils or at the outcropping carbonate rocks, the uppermost layer of the rock is  
132 referred to as the “epikarst”. It develops close to the topographic surface through rapid  
133 dissolution (Williams, 2008). Field investigations of a rock profile in the eastern mountainous  
134 area (Fig.2c) showed that the epikarst zone underlying the thin soils is rich in fractures and  
135 conduits while density and volume of the fractures generally decrease with increasing depth  
136 from ground surface (Zhang et al., 2013). Some infiltrated water can become perched in the  
137 epikarst zone as the porosity and permeability below decline markedly (Klimchouk, 2004).  
138 The distribution of epikarst thickness across the catchment was investigated at five profiles

139 (Fig.2c) using GPR (MALA Professional Explorer (ProEx) System) with a RTA 100-MHz  
140 antenna frequency and the software of Reflexw. The radargrammes clearly identify the  
141 thickness of the weathered zone, for example, the purple colour represents a low propagation  
142 velocity of electromagnetic waves in the ground for A and B profiles, and the zone with  
143 intensive changes of colour is characterized by strong fractured rocks.

144 From these profiles and the established relationship between the epikarst thickness and  
145 terrain curvatures (Zhang et al., 2012), the epikarst thickness in the entire catchment was  
146 interpolated using a digital elevation model (DEM) data derived from the 1:10 000 digital  
147 topography map in the catchment. The generated depth of epikarst zone ranges from 7 to 28  
148 m (Fig.2c), shallower in the eastern mountains and deeper in the western plains.

#### 149 *2.1.4 Deep aquifer*

150 The aquifer system consists mainly of limestone and dolomite of the Middle Triassic  
151 Guanling Formation (Fig.2d). The degree of inclination of the strata in this formation is  
152 between 5° and 25° to the northwest. The Middle Triassic Guanling Formation can be divided  
153 into T<sub>2g</sub><sup>1</sup>, T<sub>2g</sub><sup>2</sup>, and T<sub>2g</sub><sup>3</sup> (A-B section in Fig.2d) from the oldest to the youngest according to  
154 the combined characteristics of the lithology (Yang, 2001). The karst fissures and conduits are  
155 well developed in the aquifers. In particular, dense conduits can be found in the south  
156 limestone area (Yang et al., 2001). The groundwater depth decreases from more than 10 m in  
157 the east to ~2 m in the west, following the topography (Fig 3d). The aquifer boundary is  
158 similar to the catchment boundary except in the south where less than 5% of water is lost to a  
159 neighbouring catchment through conduits (Yu et al., 1990). The catchment mean recharge  
160 coefficient (recharge amount divided by precipitation) is about 0.47 (Yu et al., 1990). A large

161 proportion of the infiltration and percolation comes from direct runoff and sinking streams  
162 (allogenic recharge from the surrounding areas) in the rain season. The aquifers mostly are  
163 unconfined, however, they are markedly heterogeneous (Yu et al., 1990), with both  
164 subsurface flow of low velocity in the matrix (small fissures and fractures) and fast flow  
165 velocity in the karst conduits. Consequently, spatio-temporal variability in the water table is  
166 extremely high (Chen et al., 2018).

#### 167 *2.1.5 Sinkhole in connection with deep aquifer*

168 Sinkholes usually develop in terrain depression areas (Kruse et al, 2006), which overlie  
169 the underground channel. In the study catchment, 47 sinkholes have been identified based on  
170 the field investigations (Fig.1). Based on a DEM, the flow direction tool in ARCGIS is used  
171 to create a direction raster that identifies the drainage area of every sinkhole in the study area  
172 (Fig.1). Fourteen sinkholes in the eastern mountainous area are identified with a total area of  
173 8.22 km<sup>2</sup>, which accounts for 11 % of the total catchment area. The smallest and largest  
174 sinkhole drainage areas are 0.17 and 1.53 km<sup>2</sup>, respectively. The total area of the 33 sinkholes  
175 in the western plain area is 1.64 km<sup>2</sup>, which accounts for only 2 % of the total catchment area.  
176 Therefore, the western sinkholes collect less storm flow compared to the eastern sinkholes  
177 (Yu et al., 1990). Additionally, the western sinkholes are mainly produced by the collapse of  
178 rocks overlying the underground channel and drain small areas. They take a similar function  
179 in receiving storm flow as the underground channel does. Therefore, among the 47 sinkholes  
180 in the catchment (Fig.1), the 14 in the east are used for flow routing and the remaining 33  
181 sinkholes in the western area are ignored.

#### 182 *2.1.6 Surface stream and underground channel*



183 The Houzhai catchment consists of a surface stream in the north and a main underground  
184 channel in the south (Fig.1). The surface stream, incised an average depth of 2 m below the  
185 ground surface, is formed in the relatively thick yellow soil in the north (Fig.2b). The surface  
186 stream is usually dry in drought periods due to the high streambed infiltration into the  
187 underlying carbonate aquifer. Only during the flood periods, does the surface stream receive  
188 storm water, which flows from two main tributaries to the Qingshan (QS) reservoir and  
189 finally to the outlet of the Houzhai River.

190 The underground channel originates in the eastern mountains where most surface and  
191 subsurface flow recharges into the underground drainage network through the eastern  
192 sinkholes. The depth of the deep flow zone (underground channel bed or catchment lower  
193 boundary) is about 20-40 m below the ground surface (Fig 3d) (Yu et al., 1990). The upper  
194 mountainous region is rich in sinkholes or funnels, which are directly linked with the  
195 underground channels, resulting in a responsive hydrograph. When the underground channel  
196 reaches the broad and flat plains in the middle and lower catchment, underground flow is  
197 more attenuated (Chen et al., 2008).

#### 198 *2.1.7 Catchment sub-division and grid-scale flow routing*

199 For grid routing of the hydrological-nitrogen model, the catchment was divided into a  
200 rectangular grid of 100 m × 100 m resolution, totalling 13,000 pixels (104 rows by 125  
201 columns). All the attributes of vegetation, soils, epikarst, and deep zone are assigned in the  
202 pixels. The surface stream network is generated automatically following the Horton ordering  
203 scheme according to terrain using ARC/INFO. The surface stream width ranges 2–8 m and  
204 the depth of the stream bed ranges 1–2.5 m. The underground channel network is manually

205 delineated in terms of field investigation of underground channel information. The  
206 underground channel width and depth are approximately 1.5 and 1 m, respectively.  
207 ARC/INFO macros are used to subdivide the surface stream and underground channel  
208 networks into reaches and to order the cascade branches for the flow routing.

## 209 *2.2. Hydrochemical observations and analysis*

210 In the Houzhai catchment, two automatic weather stations were established at Chenqi  
211 (CQ) and Laoheitan (LHT) (Fig.1) to record precipitation, air temperature, wind, radiation, air  
212 humidity and pressure. The meteorological data and underground channel discharge  
213 collection was from 1 March 2016 to 31 December 2017. The discharges of the surface  
214 stream and underground channel at the catchment outlet were measured with weirs (Fig.1).  
215 Water levels were automatically recorded by a HOBO U20 water level logger (Onset  
216 Corporation, USA) with a time interval of 15 minutes. The discharge in the surface stream  
217 was measured from 1 January 2017 to 31 December 2017.

218 Rainwater and surface stream and subsurface channel water at catchment outlets were  
219 daily sampled between 1 June 2016 and 31 December 2017. All water samples were collected  
220 in 5 ml glass vials. The stable isotope ratios of  $\delta\text{D}$  and  $\delta^{18}\text{O}$  were determined using a MAT  
221 253 laser isotope analyser (instrument precision of  $\pm 0.5\text{‰}$  for  $\delta\text{D}$  and  $\pm 0.1\text{‰}$  for  $\delta^{18}\text{O}$ ).  
222 Water stable isotope ratios are reported in the  $\delta$ -notation using the Vienna Standard Mean  
223 Ocean Water standards.  $\text{NO}_3\text{-N}$  concentrations ( $[\text{NO}_3\text{-N}]$ ) at the surface and underground  
224 channel outlets were measured using non-optical NISE sensor with a time interval of 15  
225 minutes from 1 June 2016 to 30 September 2017 (Yue et al, 2019).  $\text{NH}_4\text{-N}$  concentrations  
226 were measured several times during June ~ July 2016.

227 The discharge, isotopic and NO<sub>3</sub>-N concentrations show great variability (Fig.3). From  
228 statistical characteristics of these variables (Table 1), the mean of underground channel  
229 discharge is over double that of surface stream discharge while temporal variability of  
230 underground channel discharge is much lower than that of surface stream discharge (see CV  
231 and Mode in Table 1). The  $\delta D$  ratios of underground channel tend to be less variable than  
232 surface stream flow, implying lower influence of young waters. This is particularly apparent  
233 for heavy rainfall events (corresponding to the minimum  $\delta D$  value in Table 1) where the  
234 young water influence in the underground channel flow is much less than surface stream flow.  
235 This suggests that the isotopic responses of underground channel flow and surface stream  
236 flow to rainfall are similar in most periods, and only in the heavy rainfall periods, is the  
237 surface stream flow newer than underground channel flow.

238 In terms of mean and maximum values in Table 1, N loading mostly comes from  
239 underground channel flow but the peak flow of surface waters can carry the largest N loading.  
240 Interestingly, N loading increases linearly with discharge for both surface stream and  
241 underground channel (Fig.4), which indicates that variations of the N fluxes are directly  
242 proportional to flow. Thus, accurate simulation of hydrographs for  
243 hydrological-biogeochemical modelling is vital in this karst landscape. The local meteoric  
244 water line (LMWL) is derived from the regression between  $\delta^{18}O$  and  $\delta D$  values of daily  
245 precipitation data sampled between July 2016 and December 2017. The dual-isotope plot  
246 shows great evaporative fractionation effects on underground channel flow than surface  
247 stream (Fig.5). The lower slope of underground channel flow illustrates that groundwater in  
248 the deep zone mixes more heavy isotopes during infiltration and percolation.

249 Monthly wet deposition of  $\text{NH}_4\text{-N}$  and  $\text{NO}_3\text{-N}$  ranged from 0.2-2.6 mg/L for  $\text{NO}_3\text{-N}$  and  
250 0.42-5.8 mg/L for  $\text{NH}_4\text{-N}$ , and monthly dry N deposition was 0.26 kg/ha (Zeng, 2018).  
251 Annual fluxes and seasonal distribution of litter fall were estimated drawing on understanding  
252 from another basin in Guizhou Province with similar vegetation distributions and geographic  
253 conditions (Pi, 2017). Annual fluxes of litter fall range 1.47-3.61 t/ha<sup>yr</sup> and the C/N ratios are  
254 18.7-33.1 for forest. The non-point source inputs of N for farm land (paddy and rapeseed) are  
255 estimated to be ~270kg kg/ha<sup>yr</sup> (from field surveys by the Karst Ecosystem Research Station  
256 of the Institute of Geochemistry in Puding). Leguminous crops are the main N fixation plants,  
257 which fix N via symbiotic anaerobic microorganisms (Cheng, 2008). Therefore, for this  
258 model, it is assumed that N-fixation occurs primarily with bean crops, and from field survey  
259 in this catchment the fraction of bean crop in each pixel was set to 0.04 in the cultivated land.  
260 The rate of annual N fixation by pure stands of bean was set to 40 kg N/ ha<sup>yr</sup> (based on Smil,  
261 1999). The potential denitrification fluxes are  $6.2 \times 10^{-8}$  and  $1.3 \times 10^{-6}$  kgN/m<sup>2</sup>·h for forest and  
262 farm land, respectively (Barton et al. 1999).

263

### 264 **3. Model description and Execution**

265 The original distributed hydrology-soil-vegetation model (DHSVM) includes a two-layer  
266 Penman-Monteith formulation and a two-layer energy balance model for canopy  
267 evapotranspiration and ground snow pack, respectively. It contains a multilayer unsaturated  
268 soil model, a saturated subsurface flow model, and a grid-based overland flow routing  
269 (Wigmosta et al. 1994). The model was subsequently expanded to integrate a biogeochemical  
270 module (the DHSVM Solute Export Model, D-SEM) (Thanapakpawin, 2007). To

271 accommodate the special karst geomorphological features, like sinkholes, epikarst and deep  
 272 aquifers, Zhang et al. (2011) adapted the DHSVM structure for application in Chenqi  
 273 catchment. The vertical layers of the model are divided to represent vegetation, soils, epikarst,  
 274 and deep aquifers according to descriptions of karst structure given by Perrin et al. (2003).  
 275 The flow routing includes sinkhole functions in collecting local surface and subsurface flow  
 276 in soils and the epikarst zone, and directly connecting these with underground channel  
 277 outflow (Fig.6). In this study, the N routings are improved accordingly by conceptualising the  
 278 above karst geomorphologic functions (Fig.6), in addition to integrating the mass balance  
 279 routings and biogeochemical reaction calculations proposed by Thanapakpawin (2007).

280

### 281 3.1. Hydrological simulation

282 In the three zones of soils ( $s$ ), epikarst ( $e$ ) and deep flow zone ( $d$ ), the flow routings are  
 283 based on water balance equations for every grid cell in the catchment:

$$284 \quad \frac{d\theta_s}{dt} d_s = P_0 - P_s(\theta) - E_{to} - E_{tu} - E_s + V_e + (Q_{s,in} - Q_{s,out}) - V_s \quad (1)$$

$$285 \quad \frac{d\theta_e}{dt} d_e = P_s(\theta) - P_e(\theta) - E_{to} + V_d + (Q_{e,in} - Q_{e,out}) - V_e \quad (2)$$

$$286 \quad \frac{d\theta_d}{dt} d_d = P_e(\theta) + (Q_{d,in} - Q_{d,out}) - V_d \quad (3)$$

287 where  $\theta_n$  is soil moisture and  $d_n$  is thickness ( $n=s, e, d$ );  $P_n$  is infiltrated rainfall ( $n=0$ ) or  
 288 percolated water ( $n=s, e$ );  $E_{to}$  are  $E_{tu}$  evapotranspiration from over story( $o$ ) and understory  
 289 vegetation ( $u$ ), respectively;  $E_s$  is soil evaporation;  $Q_{n,in}$  and  $Q_{n,out}$  are subsurface flow that  
 290 passes into and out of the soil, epikarst and deep conduit flow zone, respectively;  $V_n$  is return  
 291 flow.

292 Vertical infiltration and percolation in the soil ( $P_s$ ) are estimated based on Darcy's Law

293 assuming a unit hydraulic gradient and using an equivalent hydraulic conductivity as  
 294 described by Brooks-Corey (1964) for the soils. The “cubic law” is used for estimation of  
 295 infiltration and percolation of the rock fractures in epikarst ( $P_e$ ). The spatial distributions of  
 296 the rock fractures are stochastically generated according to field investigations of fractural  
 297 characteristics, such as density, length and direction (details in Zhang et al., 2011). The  
 298 subsurface flow ( $Q_{n,in}$ ,  $Q_{n,out}$ ,  $n=s, e, d$ ) is calculated cell-by-cell in terms of hydraulic  
 299 transmissivity ( $T=Kd$ , where  $K$  is hydraulic conductivity, and  $d$  is thickness of each layer),  
 300 hydraulic gradient and the grid width and length ( $b_{cell}$  and  $L_{cell}$ ) at the grid in each flow  
 301 direction. For the cells within a sinkhole drainage area, surface flow or overland flow ( $Q_{sur}$ )  
 302 and subsurface flow ( $Q_s$  and  $Q_e$ ) directly recharge into the underground channel via the  
 303 sinkhole ( $Q_{sinkhole}$ ).

304 In the original DHSVM, flow in surface stream and the underground channel systems is  
 305 routed using a cascade of linear channel reservoirs (Wigmosta et al, 1994; Wigmosta and  
 306 Perkins, 2001). In the new adaptation of DHSVM, for the surface stream flow routing, the  
 307 lateral flow ( $Q_{surL}$ ) includes the loss of water as infiltration from the surface stream bed into  
 308 the underlying aquifer ( $Q_{inf}$ ), in addition to the gained water of overland flow ( $Q_{sur}$ ) and  
 309 subsurface flow in the soil zone ( $Q_s$ ):

$$310 \quad Q_{surL} = Q_{sur} + Q_s - Q_{inf} \quad (4)$$

$$311 \quad Q_{inf} = L_{cell} \cdot b_{cell} \cdot \alpha_{inf} \quad (5)$$

312 where  $L_{cell}$  and  $b_{cell}$  are length and width of surface stream segment in one cell, respectively.  
 313  $\alpha_{inf}$  is constant rate of the surface stream bed. For the underground channel flow routing, the  
 314 average rate of lateral flow ( $Q_{gL}$ ) includes the flows from the epikarst zone ( $Q_e$ ) and the deep

315 zone intercepted by the underground channel ( $Q_d$ ) when the cells are outside a sinkhole  
 316 drainage area:

$$317 \quad Q_{gL} = Q_e + Q_d \quad (6)$$

318 Otherwise, the lateral flow equals the sinkhole water collected ( $Q_{sinkhole}$ ):

$$319 \quad Q_{gL} = Q_{sinkhole} \quad (7)$$

### 320 3.2. Nitrogen simulation

#### 321 3.2.1. Mass balance of Nitrogen

322 Consistent with the hydrological module, the karst system is conceptualised as three  
 323 nitrogen reservoirs in the vertical dimension. The multilayer mass balance model accounts for  
 324 nitrogen dynamics in the soil, epikarst, and deep flow zones:

$$325 \quad \frac{dM_s}{dt} = M_{sur-s} - M_{s-e} - M_{s-sur} + (M_{s,in} - M_{s,out}) + \sum_{i=1}^{j_s} M_i \quad (8)$$

$$326 \quad \frac{dM_e}{dt} = M_{s-e} - M_{e-d} - M_{e-s} + (M_{e,in} - M_{e,out}) + \sum_{i=1}^{j_e} M_i \quad (9)$$

$$327 \quad \frac{dM_d}{dt} = M_{e-d} - M_{d-e} + (M_{d,in} - M_{d,out}) + \sum_{i=1}^{j_d} M_i \quad (10)$$

328 where  $M_n$  is solute mass ( $n=s, e, d$ );  $M_{n,in}$  and  $M_{n,out}$  are mass flux that passes in and out the  
 329  $n$ th zone, respectively;  $\sum_{i=1}^{j_e} M_i$  ( $j=s, e, d$ ) is biogeochemical mass; subscripts of *sur-s*, *s-sur*,  
 330 *s-e*, *e-s*, *e-d* and *d-e* represent from surface to soil layer, soil layer to surface, soil layer to  
 331 epikarst, epikarst to deep flow zone, and deep flow zone to epikarst, respectively.

332 The solute concentration in each zone can be derived according to the mass ( $M_n$ ,  $n=s, e,$   
 333  $d$ ), the water volume ( $\theta_n$ ,  $n=s,e,d$ ), and the mass fluxes that pass in and out of each zone  
 334 ( $M_{n,in} / M_{n,out}$ ,  $n=s, e, d$ ). The mass fluxes draining through sinkholes into underground  
 335 conduits ( $M_{sinkhole}$ ) are calculated from the flows collected by the sinkhole ( $M_{sinkhole}$ )  
 336 multiplied by the solute concentration of the collecting water. The model tracks and simulates

337 the solute mass/concentration for each reservoir separately. The solute mass routing in stream  
 338 channel/underground conduit is based on mass balance:

$$339 \quad M_{out} = M_{in} + \Delta M_V + \sum_{i=1}^{j_V} M_i \quad (11)$$

$$340 \quad \sum_{i=1}^{j_V} M_i = M_{loss} = \phi C_{riv\_sur} Q_{riv\_sur} \quad \text{for surface stream} \quad (12)$$

$$341 \quad \sum_{i=1}^{j_V} M_i = 0 \quad \text{for underground channel} \quad (13)$$

342 where  $\Delta M_V$  is mass storage change;  $\sum_{i=1}^{j_V} M_i (j=s,e,d)$  is biogeochemical reaction mass;  
 343  $M_{loss}$  is retention mass of N in surface stream network;  $C_{riv\_sur}$  and  $Q_{riv\_sur}$  are  
 344 concentration of N and discharge of surface stream at each time step, respectively;  $\phi$  is  
 345 coefficient for retention mass of N. The model includes the effects of biogeochemical  
 346 processes on N concentrations ( $\sum_{i=1}^{j_V} M_i (j=s,e,d)$ ) in the stream channel, but biogeochemical  
 347 reactivity in the underground water is assumed to be negligible because nitrate is conservative  
 348 under the oxidizing conditions of many karst aquifer conduits (Perrin et al. 2007; Mahler and  
 349 Garner, 2009). The N loss in surface stream networks ( $M_{loss}$ ) is common (Li et al., 2019),  
 350 especially in reservoirs within stream networks. Lakebed sediments in reservoir systems can  
 351 sequester excess nutrients loaded by rivers through sedimentation (David et al., 2006;  
 352 Saunders and Kalff, 2001). Due to this effect, the reservoirs can be treated as overall sinks for  
 353 N consequently decreasing downstream nutrient loads (Bosch and Allan, 2008; Powers et al.,  
 354 2015; Han et al, 2017; Shaughnessy et al., 2019). Therefore, the retention of N in surface  
 355 stream networks affected by reservoirs was considered using a simple relationship **when**  
 356 **reservoirs exist in the surface river network (Eq. 12).**

357 Conservative tracers, such as stable isotopes of hydrogen and oxygen, can be regarded as  
 358 solutes unaffected by biogeochemical processes. Thus, if the multilayer mass balance model



359 is applied for the solute mass of the tracers, these equations (Eqs. 8 and 10) can be simplified  
 360 by neglecting the biogeochemical reactions ( $\sum_{i=1}^{jv} M_i=0$ ). Even though stable isotope mass  
 361 equations add two additional parameters (fractionation coefficients of  $\tau_s$  and  $\tau_e$  in soil and  
 362 epikarst layer, respectively) for considering isotopic fractionation by evaporation (Fig.6) in  
 363 the soil and epikarst, the isotopic tracer observations can be used to track hydrological  
 364 processes and constrain the calibration parameters:

$$365 \quad M_{s,out} = C_{iso,s} \tau_s (E_{t0} - E_{tu} - E_s) \quad (14)$$

$$366 \quad M_{e,out} = C_{iso,e} \tau_e E_{t0} \quad (15)$$

367 where  $C_{iso,s}$  and  $C_{iso,e}$  are water stable isotope compositions for soil and epikarst,  
 368 respectively.

### 369 3.2.2. Nitrogen sources and Biogeochemical processes

370 Four major N sources are represented in the model: atmospheric deposition,  
 371 anthropogenic non-point sources, biological N fixation and litter fall. In each time step, the  
 372 load of atmospheric deposition N is equal to the product of actual deposition concentration  
 373 and precipitation. Non-point sources, such as fertilizers, are represented on a pixel basis  
 374 directly. The N-fixation is estimated by (Binkley *et al.*, 1994):

$$375 \quad N_{fix} = N_f \cdot \Phi_{T,fix} \quad (16)$$

376 where,  $N_f$  is Nitrogen Fixing Reference Rate;  $\Phi_{T,fix}$  is temperature factor for fixation.

377 Vegetation residue pools from litterfall are divided into a recalcitrant structural pool and a  
 378 rapidly decomposable metabolic residue pool, each with different decay rates and carbon to  
 379 nitrogen (C/N) ratios. The N from decomposed litterfall ( $N_{litter}$ ) is simulated by using a first  
 380 order rate equation, which is added to the ammonium pool (Inamdar *et al.*, 1999):

381 
$$N_{litter} = A \cdot M / (1 + C/N) \cdot \Phi_{T,lit} \cdot \Phi_{\theta,lit} \quad (17)$$

382 where  $A$  is cell area;  $M$  is litter mass;  $\Phi_{T,lit}$  is temperature factor for litterfall;  $\Phi_{\theta,lit}$  is  
 383 moisture factor for litterfall. Soil organic N is not a major source of nitrate in the water  
 384 samples considering the thin soil profile and rapid water movement in the karst system (Liu et  
 385 al., 2009). Therefore, to reduce the complexity, the organic N processes is not considered in  
 386 the model focusing primarily on inorganic nitrogen.

387 Once the N enters soils, it is subject to changes due to biogeochemical processes. After  
 388 biogeochemical transformation for each time step is completed, the dissolved portion of the  
 389 pool drains into the surface and underground stream networks. The total amount of  
 390 nitrification ( $N_n$ ) and ammonia volatilization ( $N_{n-v}$ ) is calculated and then partitioned, using a  
 391 combination of the methods developed by Reddy *et al.* (1979) and Godwin et al. (1984):

392 
$$N_{n-v} = (1 - \exp(-\Phi_n - \Phi_v)) \cdot [NH_4]_L \cdot \frac{1}{24} \quad (18)$$

393 where  $\Phi_n = \Phi_{T,n} \cdot \Phi_{\theta,n} \quad (19)$

394 
$$\Phi_{T,n} = \begin{cases} 0 & T \leq 4 \\ 2^{\frac{T-O_t}{10}} & 4 < T < O_t \\ 1 & T \geq O_t \end{cases} \quad (20)$$

395 and  $\Phi_v = \Phi_D \cdot \Phi_{T,n} \quad (21)$

396 where  $[NH_4]_L$  is mass of  $NH_4$ ;  $\Phi_{T,n}$  is temperature factor for nitrification, controlled by  
 397 temperature ( $T$ ) and the parameter of optimum temperature ( $O_t$ );  $\Phi_{\theta,n}$  is moisture factor for  
 398 nitrification controlled by water content. Then, the nitrification  $N_n$  is estimated by:

399 
$$N_n = N_{n-v} \cdot \frac{1 - \exp(-\Phi_n)}{1 - \exp(-\Phi_n) + 1 - \exp(-\Phi_v)} \quad (22)$$

400 The calculation of denitrification ( $N_d$ ) is modified from Hénault and Germon (2000):

401 
$$N_d = D_p \cdot \Phi_{T,d} \cdot \Phi_{No3} \cdot \Phi_{\theta,d} \quad (23)$$

402 and  $\Phi_{\theta,d} = \begin{cases} 0 & f_{sat} < D_{st} \\ \left(\frac{f_{sat}-0.62}{0.38}\right)^{1.74} & f_{sat} \geq D_{st} \end{cases}$  (24)

403  $\Phi_{NO_3} = \frac{[NO_3]}{(R_{hs}+[NO_3])}$  (25)

404 where  $D_p$  is potential denitrification flux;  $\Phi_{T,d}$  is temperature factor for denitrification  
 405 controlled by temperature;  $\Phi_{\theta,d}$  is moisture factor for denitrification controlled by parameter  
 406 of denitrification saturation threshold ( $D_{st}$ );  $f_{sat}$  is soil moisture saturation extent;  $\Phi_{NO_3}$  is  
 407 nutrient factor controlled by nitrate reduction half saturation fraction ( $R_{hs}$ ).

408 Michealis-Menton saturation kinetics are assumed to be the mechanics of plant  $NH_4$ -N  
 409 uptake ( $NH_{4, uptake}$ ) (Yao et al., 2011; Bicknell et al., 1993), and its calculation includes the  
 410 parameters of Half-rate Ammonium Uptake Constant ( $Au$ ) and Maximum Ammonium Uptake  
 411 Constant ( $Aum$ ):

412  $NH_{4, uptake} = \frac{Aum \cdot [NH_4]_L}{Au + [NH_4]_L} A$  (26)

413 For  $NO_3$ -N uptake ( $NO_{3, uptake}$ ), the model used is a modified yield-based approach, with the  
 414 parameters of Maximum Nitrogen Uptake Delay ( $Num$ ) and Maximum Nitrogen  
 415 Accumulation ( $Nam$ ):

416  $NO_{3, uptake} = Nam \cdot \frac{\exp\left(-\frac{((t)_c - t_{sta} - Num)^2}{2 \cdot \left(\frac{t_{long}}{3}\right)^2}\right)}{\left(\frac{t_{long}}{3}\right) \cdot \sqrt{2\pi}}$  (27)

417 where  $t_c$  is current day;  $t_{sta}$  is growing season start day;  $t_{long}$  is growing season length.

418 A simplified scheme to represent sorption as a function of  $NO_3$ -N ( $NO_{3, sorption}$ ) and  $NH_4$ -N  
 419 ( $NH_{4, sorption}$ ) mass was used in the model:

420  $NO_{3, sorption} = M_{NO_3} \cdot N_a$  (28)

421  $NH_{4, sorption} = M_{NH_4} \cdot A_a$  (29)

422 where  $M_{NO_3}$  and  $M_{NH_4}$  are  $NO_3$  and  $NH_4$  mass, respectively;  $N_a$  is Nitrate Sorption Coefficient;  
423  $A_a$  is Ammonium Adsorption Coefficient.

424 These biogeochemical reactions are assumed to occur in the soil layer in non-karst areas  
425 (see Thanapakpawin (2007) for detail). In our modified model, the nitrification and  
426 denitrification of N occur in both the soil and epikarst zones.

427

### 428 *3.3. Modelling procedures*

429 All simulations were performed on hourly time steps, at a  $100 \times 100 \text{ m}^2$  resolution. The  
430 hourly discharge, daily water stable isotope composition and  $NO_3$ -N concentration were used  
431 for the model calibration. Automatic calibration of the coupled hydrological-N model at such  
432 a high spatiotemporal resolution is very time consuming. Therefore, the step-by-step method  
433 was employed for parameter estimation (Ferrant et al., 2011). The parameters of hydrological  
434 module are optimized first, and then parameters for biogeochemical reactions were manually  
435 calibrated using the optimized hydrological parameters.

436 The parameters of the hydrological module can be divided into sensitive and insensitive  
437 parameters (Yao, 2006; Kelleher et al., 2015). The insensitive parameters were determined as  
438 follows: (1) the vegetation-related parameters were determined by the field investigations,  
439 such as the height of 2.1 and 1 m for forest and crops, respectively; other parameters (e.g.  
440  $LAI$ , albedo and root depth) were based on the Land Data Assimilation System (LDAS); (2)  
441 the soil-related parameters, such as bulk density, porosity and wilting point, were measured  
442 using field experiments and laboratory analysis (Cheng et al., 2011); and 3) the other  
443 insensitive parameters, such as pore size distribution, aerodynamic attenuation and moisture

444 threshold, were drawn from literature (e.g., Thyer et al., 2004; Kelleher et al., 2015). The  
445 sensitive parameters, e.g. hydraulic conductivities ( $K_h$  and  $K_v$ ), field capacity ( $\theta_f$ ) in the soils,  
446 epikarst and deep zones, and canopy fraction ( $C_f$ ) in Table 2, were calibrated against  
447 observations of discharge within the initial ranges of the sensitive parameter in Table 2. In  
448 order to reduce equifinality effects, these sensitive parameters together with two additional  
449 parameters (fractionation constants of  $\tau_s$  and  $\tau_e$  in Table 2) are further calibrated against  
450 observations of isotopic ratios.

451 The modified Kling–Gupta efficiency (KGE) criterion (Kling et al., 2012) was used as  
452 the objective function for flow and isotope calibrations. The criterion balances how well the  
453 model captures the dynamics (correlation coefficient), bias (bias ratio) and variability  
454 (variability ratio) of the actual response (Schaefli and Gupta, 2007). The objective functions  
455 of KGE for the surface stream and underground channel were combined to formulate a single  
456 measure of goodness of fit. Targeted on the flow discharge, the objective function is  $KGE_Q =$   
457  $(KGE_{Q-sur} + KGE_{Q-und}) / 2$  (where  $KGE_{Q-sur}$  and  $KGE_{Q-und}$  are the objective functions for  
458 surface stream and underground channel discharges, respectively). Targeted on the isotopic  
459 concentration, the objective function is  $KGE_i = (KGE_{i-sur} + KGE_{i-und}) / 2$  (where  $KGE_{i-sur}$  and  
460  $KGE_{i-und}$  are the objective functions for isotopic concentrations for surface stream and  
461 underground channel, respectively).

462 A Monte Carlo analysis was used to explore the parameter space during calibration and  
463 provides insight to the resulting uncertainty. In order to derive a constrained parameter set,  
464 two iterations were carried out in the calibration. First, a total of 2000 different parameter  
465 combinations within the initial ranges was randomly generated as the possible parameter

466 combinations (Soulsby et al., 2015; Xie et al., 2018). After the first calibration using  $KGE_Q$   
467 and  $KGE_i > 0.3$  was used as a threshold for model rejection, and the range of each parameter  
468 was narrowed. Then, another 2000 different parameter combinations within the narrowed  
469 ranges were used as for the second calibration, and the parameter space was reduced by  
470 iteratively applying two criteria: 1) the discharge criterion discarded all parameter sets that  
471 obtain a  $KGE_Q < 0.75$ , and 2) the water stable isotope criterion discarded all parameter sets  
472 that obtain a  $KGE_i < 0.5$ . The retained parameter sets were further used for simulation of  
473 possible flow discharges and the tracer compositions, and their uncertainty bands. In addition  
474 to  $KGE$ , root mean squared error (RMSE) and absolute of average relatively error (aARE)  
475 were calculated for evaluation of the model performance.

476 After determining the best hydrological parameter set (it consists of the mean values of  
477 each parameter derived from the retained parameter sets after calibration), the N module  
478 parameters related to biogeochemical reactions (Table 3) were manually calibrated using the  
479 observed  $NO_3-N$  concentrations at the catchment outlets. The values of the biogeochemical  
480 parameters used in Thanapakpawin (2007) were taken as the initial values for model running.  
481 Then these parameters for biogeochemical reactions were calibrated against the best matching  
482  $NO_3-N$  concentrations measured at the outlets. Comparisons of the simulated and measured  
483  $NH_4-N$  concentrations at the catchment outlets were used as a “soft” validation of the  
484 simulations. This strategy of the model calibration was also used in other studies for the  
485 complex simulation of biogeochemical reactions (Zhang et al., 2016, 2017a).

486 The modelling period started on 1 March 2016, but calibration was initiated using  
487 available discharge data from 13 July 2016 and isotopes from 1 June 2016. The preceding

488 four months were therefore used as a spin-up period (the mean of precipitation isotope  
489 signatures over the sampling period was used for this) to fill storages, and initialise storage  
490 tracer and N concentrations.

491

## 492 **4. Results**

### 493 *4.1. Model performance*

494 The modelling results show that the discharge dynamics in surface stream and  
495 underground channel were mostly bracketed by the simulation ranges at the outlet though  
496 some discharges were not completely captured (Fig.7). The objective function values of the  
497 combined  $KGE_Q$  for flow discharge at the outlets were all greater than 0.75 for the 114  
498 retained parameter sets, with a maximal value of 0.81 and the mean of 0.77 over the study  
499 period. The maximal, mean and minimal objective function values were 0.8, 0.77 and 0.7,  
500 respectively, for surface stream discharge ( $KGE_{Q-sur}$ ), and 0.82, 0.78 and 0.72, respectively,  
501 for underground channel discharge ( $KGE_{Q-und}$ ). The mean of RMSE and aARE is 0.31 m<sup>3</sup>/s  
502 (0.23-0.39 m<sup>3</sup>/s) and 10% (6%~16%), respectively, for surface stream discharge, which is  
503 larger than 0.28 m<sup>3</sup>/s (0.21~0.35 m<sup>3</sup>/s) and 7% (4%~13%) for underground channel. The  
504 simulated results capture the surface stream flow during the heavy rainfall periods (Fig.7).

505 The simulated water stable isotope ratios show that the model generally reproduces the  
506 overall  $\delta D$  signal of surface stream and underground channel water during study period  
507 (Fig.8). The combined  $KGE_i$  for water stable isotope composition at the stream and  
508 underground channel outlets were all greater than 0.5, with a mean of 0.62 and maximal value  
509 of 0.67. The mean of RMSE and aARE is 8.9 ‰ (5.7-10.9 ‰) and 12% (8 ‰~19 ‰),

510 respectively, for surface stream discharge, which is larger than 5.6 ‰ (3.5~7.6 ‰) and 11 %  
511 (6 %~16 %) for underground channel. As is common in coupled flow-tracer models, the  
512 performance in the simulation of water stable isotopes was less satisfactory and more  
513 uncertain than for discharge (Table 4). There were some enriched “outliers” in underground  
514 channel water with high isotope values out of the uncertainty range (the maximum of  $\delta D$  less  
515 than -50 ‰). The most likely explanation for this is flooded paddy fields, which are  
516 extensively distributed in the depression during the growing season, this allows evaporative  
517 fractionation effects which are transferred to the channel network in larger events Zhang et  
518 al., (2019).

519 Although the performance of the coupled flow-tracer model for isotope simulation was  
520 less accurate than for discharge simulation, targeting both the flow discharge and isotopic  
521 concentration (e.g. meeting  $KGE_Q \geq 0.75$  and  $KGE_i \geq 0.5$ ) can effectively narrow the  
522 parameter ranges and thus reduce equifinality effect of these additional parameters on the  
523 simulated results (Fig.9).

524 The calibrated parameters for modelled biogeochemical reactions for  $N$  are listed in  
525 Table 3. The modelled results with this parameter set show that the simulated daily  $NO_3-N$   
526 concentrations can generally capture the observations at the outlets of the surface stream and  
527 underground channel (Fig.10). The simulated uncertainty of  $NO_3-N$  is larger than that of  
528 discharge and isotopic profile as the model structure becomes more complex and the number  
529 of calibrated parameters increases. The  $KGE_{N-sur}$  and  $KGE_{N-und}$  for daily  $NO_3-N$   
530 concentrations were 0.45 and 0.5 at surface stream and underground outlets, respectively. The  
531 mean of RMSE and aARE is 1.06 mg/L and 14 % respectively for surface stream, both



532 greater than 0.37 mg/L and 12 %, respectively for underground channel. The larger deviation  
533 of the simulated N in surface river could result from complex flow regulation and  
534 biogeological processes in the reservoir (Wang et al., 2020).

535 The measured  $\text{NH}_4\text{-N}$  concentrations at the outlets were further used to test the model  
536 performance. Since the  $\text{NH}_4\text{-N}$  concentrations of water in the study area were very low ( $\sim 10^{-2}$   
537 mg/L) (smaller than the calculation errors of the mixing and biogeochemical processes of  
538  $\text{NH}_4\text{-N}$ ), the simulated results cannot capture variability but the magnitude of the simulated  
539 and measured concentrations is of the same order for both the surface stream and underground  
540 channel outlets (Fig.11). The mean measured and simulated  $\text{NH}_4\text{-N}$  concentrations are 0.05  
541 and 0.06 mg/L, and the total measured and simulated loadings of  $\text{NH}_4\text{-N}$  are 224 and 262 kg,  
542 respectively, for surface river during the observation period (a total of 30 days). For  
543 underground channel, both the mean measured and simulated  $\text{NH}_4\text{-N}$  concentrations are 0.05  
544 mg/L, and the total measured and simulated loadings of  $\text{NH}_4\text{-N}$  are 341 and 343 kg,  
545 respectively, over the observation period (a total of 38 days).

546

#### 547 4.2. Vertical and spatial distributions of the simulated $\text{NO}_3\text{-N}$ storages

548 Fig.12 shows the spatial distribution of simulated  $\text{NO}_3\text{-N}$  loadings (concentrations of  
549  $\text{NO}_3\text{-N}$  multiplied by the flux in each layer) in the three layers of the critical zone. Spatial  
550 variations of the  $\text{NO}_3\text{-N}$  loadings in soils are most marked because of spatial difference of soil  
551 thickness, hydraulic conductivity and land cover.  $\text{NO}_3\text{-N}$  loadings in the relatively thick soils  
552 in the western plain are mostly larger than those in the thin soils in the eastern mountains  
553 (Fig.12a). In spite of thin soils over the whole catchment, the soil layer was the largest  $\text{NO}_3\text{-N}$

554 store in the catchment (Fig.12). The average values of  $\text{NO}_3\text{-N}$  in the soil, epikarst and deep  
555 flow layers are 58.4, 18.6 and 15.3kg/ha, respectively. In each of the layers, the  $\text{NO}_3\text{-N}$   
556 loadings in the farm land are much larger than those in the forest areas (Fig.12d). For  
557 example, the annual  $\text{NO}_3\text{-N}$  loading is 452 and 40 t for the soil layers in the farm land and  
558 forest respectively. The greater  $\text{NO}_3\text{-N}$  loading in the farm land is mainly attributed to the  
559 high fertilization rates in this region (e.g. the  $\text{NO}_3\text{-Ns}$  for paddy soil and yellow soil were 67  
560 and 53 kg/ha, respectively).

561

#### 562 *4.3. Simulated exchanges of N fluxes in the critical zone and catchment N balance*

563 Fig.13 shows daily and cumulative net input and the simulated loss of N from 13 July  
564 2016 to 31 October 2017 in the catchment. Atmospheric deposition, litter fall and fixation  
565 show less seasonal variability. The much greater N input (the short lines in Fig 13) indicates  
566 fertilizer input in farm land, shown by a marked increase of the cumulative input occurred in  
567 the fertilizer period in May ~ early June. The greatest input results in a prolonged increase of  
568 N loading for the high discharge in the wet season from May to September in this catchment.

569 The simulated nitrification and denitrification rates of N over the study period clearly  
570 showed a seasonal variability with temperature and wetness in a year (Fig.14). The daily rates  
571 of nitrification and denitrification are much higher in wet season (0.34 and 0.21 kg N/ha for  
572 nitrification and denitrification, respectively) than in dry season (0.01 and 0.06 kg N/ha,  
573 respectively). The peaks of nitrification and denitrification occur in the fertilizer periods. The  
574 highest peaks of nitrification and denitrification rates (2.7 and 0.53 kg N/ha, respectively)  
575 correspond to the heaviest fertilization in May ~ early June.

576 The simulated annual N fluxes (including NO<sub>3</sub>-N and NH<sub>4</sub>-N) between the layers in the  
577 critical zones are shown in Fig.15. For the total input of N (1417t) from atmospheric  
578 deposition (149t), fertilizer (1220t), litter fall (42t) and fixation (6t) in the catchment during  
579 the study year, fertilizer accounts for 86 %. These inputs are mainly consumed by terrestrial  
580 plant uptake (~ 636t), accounting for about 45% of the total input of N. The remaining losses  
581 are from ammonia volatilization (~118t), denitrification (~396t), and surface channel retention  
582 (~31t), and exports from the catchment via the surface stream (58t) and underground channel  
583 (135t).

584 From the total input of N (1417t) to the soil layer, 254 t of N leaches into the underlying  
585 epikarst zone, and 97t of N is transported to the surface stream and subsurface channel, 636t  
586 of N is absorbed by plant, 278t is denitrified, and 83t is volatilized. Of the 254t of N which  
587 drains into the epikarst zone, nearly half of it (108t) is transported to the subsurface channel,  
588 118t of N is denitrified, 35t is volatilized, and only 15t drains into the deeper aquifer. The  
589 large flux of N from the epikarst to the subsurface channel results in greater annual export of  
590 N from underground channel (135t), compared to the surface stream (58t).

591

## 592 **5. Discussion**

### 593 *5.1. Uncertainty of the simulation with increased model complexity*

594 The hydrological-biogeochemical model in this study was developed by considering  
595 flow and N fluxes in the karst critical zone characterized by special geomorphologic  
596 conditions, such as fractured zone (epikarst) and sinkholes that interconnect with surface and  
597 subsurface streams. Even though there are still uncertainties for the modelling results,

598 particularly for the N simulations, the model can simulate the concurrent dynamics of  
599 hydrological, isotopic and N processes in the catchment. It was found that N loading is  
600 linearly proportional to discharge for both surface stream and underground channel at the  
601 catchment outlet (Fig.4), and thus capturing hydrological dynamics for the model, aided with  
602 detailed hydro-chemical observations, is essential for controlling the N-loading variations in  
603 this karst catchment. In order to capture hydrological dynamics and reduce uncertainties  
604 arising from increasing complexity of the model structure and associated parameterisation  
605 (e.g. increase of the vertical zones and the related parameters), we constrained hydrological  
606 module parameter ranges in the model calibration by using a combination of observations of  
607 flow discharges and isotopic concentrations. We found that although the isotope-aided model  
608 introduced two additional parameters, the detailed observations of isotopic concentrations can  
609 narrow the parameter ranges and thus reduce equifinality effect of parameters on the  
610 simulated results (Fig.7).

611 The relatively larger uncertainties of N simulations arise from increasing complexity of  
612 the model structure, and from observations of N and calibration procedures. For example, the  
613 N inputs were estimated from field surveys at some specific sites (e.g., the fertilizer and the  
614 fraction of bean production), from measurements in other areas (e.g., litter fall), and from  
615 other research (e.g., the referenced rate of annual N fixation from Smil (1999)). Even though  
616 high temporal resolution of N concentrations has been monitored at the catchment outlets,  
617 more detailed observations and field surveys of these inputs are required to reduce uncertainty  
618 in the complex hydrological and biogeochemical processes.

619 The parameter calibration in this study employs a step-wise procedure of targeting

620 simulation accuracies of outlet discharges and water stable isotope ratios for the hydrological  
621 module, and then the NO<sub>3</sub>-N concentrations for the biogeochemical module. The procedure is  
622 computationally efficient for complex model calibration in terms of the Monte Carlo  
623 framework, but it weakens interactions between hydrological and biogeochemical dynamics.  
624 In future research, simultaneous calibration of the hydrological-biogeological model  
625 parameters by combining use of hydrological observations, isotopic analysis (including N  
626 isotope analysis) and N concentrations may help further constrain the parameter ranges and  
627 reduce uncertainty of N simulations.

628

## 629 *5.2. N sources and pathways in karst landscapes*

630 Assessing N sources and transfer pathways is an evidence base for promoting efficient  
631 use of N and preventing N loss, thereby improving N management at the catchment scale  
632 (Pionke et al., 1996; Heathwaite et al., 2005; Jarvie et al., 2008, 2017; Kovacs et al., 2012).  
633 Our distributed model provides quantitative information on N sources and loads (Fig.15),  
634 which are essential for catchment managers who need to make evidence-based decisions on N  
635 pollution controls. In this catchment, about 61 % of N export occurred during the wet season,  
636 because of the large stream flow during that time. This is driven by the high water flux  
637 transporting large amounts of N from the soil reservoir into the epikarst and deep flow zone,  
638 and then into the surface and underground channels. Therefore, the quick response of water  
639 flow to rainfall usually leads to the concentrated export of N in karst catchments. Many  
640 studies have indicated that delivery times for soil water, shallow groundwater and deep  
641 groundwater to river systems range from years to decades in non-karst areas (Sanford and

642 Pope, 2013). The considerable contribution of N loading to streams from groundwater (e.g. 67  
643 % groundwater contributions to river N loading in Yongan catchment in southeast China)  
644 leads to a marked lag effect of N flux (Hu et al. 2018). However, the epikarst reservoir in the  
645 Houzhai catchment contributes the most N to the surface stream and underground channel  
646 (~45%, in Fig.15) through fractures/conduits in the karst, which implies the potential for a  
647 low hydrologic lag effect of N flux due to the high hydraulic conductivity of epikarst ( $5 \times 10^{-5}$  -  
648  $4 \times 10^{-4}$  m/s in Table 2).

649 The limited soils in karst areas are extremely important for sustaining crop and plant  
650 growth. The simulated spatial distributions of  $\text{NO}_3\text{-N}$  indicated that the main reservoirs and  
651 sources of N are located in the cultivated land of low lying plain and valley areas with  
652 relatively thick soil cover in southwest China. Meanwhile, the frequent, heavy fertilization  
653 accentuates N accumulation in the farm land, and this makes these areas the main sources of  
654 N loss during rainstorm periods. In addition, the soil properties and underlying rocks also  
655 have marked influences on N loading and export. Under the same effect of fertilization, the N  
656 loading of the soil reservoir in yellow soils in the dolostone was markedly lower than that  
657 with paddy soil in the limestone, because of the higher infiltration and percolation rates.

658 Sinkholes are another important transport and export pathway. Sinkholes sometimes  
659 function as storm drains because they directly link to the underlying aquifer systems  
660 (Tihansky, 1999). In the upstream area with more sinkholes, over 90 % of the N export was in  
661 the wet season (Yue, 2019). However, the importance of N flux through sinkholes in karst  
662 areas is a relatively under-researched topic in soil and water science.

663

664 *5.3. Implications for fertilization management in karst areas*

665 Agricultural non-point sources, such as organic and inorganic fertilizers, have been  
666 increasingly recognized as a major contributor to N pollution in catchments (Dupas et al.,  
667 2015). In many karst catchments worldwide, N fertilizer is a major contributor to aquifer  
668 contamination (Panno et al, 2001; Minet et al., 2017; Eller and Katz, 2017). In southwest  
669 China, one of the largest continuous karst areas in the world, researchers also identified  
670 agricultural activities as the predominant source of aquifer N, but found the contribution of  
671 atmospheric N to be negligible (Yang et al., 2013). Consequently, spatially and temporally  
672 targeted fertilization management is becoming more important for effective, catchment-wide  
673 reductions in N loss from land to water. The simulated N fluxes showed that the proportion of  
674 N uptake by crops was no more than 50 % of the fertilizer applied, which means there are  
675 marked N losses and/or accumulation in the karst system. Therefore, improving the efficiency  
676 of fertilization represents a priority for reducing the N losses and subsequent contamination of  
677 water. In addition, the main period of fertilizer application is usually in May in the study area  
678 (Yue et al., 2019), corresponding to the end of the dry season and beginning of the rainy  
679 season. Consequently, applied N will rapidly infiltrate to the deeper soil layers, the epikarst,  
680 and even the deep flow zone during heavy rainfall events leading to the N loss. Importantly  
681 when water levels in sub-surface conduits increase beyond sustaining the low flows from the  
682 karst aquifer, the water will flow into small fractures from conduits (Zhang et al., 2017b).  
683 Consequently, N transported will also enter the small fractures and accumulate, leading to  
684 extensive, potentially long-term contamination of the karst system. Elsewhere the karst  
685 system has been observed to delay N flux to streams during storm events and thereafter export

686 N at a more gradual rate distributed over the flood recession (Husic et al., 2018). To reduce  
687 the N loss and karst critical zone pollution (mainly in the epikarst), measures to reduce the N  
688 entering the underground system are critical for mitigating epikarst N loading, such as  
689 decreasing the N input during periods when there is strong hydraulic connectivity between  
690 soil and epikarst/deep flow zone. Therefore, fertilization may be more reasonable if timed for  
691 drier periods before the wet season starts or large storm events are forecast.

692 N management scenarios within karst catchments should not only consider the N fluxes  
693 within the surface or underground system but also the transformation of N between them via  
694 the sinkholes. Since a large number of sinkholes are located in the cultivated land of plain and  
695 valley areas, restricting fertilization around sinkholes to decrease the concentrated and fast  
696 loss of N is necessary for spatial zoning of agricultural activities.

697

## 698 **6. Conclusions**

699 Water and N transport in karst areas depend strongly on the structure of the critical zone  
700 and the karst flow system. In this study, a hydrological-biogeochemical model was developed  
701 by considering the effects of unique karstic characteristics on flow and N dynamics.

702 The model has been successfully applied in the karst catchment of Houzhai where  
703 detailed observation data of flow, stable isotopes and N concentrations, and geomorphological  
704 surveys for soil properties, fracture distribution and karst topography were available.  
705 Uncertainty analysis using Monte Carlo analysis and multi-objective calibration was used  
706 targeting initially flow and water stable isotopes, and then N simulations. Multiple sources of  
707 observations are used to identify main controlling factors of N loading, such as hydrological



708 dynamics in the catchment. The multi-objective calibration, combining discharge with water  
709 stable isotopes, can significantly constrain the parameters and reduce equifinality effect of  
710 parameters on the simulated results. The modelling results reveal functional effects of karst  
711 geomorphology and land use on spatio-temporal variations of hydrological processes and N  
712 transport, such as the large amount of N released from soil reservoirs to the epikarst (via  
713 fractures or sinkholes) and then exported to the underground channel. The modelling results  
714 also show regional differences of hydrological processes and N transport in relation to the  
715 distribution of soils, epikarst and groundwater aquifer controlled by geological conditions. In  
716 the limestone area of the south characterized by the thin soils, rich fractures and sinkholes, the  
717 flow and NO<sub>3</sub>-N loadings in the underground channel are about 2.3 and 2 times larger,  
718 respectively, than those in the north surface stream overlying the dolomite stone.

719       The large proportion of N draining into groundwater could lead to extensive, potentially  
720 long-term contamination of the karst system. Therefore, improving the efficiency of  
721 fertilization is an urgent need to reduce the N losses and contamination. It is worth noting that  
722 in karst landscapes with surrounding hills separated by star-shaped valleys, in the southwest  
723 of China, most sinkholes are distributed in the valleys covered by thick soil. These areas are  
724 often characterised by farmland, with high N inputs due to fertilizer applications. Therefore,  
725 improving agricultural management in valleys/depressions has a key role to play in reducing  
726 regional N loss and pollution in karst area.

727       The modelling indicates that uncertainty increases with model complexity and  
728 parameterisation. Strengthening the modelling capability particularly biogeochemical  
729 processes, is vital for understanding transport of N and other N components. Improvements to

730 the modelling could be achieved if supported by additional surveys of geological conditions  
731 to describe the strong heterogeneity of the karst structure in detail, and biogeochemical  
732 analysis, such as  $^{15}\text{N-NO}_3$ , to trace N sources and its transformation. Importantly, in addition  
733 to input-output observations, monitoring of hydrological and biogeochemical dynamics in  
734 different zones, such as vegetation, soils, epikarst and deep aquifer, can help adequate  
735 expressions of hydrological and biogeochemical processes in each medium and further  
736 improve the reliability of the modelling results.

737

738 **Acknowledgments.** This research was supported by The UK-China Critical Zone  
739 Observatory (CZO) Programme (41571130071/2), the National Natural Science Foundation  
740 of China (41971028, 41571020), the National Key Research and development Program of  
741 China (2016YFC0502602), and the UK Natural Environment Research Council  
742 (NE/N007468/1, NE/N007425/1). In addition, we thank the two anonymous reviewers and the  
743 editor for their constructive comments which significantly improved the manuscript.

744

## 745 **References**

- 746 Arnold, J.G., Srinivasan, R., Muttiah, R.S., Williams, J.R., 1998. LARGE AREA  
747 HYDROLOGIC MODELING AND ASSESSMENT PART I: MODEL  
748 DEVELOPMENT. *J. Am. Water Resour. Assoc.* 34, 73–89.
- 749 Barton, L., McLay, C.D.A., Schipper, L.A., Smith, C.T., 1999. Annual denitrification rates in  
750 agricultural and forest soils: a review. *Aust. J. Soil Res.* 37 (6), 1073-1093.
- 751 [Bicknell, B.R., Imhoff, J.C., Kittle, J.L., Donigian, A.S., Johanson, R.C., 1993. Hydrological  
752 Simulation Program-Fortran \(HSPF\): User's manual for release 10.0. EPA-600/3-84-066.  
753 Environmental Research Laboratory, USEPA. Athens, GA.](#)

- 754 Binkley, D., Cromack, K. Jr., Baker, D., 1994. Nitrogen fixation by Red Alder: biology, rates,  
755 and controls, in: Hibbs, D. (Ed.), *The Biology and Management of Red Alder*. Oregon  
756 State University Press, Corvallis. pp. 57-72.
- 757 Birkel, C., Soulsby, C., Tetzlaff, D., 2015. Conceptual modelling to assess how the interplay  
758 of hydrological connectivity, catchment storage and tracer dynamics controls  
759 nonstationary water age estimates. *Hydrol. Process.* 29, 2956–2969.
- 760 Bosch, N.S., Allan, J.D., 2008. The influence of impoundments on nutrient budgets in two  
761 catchments of Southeastern Michigan. *Biogeochemistry.* 87(3), 325–338.
- 762 Brooks, R.H., Corey, a T., 1964. Hydraulic properties of porous media, *Hydrology Papers*,  
763 Colorado State University. Pap. 3. Fort Collins CO.  
764 <https://doi:citeulike-article-id:711012>.
- 765 Chen, X., Zhang, Z., Soulsby, C., Cheng, Q., Binley, A., Jiang, R., Tao, M., 2018.  
766 Characterizing the heterogeneity of karst critical zone and its hydrological function: An  
767 integrated approach. *Hydrol. Process.* 32, 2932–2946.
- 768 Chen, X., Chen, C., Hao, Q., Zhang, Z., Shi, P., 2008. Simulation of Rainfall-Underground  
769 Outflow Responses of a Karstic Watershed in Southwest China with an Artificial Neural  
770 Network, in: *Sinkholes and the Engineering and Environmental Impacts of Karst*.  
771 American Society of Civil Engineers, Reston, VA, pp. 433–443.
- 772 Cheng, Q., 2008. Perspectives in Biological Nitrogen Fixation Research. *J. Integr. Plant Biol.*  
773 50, 786–798.
- 774 Cheng, Q., Chen, Xi, Chen, Xunhong, Zhang, Z., Ling, M., 2011. Water infiltration  
775 underneath single-ring permeameters and hydraulic conductivity determination. *J.*  
776 *Hydrol.* 398, 135–143.
- 777 David, M.B., Wall, L.G., Royer, T. V., Tank, J.L., 2006. Denitrification and the nitrogen  
778 budget of a reservoir in an agricultural landscape. *Ecol. Appl.* 16(6), 2177–2190.
- 779 Dupas, R., Delmas, M., Dorioz, J.-M., Garnier, J., Moatar, F., Gascuel-Oudou, C., 2015.  
780 Assessing the impact of agricultural pressures on N and P loads and eutrophication risk.  
781 *Ecol. Indic.* 48, 396–407.
- 782 Eller, K.T., Katz, B.G., 2017. Nitrogen Source Inventory and Loading Tool: An integrated  
783 approach toward restoration of water-quality impaired karst springs. *J. Environ. Manage.*  
784 196, 702–709.
- 785 Ferrant, S., Oehler, F., Durand, P., Ruiz, L., Salmon-Monviola, J., Justes, E., Dugast, P.,  
786 Probst, A., Probst, J.-L., Sanchez-Perez, J.-M., 2011. Understanding nitrogen transfer

- 787 dynamics in a small agricultural catchment: Comparison of a distributed (TNT2) and a  
788 semi distributed (SWAT) modeling approaches. *J. Hydrol.* 406, 1–15.
- 789 Ford, D.C., Williams, P.W., 1989. *Karst Geomorphology and Hydrology*. Unwin Hyman:  
790 London.
- 791 Godwin, D.C., Jones, C.A., Ritchie, J.T., Vlek, P.L.G., Youngdahl, L.J., 1984. The water and  
792 nitrogen components of the CERES models. *Proc. Int. Symp. Minim. Data Sets*  
793 *Agrotechnology Transf. Patancheru, India*.
- 794 Han, Z.W., Zhang, S., Wu, P., Cao, X.X., Tu, H., 2017. Distribution characteristics of  
795 nitrogen and phosphorus in waters and release flux estimation in the sediment of Caohai  
796 basin, Guizhou. *Chinese Journal of Ecology*.
- 797 Hartmann, A., Goldscheider, N., Wagener, T., Lange, J., Weiler, M., 2014. Karst water  
798 resources in a changing world: Review of hydrological modeling approaches. *Rev.*  
799 *Geophys.* 52, 218–242.
- 800 Heathwaite, A.L., Quinn, P.F., Hewett, C.J.M., 2005. Modelling and managing critical source  
801 areas of diffuse pollution from agricultural land using flow connectivity simulation. *J.*  
802 *Hydrol.* 304, 446–461.
- 803 Hénault, C., Germon, J.C., 2000. NEMIS, a predictive model of denitrification on the field  
804 scale. *Eur. J. Soil Sci.* 51, 257–270.
- 805 Hu, M., Liu, Y., Wang, J., Dahlgren, R.A., Chen, D., 2018. A modification of the Regional  
806 Nutrient Management model (ReNuMa) to identify long-term changes in riverine  
807 nitrogen sources. *J. Hydrol.* 561, 31–42.
- 808 Husic, A., Fox, J., Adams, E., Ford, W., Agouridis, C., Currens, J., Backus, J., 2019. Nitrate  
809 Pathways, Processes, and Timing in an Agricultural Karst System: Development and  
810 Application of a Numerical Model. *Water Resour. Res.* 55, 2079–2103.
- 811 [Inamdar, S.P., Lowrance, R.R., Altier, L.S., Williams, R.G., Hubbard, R.K., 1999. Riparian  
812 Ecosystem Management Model \(REMM\): II. testing of the water quality and nutrient  
813 cycling component for a coastal plain riparian system. \*Transactions of the ASAE\*, 42 \(6\),  
814 1691-1707.](#)
- 815 Jarvie, H.P., Johnson, L.T., Sharpley, A.N., Smith, D.R., Baker, D.B., Bruulsema, T.W.,  
816 Confesor, R., 2017. Increased Soluble Phosphorus Loads to Lake Erie: Unintended  
817 Consequences of Conservation Practices? *J. Environ. Qual.* 46, 123–132.
- 818 Jarvie, H.P., Withers, P.J.A., Hodgkinson, R., Bates, A., Neal, M., Wickham, H.D., Harman,  
819 S.A., Armstrong, L., 2008. Influence of rural land use on streamwater nutrients and their  
820 ecological significance. *J. Hydrol.* 350, 166–186.

- 821 Jones, A.L., Smart, P.L., 2005. Spatial and temporal changes in the structure of groundwater  
822 nitrate concentration time series (1935–1999) as demonstrated by autoregressive  
823 modelling. *J. Hydrol.* 310, 201–215.
- 824 Kelleher, C., Wagener, T., McGlynn, B., 2015. Model-based analysis of the influence of  
825 catchment properties on hydrologic partitioning across five mountain headwater  
826 subcatchments. *Water Resour. Res.* 51, 4109–4136.
- 827 Klimchouk, A., 2004. Towards defining, delimiting and classifying epikarst: Its origin,  
828 processes and variants of geomorphic evolution. *Speleogenes. Evol. Karst Aquifers.*
- 829 Kling, H., Fuchs, M., Paulin, M., 2012. Runoff conditions in the upper Danube basin under an  
830 ensemble of climate change scenarios. *J. Hydrol.* 424–425, 264–277.
- 831 Kovacs, A., Honti, M., Zessner, M., Eder, A., Clement, A., Blöschl, G., 2012. Identification  
832 of phosphorus emission hotspots in agricultural catchments. *Sci. Total Environ.* 433,  
833 74–88.
- 834 Kruse, S., Grasmueck, M., Weiss, M., Viggiano, D., 2006. Sinkhole structure imaging in  
835 covered Karst terrain. *Geophys. Res. Lett.* 33, L16405.
- 836 Li, C., Aber, J., Stange, F., Butterbach-Bahl, K., Papen, H., 2000. A process-oriented model  
837 of N<sub>2</sub>O and NO emissions from forest soils: 1. Model development. *J. Geophys. Res.*  
838 *Atmos.* 105, 4369–4384.
- 839 Li, C., Li, S.L., Yue, F.J., Liu, J., Zhong, J., Yan, Z.F., Zhang, R.C., Wang, Z.J., Xu, S., 2019.  
840 Identification of sources and transformations of nitrate in the Xijiang River using nitrate  
841 isotopes and Bayesian model. *Sci. Total Environ.* 646, 801–810.
- 842 Liu, C.Q., 2009. Biogeochemical processes and cycling of nutrients in the Earth's surface:  
843 Cycling of nutrients in soil–plant systems of karstic environments, Southwest China. (In  
844 Chinese) Science Press, Beijing, China.
- 845 Mahler, B.J., Garner, B.D., 2009. Using nitrate to quantify quick flow in a karst aquifer.  
846 *Ground Water.* 47(3),350-360.
- 847 McDonnell, J.J., Beven, K., 2014. Debates-The future of hydrological sciences: A (common)  
848 path forward? A call to action aimed at understanding velocities, celerities and residence  
849 time distributions of the headwater hydrograph. *Water Resour. Res.* 50, 5342–5350.
- 850 Minet, E.P., Goodhue, R., Meier-Augenstein, W., Kalin, R.M., Fenton, O., Richards, K.G.,  
851 Coxon, C.E., 2017. Combining stable isotopes with contamination indicators: A method  
852 for improved investigation of nitrate sources and dynamics in aquifers with mixed  
853 nitrogen inputs. *Water Res.* 124, 85–96.

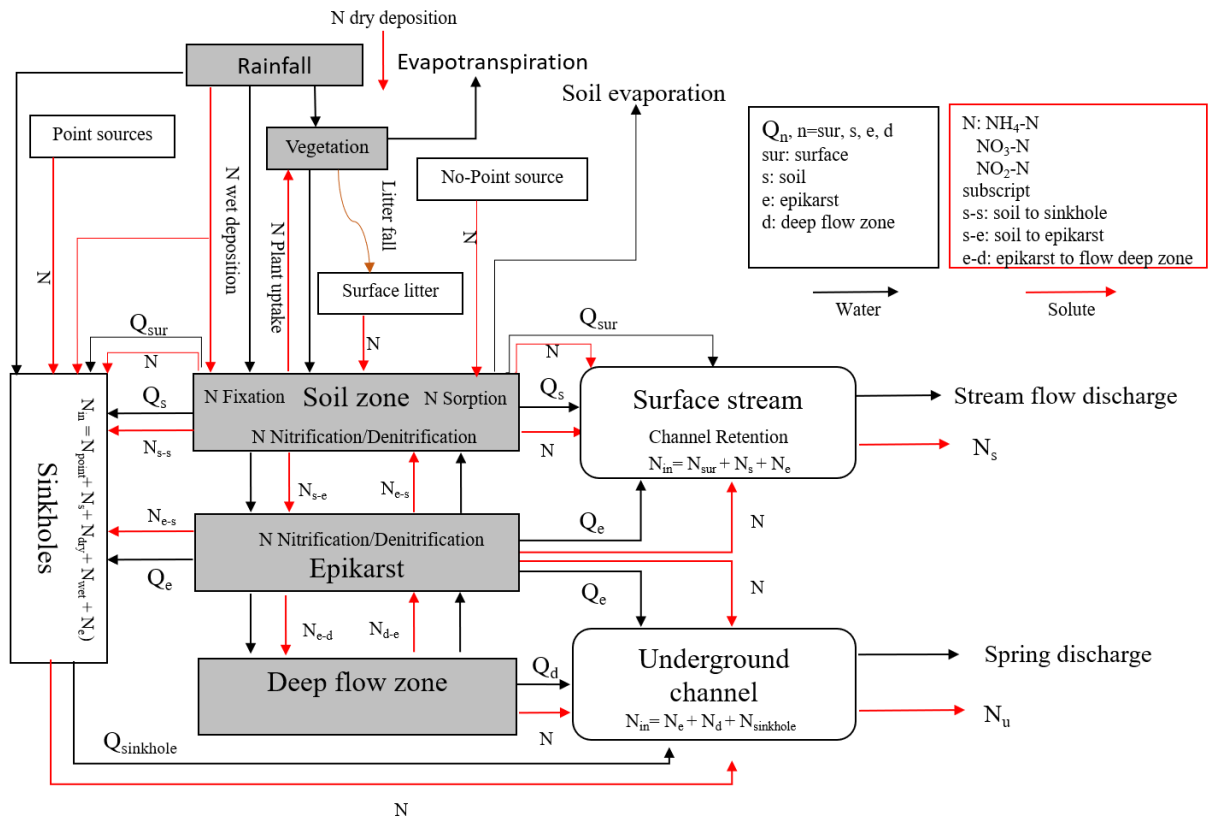
- 854 Opsahl, S.P., Musgrove, M., Slattery, R.N., 2017. New insights into nitrate dynamics in a  
855 karst groundwater system gained from in situ high-frequency optical sensor  
856 measurements. *J. Hydrol.* 546, 179–188.
- 857 Panno, S., Hackley, K., Hwang, H., Kelly, W., 2001. Determination of the sources of  
858 nitrate contamination in karst springs using isotopic and chemical indicators. *Chem.*  
859 *Geol.* 179, 113–128.
- 860 Perrin, J., Jeannin, P.-Y., Zwahlen, F., 2003. Epikarst storage in a karst aquifer: a conceptual  
861 model based on isotopic data, Milandre test site, Switzerland. *J. Hydrol.* 279, 106–124.
- 862 Perrin, J., Jeannin, P.Y., Cornaton, F., 2007. The role of tributary mixing in chemical  
863 variations at a karst spring, Milandre, Switzerland. *J. Hydrol.* 332, 152–173.
- 864 Pi, F., 2017. Study on forest ecological stoichiometry and carbon, nitrogen and phosphorus  
865 cycle in Karst region of central Guizhou, Master's thesis, Guizhou University (in  
866 Chinese).
- 867 Pionke, H.B., Gburek, W.J., Sharpley, A.N., Schnabel, R.R., 1996. Flow and nutrient export  
868 patterns for an agricultural hill-land watershed. *Water Resour. Res.* 32, 1795–1804.
- 869 Piovano, T.I., Tetzlaff, D., Ala-aho, P., Buttle, J., Mitchell, C.P.J., Soulsby, C., 2018. Testing  
870 a spatially distributed tracer-aided runoff model in a snow-influenced catchment: Effects  
871 of multicriteria calibration on streamwater ages. *Hydrol. Process.* 32, 3089–3107.
- 872 Powers, S.M., Tank, J.L., Robertson, D.M., 2015. Control of nitrogen and phosphorus  
873 transport by reservoirs in agricultural landscapes. *Biogeochemistry.* 124(1- 3), 417–439.
- 874 [Ranzini, M., Forti, M.C., Whitehead, P.G., Arcova, F.C.S., de Cicco, V., Wade, A.J., 2007.](#)  
875 [Integrated Nitrogen Catchment model \(INCA\) applied to a tropical catchment in the](#)  
876 [Atlantic Forest, São Paulo, Brazil. \*Hydrol. Earth Syst. Sci.\* 11, 614–622.](#)
- 877 Reddy, K.R., Khaleel, R., Overcash, M.R., Westerman, P.W., 1979. A Nonpoint Source  
878 Model for Land Areas Receiving Animal Wastes: I. Mineralization of Organic Nitrogen.  
879 *Trans. ASAE* 22, 0863–0872.
- 880 Sanford, W.E., Pope, J.P., 2013. Quantifying Groundwater's Role in Delaying Improvements  
881 to Chesapeake Bay Water Quality. *Environ. Sci. Technol.* 47, 13330–13338.
- 882 Saunders, D.L., Kalff, J., 2001. Nitrogen retention in wetlands, lakes and rivers.  
883 *Hydrobiologia.* 443(1/3), 205–212.
- 884 Schaefli, B., Gupta, H. V., 2007. Do Nash values have value? *Hydrol. Process.* 21,  
885 2075–2080.

- 886 Shaughnessy, A.R., Sloan, J.J., Corcoran, M.J., Hasenmueller, E.A., 2019. Sediments in  
887 Agricultural Reservoirs Act as Sinks and Sources for Nutrients over Various Timescales.  
888 *Water Resour. Res.* 55, 5985–6000.
- 889 Smil, V., 1999. Nitrogen in crop production: An account of global flows. *Global Biogeochem.*  
890 *Cycles* 13, 647–662.
- 891 Soulsby, C., Birkel, C., Geris, J., Dick, J., Tunaley, C., Tetzlaff, D., 2015. Stream water age  
892 distributions controlled by storage dynamics and nonlinear hydrologic connectivity:  
893 Modeling with high-resolution isotope data. *Water Resour. Res.* 51, 7759–7776.
- 894 Sprenger, M., Volkmann, T.H.M., Blume, T., Weiler, M., 2015. Estimating flow and transport  
895 parameters in the unsaturated zone with pore water stable isotopes. *Hydrol. Earth Syst.*  
896 *Sci.* 19, 2617–2635.
- 897 Thanapakpawin, P., 2007. Spatially-distributed modeling of hydrology and nitrogen export  
898 from watersheds. PHD's thesis, University of Washington
- 899 Thyer, M., Beckers, J., Spittlehouse, D., Alila, Y., Winkler, R., 2004. Diagnosing a  
900 distributed hydrologic model for two high-elevation forested catchments based on  
901 detailed stand- and basin-scale data. *Water Resour. Res.* 40.
- 902 Tihansky, A.B., 1999. Sinkholes, west-central Florida. L. Subsid. United States US Geol.  
903 *Surv. Circ.*
- 904 Wang, Z.J., Li, S.L., Yue, F.J., Qin, C.Q., Buckerfield, S., Zeng, J., 2020. Rainfall driven  
905 nitrate transport in agricultural karst surface river system: Insight from high resolution  
906 hydrochemistry and nitrate isotopes. *Agric. Ecosyst. Environ.* 291, 106787.
- 907 Wigmosta, M.S., Vail, L.W., Lettenmaier, D.P., 1994. A distributed hydrology-vegetation  
908 model for complex terrain. *Water Resour. Res.* 30, 1665–1679.
- 909 Wigmosta, M.S., Perkins, W.A., 2001. Simulating the effects of forest roads on watershed  
910 hydrology, in *Land Use and Watersheds: Human Influence on Hydrology and*  
911 *Geomorphology in Urban and Forest Areas, Water Sci. Appl. Ser.*, vol. 2, edited by M.  
912 Wigmosta, and S. Burgess, pp. 127–143, AGU, Washington, D. C.
- 913 Williams, P.W., 2008. The role of the epikarst in karst and cave hydrogeology: A review. *Int.*  
914 *J. Speleol.* 37(1),1-10.
- 915 Xie, Y., Cook, P.G., Simmons, C.T., Partington, D., Crosbie, R., Batelaan, O., 2018.  
916 Uncertainty of groundwater recharge estimated from a water and energy balance model.  
917 *J. Hydrol.* 561, 1081–1093.

- 918 Yang, P., Yuan, D., Ye, X., Xie, S., Chen, X., Liu, Z., 2013. Sources and migration path of  
919 chemical compositions in a karst groundwater system during rainfall events. *Chinese Sci.*  
920 *Bull.* 58, 2488–2496.
- 921 Yang, Y. 2001. A study on the structure of karst aquifer medium and the groundwater flow in  
922 Houzhai underground river basin. *Carsologica Sinica* 20(1). (In Chinese)
- 923 Yao, C.Q., 2006. Simulation of Watershed Land-Surface Hydrological Process and its  
924 Integration with GIS. PHD's thesis, Beijing Normal University (in Chinese).
- 925 Yao, F., Sun, J., Tang, C., Ni, W., 2011. Kinetics of ammonium, nitrate and phosphate uptake  
926 by candidate plants used in constructed wetlands, in: *Procedia Environmental Sciences.*  
927 10, 1854-1861.
- 928 Yu, J.B., Yang, L.Z., Zhang, H.S., Fang, M.Z., Xing, F.M., 1990. The study of development  
929 regularity of karst in China - Water resources evaluation and exploitation in karst region  
930 in south of Puding in Guizhou Province. Science Press of China. (In Chinese).
- 931 Yue, F.J., Li, S.L., Liu, C.Q., Lang, Y.C., Ding, H., 2015. Sources and transport of nitrate  
932 constrained by the isotopic technique in a karst catchment: an example from Southwest  
933 China. *Hydrol. Process.* 29, 1883–1893.
- 934 Yue, F.-J., Waldron, S., Li, S.-L., Wang, Z.-J., Zeng, J., Xu, S., Zhang, Z.-C., Oliver, D.M.,  
935 2019. Land use interacts with changes in catchment hydrology to generate chronic nitrate  
936 pollution in karst waters and strong seasonality in excess nitrate export. *Sci. Total*  
937 *Environ.* 696, 134062.
- 938 Zeng, J., 2018. Chemical characterization of rainwater and spatial-temporal variation of  
939 nitrogen deposition in a small Karst catchment, Master's thesis, Guizhou University (in  
940 Chinese).
- 941 Zhang, W., Li, Y., Zhu, B., Zheng, X., Liu, C., Tang, J., Su, F., Zhang, C., Ju, X., Deng, J.,  
942 2018. A process-oriented hydro-biogeochemical model enabling simulation of gaseous  
943 carbon and nitrogen emissions and hydrologic nitrogen losses from a subtropical  
944 catchment. *Sci. Total Environ.*
- 945 Zhang, Y., Gao, Y., Yu, Q., 2017a. Diffuse nitrogen loss simulation and impact assessment of  
946 stereoscopic agriculture pattern by integrated water system model and consideration of  
947 multiple existence forms. *J. Hydrol.* 552, 660–673.
- 948 Zhang, Y., Shao, Q., 2018. Uncertainty and its propagation estimation for an integrated water  
949 system model: An experiment from water quantity to quality simulations. *J. Hydrol.* 565,  
950 623–635.



- 951 Zhang, Y.Y., Shao, Q.X., Ye, A.Z., Xing, H.T., Xia, J., 2016. Integrated water system  
952 simulation by considering hydrological and biogeochemical processes: model  
953 development, with parameter sensitivity and autocalibration. *Hydrol. Earth Syst. Sci.* 20,  
954 529–553.
- 955 Zhang, Z., Chen, X., Cheng, Q., Soulsby, C., 2019. Storage dynamics, hydrological  
956 connectivity and flux ages in a karst catchment: conceptual modelling using stable  
957 isotopes. *Hydrol. Earth Syst. Sci.* 23, 51–71.
- 958 Zhang, Z., Chen, X., Ghadouani, A., Shi, P., 2011. Modelling hydrological processes  
959 influenced by soil, rock and vegetation in a small karst basin of southwest China. *Hydrol.*  
960 *Process.* 25, 2456–2470.
- 961 Zhang, Z., Chen, X., Soulsby, C., 2017b. Catchment-scale conceptual modelling of water and  
962 solute transport in the dual flow system of the karst critical zone. *Hydrol. Process.* 31,  
963 3421–3436.
- 964 Zhang, Z., Chen, Xi, Chen, Xunhong, Shi, P., 2013. Quantifying time lag of epikarst-spring  
965 hydrograph response to rainfall using correlation and spectral analyses. *Hydrogeol. J.* 21,  
966 1619–1631.
- 967 Zhang, Z.C., Chen, X., Liu, J.T., Peng, T., Shi, P., Yan, X.L., 2012. Influence of terrain on  
968 epikarst in karst mountain- A case study of Chenqi catchment. *Earth and environment*,  
969 40(2):137-143. (In Chinese)
- 970
- 971



Distributed hydrological-nitrogen model in karst critical zone

## Highlights:

A novel distributed water-N model for karst catchment was developed

Tracer-aided model can significantly reduce equifinality effect of parameters

About 45% of N in surface stream and underground channel from epikarst

Sinkholes are important transport and export pathway of N in karst catchment

# 1 **Coupled Hydrological and Biogeochemical Modelling of Nitrogen** 2 **Transport in the Karst Critical Zone**

3 Zhicai Zhang<sup>1,3,7</sup>, Xi Chen<sup>2\*</sup>, Qinbo Cheng<sup>3</sup>, Siliang Li<sup>2</sup>, Fujun Yue<sup>2,5</sup>, Tao Peng<sup>4</sup>, Susan  
4 Waldron<sup>5</sup>, David Oliver<sup>6</sup>, Chris Soulsby<sup>7</sup>

5 <sup>1</sup>State Key Laboratory of Hydrology-Water Resources and Hydraulic Engineering, Hohai University, Nanjing  
6 210098, China

7 <sup>2</sup>Institute of Surface-Earth System Science, Tianjin University, Tianjin 300072, China

8 <sup>3</sup>College of Hydrology and Water Resources, Hohai University, Nanjing 210098, China

9 <sup>4</sup>Institute of Geochemistry Chinese Academy of Sciences, Guiyang, 550081, China

10 <sup>5</sup>School of Geographical and Earth Sciences, University of Glasgow, Glasgow G12 8QQ, United Kingdom

11 <sup>6</sup>Biological & Environmental Sciences, Faculty of Natural Sciences, University of Stirling, Stirling FK9 4LA,  
12 United Kingdom

13 <sup>7</sup>School of Geosciences, University of Aberdeen, Aberdeen AB24 3UF, United Kingdom  
14  
15

16 **Abstract** Transport of nitrogen (N) in karst areas is more complex than in non-karst areas due  
17 to marked heterogeneity of hydrodynamic behaviour in the karst critical zone. Here, we  
18 present a novel, distributed, coupled hydrological-biogeochemical model that can simulate  
19 water and nitrogen transport in the critical zone of karst catchments. This new model was  
20 calibrated using integrated hydrometric, water stable isotope, and nitrogen-N concentration  
21 data at the outflow of Houzhai catchment in Guizhou province of Southwest China.  
22 Hydrological dynamics appears to control N load from the study catchment. Combining flow  
23 discharge and water stable isotopes significantly constrained model parameterisation and  
24 mitigate the equifinality effects of parameters on the simulated results. Karst geomorphology  
25 and land use have functional effects on spatiotemporal variations of hydrological processes  
26 and nitrogen transport. In the study catchment, agricultural fertilizer was the largest input  
27 source of N, accounting for 86 % of the total. Plant uptake consumed about 45 % of inputs,  
28 primarily in the low-lying valley bottom areas and the plain covered by relatively thick soils.

29 Thus, a large amount of N released from soil reservoirs to the epikarst (via fractures or  
30 sinkholes) is then exported to the underground channel in the limestone area to the south. This  
31 N draining into groundwater could lead to extensive, potentially long-term contamination of  
32 the karst system. Therefore, improving the efficiency of fertilization and agricultural  
33 management in valleys/depressions is an urgent need to reduce N losses and contamination  
34 risk.

35

## 36 **1. Introduction**

37 Carbonate bedrock is a significant continental surface, comprising ~12 % of ice-free land  
38 and providing water resources for about 25 % of the Earth's population (Ford and Williams,  
39 1989). The southwest China karst region is one of the largest globally continuous karst areas,  
40 covering  $\sim 540 \times 10^3 \text{ km}^2$  over eight provinces. Agro-forestry and mineral extraction dominate  
41 land use, with subsistence-agriculture where soils exist (terraced gentler hillslopes/valley  
42 floors), and forest in uncultivated steeper mountains. From ~1950-1980 deforestation for  
43 creating cultivation space caused accelerated soil erosion, a changed hydrological balance and,  
44 shaped by agricultural practices, poorer water quality. Anthropogenic N fluxes have also been  
45 increasing as a result of population growth, agricultural intensification, fossil fuel-related acid  
46 deposition in industrialised- and agriculturally-intensified regions. Moreover, significant soil  
47 percolation and subsequent rapid preferential flow in the critical zone provides limited  
48 buffering for contaminant attenuation before re-emergence. It is therefore important to  
49 understand what controls water quality, and the source and attenuation of contaminants in this  
50 sensitive landscape. Models can help understanding of how nitrogen is cycled and transported

51 and the key factors and processes that control its dynamics. Modelling results provide  
52 quantitative estimates of how a system will respond to changes in pollutant inputs to aid  
53 environmental management (Ranzini et al., 2007).

54 The transfers of N in karst areas are more complex than those in non-karst areas because  
55 of the marked spatial heterogeneity of hydrodynamic behaviour. Lumped parameter models  
56 conceptualising reservoirs of the critical zone in series and/or parallel have been popularly  
57 used to simulate flow and nitrate movements and its biogeochemical reaction in karst areas  
58 (Husic et al., 2019). However, these lumped models lack functionality in relation to the spatial  
59 heterogeneity of hydrological-N processes characterising karst landforms, geology and land  
60 cover. Distributed hydrological-nutrient models, like SWAT (Arnold et al., 1998), have been  
61 widely used to simulate hydrological and nutrient responses to changes of land surface  
62 conditions. Expanding the grid-pattern hydrological model functions using process-oriented  
63 biogeochemical modules, such as the DeNitrification-DeComposition (DNDC) module (Li et  
64 al., 2000), facilitates comprehensive simulation of nitrogen transformation, vertical movement  
65 of water and nitrogen in soils and effluxes of carbon and nitrogen gases (Ferrant et al., 2011;  
66 Zhang et al., 2016, 2017a; Zhang et al., 2018). However, these models are developed for  
67 matrix flow systems therefore cannot be directly applied in karst areas. In karst areas, the high  
68 permeability of rock fractures leads to considerable changes in water storage and water age by  
69 facilitating mixing of new and old water during rainfall events (Zhang et al., 2019).  
70 Channelled flow in sub-surface conduits also exchanges reversibly with small fractures in the  
71 surrounding matrix depending on the hydraulic gradient between them (Hartmann et al.,  
72 2014). Sinkholes are special features in karst areas, which receive both diffused and

73 concentrated autogenic recharge, and then drain through a shaft or an underlying solution  
74 conduit (Tihansky, 1999). Therefore, over different, linked porous media, biogeochemical  
75 processing capacities can vary drastically (Jones and Smart, 2005; Opsahl et al., 2017; Yue et  
76 al., 2015). Until now, only a few models can appropriately delineate the unique  
77 hydrological-nitrogen cycle of karst systems.

78 A particular challenge in coupled hydrological-biogeochemical modelling is the  
79 increased risk of equifinality as model parameters increase (Zhang et al., 2016; Zhang and  
80 Shao, 2018). However, recently using tracer-aided models has helped ensure robust  
81 hydrological modules in coupled models. Using water stable isotopes or other tracers (e.g.  
82 chloride) in calibration, in addition to the more commonly used target of flow, can help  
83 constrain parameterisation at the catchment scale whilst giving increased confidence of  
84 accurate process representation of runoff sources (Birkel et al, 2015).Tracer-aided models can  
85 also strengthen conceptualisation of hydrological functions and transport of water particles, in  
86 terms of water age, dominant flow paths and hydrological connectivity in different model  
87 compartments. Such quantitative hydrological understanding can be functionally linked to  
88 solute transport in water quality models (McDonnell and Beven, 2014; Sprenger et al., 2015).  
89 These advantages of stable isotopes have been successfully exploited in enhancing the  
90 reliability of modelling dominant hydrological processes in non-karst catchments (Soulsby et  
91 al., 2015; Piovano et al., 2018) - but the efficiency of the tracer-aided functions applied in the  
92 hydrological-biogeochemical model in karst catchments is unknown.

93 Our previous work in the Chenqi catchment, a sub-catchment of the Houzhai catchment,  
94 Guizhou province of Southwest China, has focused on a typical karst landscape and

95 associated karst critical zone architecture (Vertically, the earth critical zone refers to a  
96 permeable layer from the tops of the trees to the bottom of the groundwater. Here, karst  
97 critical zone encompasses vegetation, soils, epikarst and deep aquifer.). In this prior work, we  
98 developed a distributed hydrological model (Zhang et al. 2011). In this study, we extend this  
99 model to facilitate multi-criteria calibration based on detailed observations of water stable  
100 isotope composition; we also couple biogeochemical modules to the hydrological structure to  
101 simulate spatially distributed fluxes of N, and apply the model to the larger Houzhai  
102 catchment. We address the three questions: (1) How do interacting karst geomorphological  
103 features, such as fractures and conduits, sinkholes, and surface streams and subsurface  
104 channel, control hydrological-nitrogen processes? (2) How effective is the tracer-aided model  
105 in reducing modelling uncertainty? (3) How much N in the catchment N budget is contributed  
106 from different sources in the critical zone and from different land uses?

107

## 108 **2. Study area and Data**

### 109 *2.1. Study area and descriptions of critical zone structure*

#### 110 *2.1.1 Study area*

111 The Houzhai catchment, located in Puding County, Guizhou Province of southwest  
112 China, has an area of 73.5 km<sup>2</sup> (Fig.1). The site has a subtropical wet monsoon climate. The  
113 mean annual temperature is 20.1<sup>0</sup>C. The highest monthly average temperature is in July, and  
114 the lowest is in January. Annual precipitation is 920 mm, with a distinct summer wet season  
115 and a winter dry season. Monthly average humidity ranges from 74 % to 78 %. The lithology  
116 is ~90 % Triassic argillaceous limestone and dolomite. The elevation of the study area varies



117 from 1218 to 1565 m above sea level, high in the east and low in the west (Fig.1). The karst  
118 topography in this catchment includes many exposed funnels and sinkholes and a  
119 well-developed underground channel network. Buried karst is located in the valleys and  
120 poljes, which are surrounded by karst mountainous peaks. The east mountainous area has the  
121 typical cone and cockpit karstic geomorphology of southwest China. The cone peaks are  
122 generally 200-300 m above the adjacent sinkhole depressions while the cone surface relief  
123 and slope are much steeper.

#### 124 *2.1.2 Vegetation and soils*

125 The land use and cover in the catchment include forests (mostly a mix of trees and  
126 shrubs), cultivated fields, villages and open water (Fig.2a). The soils are classified as  
127 limestone soil, paddy soil, and yellow soil (Fig.2b). Field investigations of soil thickness  
128 and hydraulic properties have been undertaken. The soil thickness ranges 0~2.0 m,  
129 increasing from steep hillslope (0-50cm) to gentle plain areas (1-2m).

#### 130 *2.1.3 Epikarst*

131 Below soils or at the outcropping carbonate rocks, the uppermost layer of the rock is  
132 referred to as the “epikarst”. It develops close to the topographic surface through rapid  
133 dissolution (Williams, 2008). Field investigations of a rock profile in the eastern mountainous  
134 area (Fig.2c) showed that the epikarst zone underlying the thin soils is rich in fractures and  
135 conduits while density and volume of the fractures generally decrease with increasing depth  
136 from ground surface (Zhang et al., 2013). Some infiltrated water can become perched in the  
137 epikarst zone as the porosity and permeability below decline markedly (Klimchouk, 2004).  
138 The distribution of epikarst thickness across the catchment was investigated at five profiles

139 (Fig.2c) using GPR (MALA Professional Explorer (ProEx) System) with a RTA 100-MHz  
140 antenna frequency and the software of Reflexw. The radargrammes clearly identify the  
141 thickness of the weathered zone, for example, the purple colour represents a low propagation  
142 velocity of electromagnetic waves in the ground for A and B profiles, and the zone with  
143 intensive changes of colour is characterized by strong fractured rocks.

144 From these profiles and the established relationship between the epikarst thickness and  
145 terrain curvatures (Zhang et al., 2012), the epikarst thickness in the entire catchment was  
146 interpolated using a digital elevation model (DEM) data derived from the 1:10 000 digital  
147 topography map in the catchment. The generated depth of epikarst zone ranges from 7 to 28  
148 m (Fig.2c), shallower in the eastern mountains and deeper in the western plains.

#### 149 *2.1.4 Deep aquifer*

150 The aquifer system consists mainly of limestone and dolomite of the Middle Triassic  
151 Guanling Formation (Fig.2d). The degree of inclination of the strata in this formation is  
152 between 5° and 25° to the northwest. The Middle Triassic Guanling Formation can be divided  
153 into T<sub>2g</sub><sup>1</sup>, T<sub>2g</sub><sup>2</sup>, and T<sub>2g</sub><sup>3</sup> (A-B section in Fig.2d) from the oldest to the youngest according to  
154 the combined characteristics of the lithology (Yang, 2001). The karst fissures and conduits are  
155 well developed in the aquifers. In particular, dense conduits can be found in the south  
156 limestone area (Yang et al., 2001). The groundwater depth decreases from more than 10 m in  
157 the east to ~2 m in the west, following the topography (Fig 3d). The aquifer boundary is  
158 similar to the catchment boundary except in the south where less than 5% of water is lost to a  
159 neighbouring catchment through conduits (Yu et al., 1990). The catchment mean recharge  
160 coefficient (recharge amount divided by precipitation) is about 0.47 (Yu et al., 1990). A large

161 proportion of the infiltration and percolation comes from direct runoff and sinking streams  
162 (allogenic recharge from the surrounding areas) in the rain season. The aquifers mostly are  
163 unconfined, however, they are markedly heterogeneous (Yu et al., 1990), with both  
164 subsurface flow of low velocity in the matrix (small fissures and fractures) and fast flow  
165 velocity in the karst conduits. Consequently, spatio-temporal variability in the water table is  
166 extremely high (Chen et al., 2018).

#### 167 *2.1.5 Sinkhole in connection with deep aquifer*

168 Sinkholes usually develop in terrain depression areas (Kruse et al, 2006), which overlie  
169 the underground channel. In the study catchment, 47 sinkholes have been identified based on  
170 the field investigations (Fig.1). Based on a DEM, the flow direction tool in ARCGIS is used  
171 to create a direction raster that identifies the drainage area of every sinkhole in the study area  
172 (Fig.1). Fourteen sinkholes in the eastern mountainous area are identified with a total area of  
173 8.22 km<sup>2</sup>, which accounts for 11 % of the total catchment area. The smallest and largest  
174 sinkhole drainage areas are 0.17 and 1.53 km<sup>2</sup>, respectively. The total area of the 33 sinkholes  
175 in the western plain area is 1.64 km<sup>2</sup>, which accounts for only 2 % of the total catchment area.  
176 Therefore, the western sinkholes collect less storm flow compared to the eastern sinkholes  
177 (Yu et al., 1990). Additionally, the western sinkholes are mainly produced by the collapse of  
178 rocks overlying the underground channel and drain small areas. They take a similar function  
179 in receiving storm flow as the underground channel does. Therefore, among the 47 sinkholes  
180 in the catchment (Fig.1), the 14 in the east are used for flow routing and the remaining 33  
181 sinkholes in the western area are ignored.

#### 182 *2.1.6 Surface stream and underground channel*

183 The Houzhai catchment consists of a surface stream in the north and a main underground  
184 channel in the south (Fig.1). The surface stream, incised an average depth of 2 m below the  
185 ground surface, is formed in the relatively thick yellow soil in the north (Fig.2b). The surface  
186 stream is usually dry in drought periods due to the high streambed infiltration into the  
187 underlying carbonate aquifer. Only during the flood periods, does the surface stream receive  
188 storm water, which flows from two main tributaries to the Qingshan (QS) reservoir and  
189 finally to the outlet of the Houzhai River.

190 The underground channel originates in the eastern mountains where most surface and  
191 subsurface flow recharges into the underground drainage network through the eastern  
192 sinkholes. The depth of the deep flow zone (underground channel bed or catchment lower  
193 boundary) is about 20-40 m below the ground surface (Fig 3d) (Yu et al., 1990). The upper  
194 mountainous region is rich in sinkholes or funnels, which are directly linked with the  
195 underground channels, resulting in a responsive hydrograph. When the underground channel  
196 reaches the broad and flat plains in the middle and lower catchment, underground flow is  
197 more attenuated (Chen et al., 2008).

#### 198 *2.1.7 Catchment sub-division and grid-scale flow routing*

199 For grid routing of the hydrological-nitrogen model, the catchment was divided into a  
200 rectangular grid of 100 m  $\times$  100 m resolution, totalling 13,000 pixels (104 rows by 125  
201 columns). All the attributes of vegetation, soils, epikarst, and deep zone are assigned in the  
202 pixels. The surface stream network is generated automatically following the Horton ordering  
203 scheme according to terrain using ARC/INFO. The surface stream width ranges 2–8 m and  
204 the depth of the stream bed ranges 1–2.5 m. The underground channel network is manually

205 delineated in terms of field investigation of underground channel information. The  
206 underground channel width and depth are approximately 1.5 and 1 m, respectively.  
207 ARC/INFO macros are used to subdivide the surface stream and underground channel  
208 networks into reaches and to order the cascade branches for the flow routing.

## 209 *2.2. Hydrochemical observations and analysis*

210 In the Houzhai catchment, two automatic weather stations were established at Chenqi  
211 (CQ) and Laoheitan (LHT) (Fig.1) to record precipitation, air temperature, wind, radiation, air  
212 humidity and pressure. The meteorological data and underground channel discharge  
213 collection was from 1 March 2016 to 31 December 2017. The discharges of the surface  
214 stream and underground channel at the catchment outlet were measured with weirs (Fig.1).  
215 Water levels were automatically recorded by a HOBO U20 water level logger (Onset  
216 Corporation, USA) with a time interval of 15 minutes. The discharge in the surface stream  
217 was measured from 1 January 2017 to 31 December 2017.

218 Rainwater and surface stream and subsurface channel water at catchment outlets were  
219 daily sampled between 1 June 2016 and 31 December 2017. All water samples were collected  
220 in 5 ml glass vials. The stable isotope ratios of  $\delta\text{D}$  and  $\delta^{18}\text{O}$  were determined using a MAT  
221 253 laser isotope analyser (instrument precision of  $\pm 0.5\text{‰}$  for  $\delta\text{D}$  and  $\pm 0.1\text{‰}$  for  $\delta^{18}\text{O}$ ).  
222 Water stable isotope ratios are reported in the  $\delta$ -notation using the Vienna Standard Mean  
223 Ocean Water standards.  $\text{NO}_3\text{-N}$  concentrations ( $[\text{NO}_3\text{-N}]$ ) at the surface and underground  
224 channel outlets were measured using non-optical NISE sensor with a time interval of 15  
225 minutes from 1 June 2016 to 30 September 2017 (Yue et al, 2019).  $\text{NH}_4\text{-N}$  concentrations  
226 were measured several times during June ~ July 2016.

227 The discharge, isotopic and NO<sub>3</sub>-N concentrations show great variability (Fig.3). From  
228 statistical characteristics of these variables (Table 1), the mean of underground channel  
229 discharge is over double that of surface stream discharge while temporal variability of  
230 underground channel discharge is much lower than that of surface stream discharge (see CV  
231 and Mode in Table 1). The  $\delta D$  ratios of underground channel tend to be less variable than  
232 surface stream flow, implying lower influence of young waters. This is particularly apparent  
233 for heavy rainfall events (corresponding to the minimum  $\delta D$  value in Table 1) where the  
234 young water influence in the underground channel flow is much less than surface stream flow.  
235 This suggests that the isotopic responses of underground channel flow and surface stream  
236 flow to rainfall are similar in most periods, and only in the heavy rainfall periods, is the  
237 surface stream flow newer than underground channel flow.

238 In terms of mean and maximum values in Table 1, N loading mostly comes from  
239 underground channel flow but the peak flow of surface waters can carry the largest N loading.  
240 Interestingly, N loading increases linearly with discharge for both surface stream and  
241 underground channel (Fig.4), which indicates that variations of the N fluxes are directly  
242 proportional to flow. Thus, accurate simulation of hydrographs for  
243 hydrological-biogeochemical modelling is vital in this karst landscape. The local meteoric  
244 water line (LMWL) is derived from the regression between  $\delta^{18}O$  and  $\delta D$  values of daily  
245 precipitation data sampled between July 2016 and December 2017. The dual-isotope plot  
246 shows great evaporative fractionation effects on underground channel flow than surface  
247 stream (Fig.5). The lower slope of underground channel flow illustrates that groundwater in  
248 the deep zone mixes more heavy isotopes during infiltration and percolation.

249 Monthly wet deposition of  $\text{NH}_4\text{-N}$  and  $\text{NO}_3\text{-N}$  ranged from 0.2-2.6 mg/L for  $\text{NO}_3\text{-N}$  and  
250 0.42-5.8 mg/L for  $\text{NH}_4\text{-N}$ , and monthly dry N deposition was 0.26 kg/ha (Zeng, 2018).  
251 Annual fluxes and seasonal distribution of litter fall were estimated drawing on understanding  
252 from another basin in Guizhou Province with similar vegetation distributions and geographic  
253 conditions (Pi, 2017). Annual fluxes of litter fall range 1.47-3.61 t/ha<sup>-yr</sup> and the C/N ratios are  
254 18.7-33.1 for forest. The non-point source inputs of N for farm land (paddy and rapeseed) are  
255 estimated to be ~270kg kg/ha<sup>-yr</sup> (from field surveys by the Karst Ecosystem Research Station  
256 of the Institute of Geochemistry in Puding). Leguminous crops are the main N fixation plants,  
257 which fix N via symbiotic anaerobic microorganisms (Cheng, 2008). Therefore, for this  
258 model, it is assumed that N-fixation occurs primarily with bean crops, and from field survey  
259 in this catchment the fraction of bean crop in each pixel was set to 0.04 in the cultivated land.  
260 The rate of annual N fixation by pure stands of bean was set to 40 kg N/ ha<sup>-yr</sup> (based on Smil,  
261 1999). The potential denitrification fluxes are  $6.2 \times 10^{-8}$  and  $1.3 \times 10^{-6}$  kgN/m<sup>2</sup>·h for forest and  
262 farm land, respectively (Barton et al. 1999).

263

### 264 **3. Model description and Execution**

265 The original distributed hydrology-soil-vegetation model (DHSVM) includes a two-layer  
266 Penman-Monteith formulation and a two-layer energy balance model for canopy  
267 evapotranspiration and ground snow pack, respectively. It contains a multilayer unsaturated  
268 soil model, a saturated subsurface flow model, and a grid-based overland flow routing  
269 (Wigmosta et al. 1994). The model was subsequently expanded to integrate a biogeochemical  
270 module (the DHSVM Solute Export Model, D-SEM) (Thanapakpawin, 2007). To

271 accommodate the special karst geomorphological features, like sinkholes, epikarst and deep  
 272 aquifers, Zhang et al. (2011) adapted the DHSVM structure for application in Chenqi  
 273 catchment. The vertical layers of the model are divided to represent vegetation, soils, epikarst,  
 274 and deep aquifers according to descriptions of karst structure given by Perrin et al. (2003).  
 275 The flow routing includes sinkhole functions in collecting local surface and subsurface flow  
 276 in soils and the epikarst zone, and directly connecting these with underground channel  
 277 outflow (Fig.6). In this study, the N routings are improved accordingly by conceptualising the  
 278 above karst geomorphologic functions (Fig.6), in addition to integrating the mass balance  
 279 routings and biogeochemical reaction calculations proposed by Thanapakpawin (2007).

280

### 281 3.1. Hydrological simulation

282 In the three zones of soils ( $s$ ), epikarst ( $e$ ) and deep flow zone ( $d$ ), the flow routings are  
 283 based on water balance equations for every grid cell in the catchment:

$$284 \quad \frac{d\theta_s}{dt} d_s = P_0 - P_s(\theta) - E_{to} - E_{tu} - E_s + V_e + (Q_{s,in} - Q_{s,out}) - V_s \quad (1)$$

$$285 \quad \frac{d\theta_e}{dt} d_e = P_s(\theta) - P_e(\theta) - E_{to} + V_d + (Q_{e,in} - Q_{e,out}) - V_e \quad (2)$$

$$286 \quad \frac{d\theta_d}{dt} d_d = P_e(\theta) + (Q_{d,in} - Q_{d,out}) - V_d \quad (3)$$

287 where  $\theta_n$  is soil moisture and  $d_n$  is thickness ( $n=s, e, d$ );  $P_n$  is infiltrated rainfall ( $n=0$ ) or  
 288 percolated water ( $n=s, e$ );  $E_{to}$  are  $E_{tu}$  evapotranspiration from over story( $o$ ) and understory  
 289 vegetation ( $u$ ), respectively;  $E_s$  is soil evaporation;  $Q_{n,in}$  and  $Q_{n,out}$  are subsurface flow that  
 290 passes into and out of the soil, epikarst and deep conduit flow zone, respectively;  $V_n$  is return  
 291 flow.

292 Vertical infiltration and percolation in the soil ( $P_s$ ) are estimated based on Darcy's Law



293 assuming a unit hydraulic gradient and using an equivalent hydraulic conductivity as  
 294 described by Brooks-Corey (1964) for the soils. The “cubic law” is used for estimation of  
 295 infiltration and percolation of the rock fractures in epikarst ( $P_e$ ). The spatial distributions of  
 296 the rock fractures are stochastically generated according to field investigations of fractural  
 297 characteristics, such as density, length and direction (details in Zhang et al., 2011). The  
 298 subsurface flow ( $Q_{n,in}$ ,  $Q_{n,out}$ ,  $n=s, e, d$ ) is calculated cell-by-cell in terms of hydraulic  
 299 transmissivity ( $T=Kd$ , where  $K$  is hydraulic conductivity, and  $d$  is thickness of each layer),  
 300 hydraulic gradient and the grid width and length ( $b_{cell}$  and  $L_{cell}$ ) at the grid in each flow  
 301 direction. For the cells within a sinkhole drainage area, surface flow or overland flow ( $Q_{sur}$ )  
 302 and subsurface flow ( $Q_s$  and  $Q_e$ ) directly recharge into the underground channel via the  
 303 sinkhole ( $Q_{sinkhole}$ ).

304 In the original DHSVM, flow in surface stream and the underground channel systems is  
 305 routed using a cascade of linear channel reservoirs (Wigmosta et al, 1994; Wigmosta and  
 306 Perkins, 2001). In the new adaptation of DHSVM, for the surface stream flow routing, the  
 307 lateral flow ( $Q_{surL}$ ) includes the loss of water as infiltration from the surface stream bed into  
 308 the underlying aquifer ( $Q_{inf}$ ), in addition to the gained water of overland flow ( $Q_{sur}$ ) and  
 309 subsurface flow in the soil zone ( $Q_s$ ):

$$310 \quad Q_{surL} = Q_{sur} + Q_s - Q_{inf} \quad (4)$$

$$311 \quad Q_{inf} = L_{cell} \cdot b_{cell} \cdot \alpha_{inf} \quad (5)$$

312 where  $L_{cell}$  and  $b_{cell}$  are length and width of surface stream segment in one cell, respectively.  
 313  $\alpha_{inf}$  is constant rate of the surface stream bed. For the underground channel flow routing, the  
 314 average rate of lateral flow ( $Q_{gL}$ ) includes the flows from the epikarst zone ( $Q_e$ ) and the deep

315 zone intercepted by the underground channel ( $Q_d$ ) when the cells are outside a sinkhole  
 316 drainage area:

$$317 \quad Q_{gL} = Q_e + Q_d \quad (6)$$

318 Otherwise, the lateral flow equals the sinkhole water collected ( $Q_{sinkhole}$ ):

$$319 \quad Q_{gL} = Q_{sinkhole} \quad (7)$$

### 320 3.2. Nitrogen simulation

#### 321 3.2.1. Mass balance of Nitrogen

322 Consistent with the hydrological module, the karst system is conceptualised as three  
 323 nitrogen reservoirs in the vertical dimension. The multilayer mass balance model accounts for  
 324 nitrogen dynamics in the soil, epikarst, and deep flow zones:

$$325 \quad \frac{dM_s}{dt} = M_{sur-s} - M_{s-e} - M_{s-sur} + (M_{s,in} - M_{s,out}) + \sum_{i=1}^{j_s} M_i \quad (8)$$

$$326 \quad \frac{dM_e}{dt} = M_{s-e} - M_{e-d} - M_{e-s} + (M_{e,in} - M_{e,out}) + \sum_{i=1}^{j_e} M_i \quad (9)$$

$$327 \quad \frac{dM_d}{dt} = M_{e-d} - M_{d-e} + (M_{d,in} - M_{d,out}) + \sum_{i=1}^{j_d} M_i \quad (10)$$

328 where  $M_n$  is solute mass ( $n=s, e, d$ );  $M_{n,in}$  and  $M_{n,out}$  are mass flux that passes in and out the  
 329  $n$ th zone, respectively;  $\sum_{i=1}^{j_e} M_i$  ( $j=s, e, d$ ) is biogeochemical mass; subscripts of *sur-s*, *s-sur*,  
 330 *s-e*, *e-s*, *e-d* and *d-e* represent from surface to soil layer, soil layer to surface, soil layer to  
 331 epikarst, epikarst to deep flow zone, and deep flow zone to epikarst, respectively.

332 The solute concentration in each zone can be derived according to the mass ( $M_n$ ,  $n=s, e,$   
 333  $d$ ), the water volume ( $\theta_n$ ,  $n=s,e,d$ ), and the mass fluxes that pass in and out of each zone  
 334 ( $M_{n,in} / M_{n,out}$ ,  $n=s, e, d$ ). The mass fluxes draining through sinkholes into underground  
 335 conduits ( $M_{sinkhole}$ ) are calculated from the flows collected by the sinkhole ( $M_{sinkhole}$ )  
 336 multiplied by the solute concentration of the collecting water. The model tracks and simulates

337 the solute mass/concentration for each reservoir separately. The solute mass routing in stream  
 338 channel/underground conduit is based on mass balance:

$$339 \quad M_{out} = M_{in} + \Delta M_V + \sum_{i=1}^{j_V} M_i \quad (11)$$

$$340 \quad \sum_{i=1}^{j_V} M_i = M_{loss} = \phi C_{riv\_sur} Q_{riv\_sur} \quad \text{for surface stream} \quad (12)$$

$$341 \quad \sum_{i=1}^{j_V} M_i = 0 \quad \text{for underground channel} \quad (13)$$

342 where  $\Delta M_V$  is mass storage change;  $\sum_{i=1}^{j_V} M_i (j=s,e,d)$  is biogeochemical reaction mass;  
 343  $M_{loss}$  is retention mass of N in surface stream network;  $C_{riv\_sur}$  and  $Q_{riv\_sur}$  are  
 344 concentration of N and discharge of surface stream at each time step, respectively;  $\phi$  is  
 345 coefficient for retention mass of N. The model includes the effects of biogeochemical  
 346 processes on N concentrations ( $\sum_{i=1}^{j_V} M_i (j=s,e,d)$ ) in the stream channel, but biogeochemical  
 347 reactivity in the underground water is assumed to be negligible because nitrate is conservative  
 348 under the oxidizing conditions of many karst aquifer conduits (Perrin et al. 2007; Mahler and  
 349 Garner, 2009). The N loss in surface stream networks ( $M_{loss}$ ) is common (Li et al., 2019),  
 350 especially in reservoirs within stream networks. Lakebed sediments in reservoir systems can  
 351 sequester excess nutrients loaded by rivers through sedimentation (David et al., 2006;  
 352 Saunders and Kalff, 2001). Due to this effect, the reservoirs can be treated as overall sinks for  
 353 N consequently decreasing downstream nutrient loads (Bosch and Allan, 2008; Powers et al.,  
 354 2015; Han et al, 2017; Shaughnessy et al., 2019). Therefore, the retention of N in surface  
 355 stream networks affected by reservoirs was considered using a simple relationship when  
 356 reservoirs exist in the surface river network (Eq. 12).

357 Conservative tracers, such as stable isotopes of hydrogen and oxygen, can be regarded as  
 358 solutes unaffected by biogeochemical processes. Thus, if the multilayer mass balance model

359 is applied for the solute mass of the tracers, these equations (Eqs. 8 and 10) can be simplified  
 360 by neglecting the biogeochemical reactions ( $\sum_{i=1}^{jv} M_i=0$ ). Even though stable isotope mass  
 361 equations add two additional parameters (fractionation coefficients of  $\tau_s$  and  $\tau_e$  in soil and  
 362 epikarst layer, respectively) for considering isotopic fractionation by evaporation (Fig.6) in  
 363 the soil and epikarst, the isotopic tracer observations can be used to track hydrological  
 364 processes and constrain the calibration parameters:

$$365 \quad M_{s,out} = C_{iso,s} \tau_s (E_{t0} - E_{tu} - E_s) \quad (14)$$

$$366 \quad M_{e,out} = C_{iso,e} \tau_e E_{t0} \quad (15)$$

367 where  $C_{iso,s}$  and  $C_{iso,e}$  are water stable isotope compositions for soil and epikarst,  
 368 respectively.

### 369 3.2.2. Nitrogen sources and Biogeochemical processes

370 Four major N sources are represented in the model: atmospheric deposition,  
 371 anthropogenic non-point sources, biological N fixation and litter fall. In each time step, the  
 372 load of atmospheric deposition N is equal to the product of actual deposition concentration  
 373 and precipitation. Non-point sources, such as fertilizers, are represented on a pixel basis  
 374 directly. The N-fixation is estimated by (Binkley *et al.*, 1994):

$$375 \quad N_{fix} = N_f \cdot \Phi_{T,fix} \quad (16)$$

376 where,  $N_f$  is Nitrogen Fixing Reference Rate;  $\Phi_{T,fix}$  is temperature factor for fixation.  
 377 Vegetation residue pools from litterfall are divided into a recalcitrant structural pool and a  
 378 rapidly decomposable metabolic residue pool, each with different decay rates and carbon to  
 379 nitrogen (C/N) ratios. The N from decomposed litterfall ( $N_{litter}$ ) is simulated by using a first  
 380 order rate equation, which is added to the ammonium pool (Inamdar *et al.*, 1999):

381 
$$N_{litter} = A \cdot M / (1 + C/N) \cdot \Phi_{T,lit} \cdot \Phi_{\theta,lit} \quad (17)$$

382 where  $A$  is cell area;  $M$  is litter mass;  $\Phi_{T,lit}$  is temperature factor for litterfall;  $\Phi_{\theta,lit}$  is  
 383 moisture factor for litterfall. Soil organic N is not a major source of nitrate in the water  
 384 samples considering the thin soil profile and rapid water movement in the karst system (Liu et  
 385 al., 2009). Therefore, to reduce the complexity, the organic N processes is not considered in  
 386 the model focusing primarily on inorganic nitrogen.

387 Once the N enters soils, it is subject to changes due to biogeochemical processes. After  
 388 biogeochemical transformation for each time step is completed, the dissolved portion of the  
 389 pool drains into the surface and underground stream networks. The total amount of  
 390 nitrification ( $N_n$ ) and ammonia volatilization ( $N_{n-v}$ ) is calculated and then partitioned, using a  
 391 combination of the methods developed by Reddy *et al.* (1979) and Godwin *et al.* (1984):

392 
$$N_{n-v} = (1 - \exp(-\Phi_n - \Phi_v)) \cdot [NH_4]_L \cdot \frac{1}{24} \quad (18)$$

393 where  $\Phi_n = \Phi_{T,n} \cdot \Phi_{\theta,n} \quad (19)$

394 
$$\Phi_{T,n} = \begin{cases} 0 & T \leq 4 \\ 2^{\frac{T-O_t}{10}} & 4 < T < O_t \\ 1 & T \geq O_t \end{cases} \quad (20)$$

395 and  $\Phi_v = \Phi_D \cdot \Phi_{T,n} \quad (21)$

396 where  $[NH_4]_L$  is mass of  $NH_4$ ;  $\Phi_{T,n}$  is temperature factor for nitrification, controlled by  
 397 temperature ( $T$ ) and the parameter of optimum temperature ( $O_t$ );  $\Phi_{\theta,n}$  is moisture factor for  
 398 nitrification controlled by water content. Then, the nitrification  $N_n$  is estimated by:

399 
$$N_n = N_{n-v} \cdot \frac{1 - \exp(-\Phi_n)}{1 - \exp(-\Phi_n) + 1 - \exp(-\Phi_v)} \quad (22)$$

400 The calculation of denitrification ( $N_d$ ) is modified from Hénault and Germon (2000):

401 
$$N_d = D_p \cdot \Phi_{T,d} \cdot \Phi_{No3} \cdot \Phi_{\theta,d} \quad (23)$$

402 and  $\Phi_{\theta,d} = \begin{cases} 0 & f_{sat} < D_{st} \\ \left(\frac{f_{sat}-0.62}{0.38}\right)^{1.74} & f_{sat} \geq D_{st} \end{cases}$  (24)

403  $\Phi_{NO_3} = \frac{[NO_3]}{(R_{hs}+[NO_3])}$  (25)

404 where  $D_p$  is potential denitrification flux;  $\Phi_{T,d}$  is temperature factor for denitrification  
 405 controlled by temperature;  $\Phi_{\theta,d}$  is moisture factor for denitrification controlled by parameter  
 406 of denitrification saturation threshold ( $D_{st}$ );  $f_{sat}$  is soil moisture saturation extent;  $\Phi_{NO_3}$  is  
 407 nutrient factor controlled by nitrate reduction half saturation fraction ( $R_{hs}$ ).

408 Michealis-Menton saturation kinetics are assumed to be the mechanics of plant  $NH_4$ -N  
 409 uptake ( $NH_{4, uptake}$ ) (Yao et al., 2011; Bicknell et al., 1993), and its calculation includes the  
 410 parameters of Half-rate Ammonium Uptake Constant ( $Au$ ) and Maximum Ammonium Uptake  
 411 Constant ( $Aum$ ):

412  $NH_{4, uptake} = \frac{Aum \cdot [NH_4]_L}{Au + [NH_4]_L} A$  (26)

413 For  $NO_3$ -N uptake ( $NO_{3, uptake}$ ), the model used is a modified yield-based approach, with the  
 414 parameters of Maximum Nitrogen Uptake Delay ( $Num$ ) and Maximum Nitrogen  
 415 Accumulation ( $Nam$ ):

416  $NO_{3, uptake} = Nam \cdot \frac{\exp\left(-\frac{((t)_c - t_{sta} - Num)^2}{2 \cdot \left(\frac{t_{long}}{3}\right)^2}\right)}{\left(\frac{t_{long}}{3}\right) \cdot \sqrt{2\pi}}$  (27)

417 where  $t_c$  is current day;  $t_{sta}$  is growing season start day;  $t_{long}$  is growing season length.

418 A simplified scheme to represent sorption as a function of  $NO_3$ -N ( $NO_{3, sorption}$ ) and  $NH_4$ -N  
 419 ( $NH_{4, sorption}$ ) mass was used in the model:

420  $NO_{3, sorption} = M_{NO_3} \cdot N_a$  (28)

421  $NH_{4, sorption} = M_{NH_4} \cdot A_a$  (29)

422 where  $M_{NO_3}$  and  $M_{NH_4}$  are  $NO_3$  and  $NH_4$  mass, respectively;  $N_a$  is Nitrate Sorption Coefficient;  
423  $A_a$  is Ammonium Adsorption Coefficient.

424 These biogeochemical reactions are assumed to occur in the soil layer in non-karst areas  
425 (see Thanapakpawin (2007) for detail). In our modified model, the nitrification and  
426 denitrification of N occur in both the soil and epikarst zones.

427

### 428 *3.3. Modelling procedures*

429 All simulations were performed on hourly time steps, at a  $100 \times 100 \text{ m}^2$  resolution. The  
430 hourly discharge, daily water stable isotope composition and  $NO_3$ -N concentration were used  
431 for the model calibration. Automatic calibration of the coupled hydrological-N model at such  
432 a high spatiotemporal resolution is very time consuming. Therefore, the step-by-step method  
433 was employed for parameter estimation (Ferrant et al., 2011). The parameters of hydrological  
434 module are optimized first, and then parameters for biogeochemical reactions were manually  
435 calibrated using the optimized hydrological parameters.

436 The parameters of the hydrological module can be divided into sensitive and insensitive  
437 parameters (Yao, 2006; Kelleher et al., 2015). The insensitive parameters were determined as  
438 follows: (1) the vegetation-related parameters were determined by the field investigations,  
439 such as the height of 2.1 and 1 m for forest and crops, respectively; other parameters (e.g.  
440 *LAI*, albedo and root depth) were based on the Land Data Assimilation System (LDAS); (2)  
441 the soil-related parameters, such as bulk density, porosity and wilting point, were measured  
442 using field experiments and laboratory analysis (Cheng et al., 2011); and 3) the other  
443 insensitive parameters, such as pore size distribution, aerodynamic attenuation and moisture

444 threshold, were drawn from literature (e.g., Thyer et al., 2004; Kelleher et al., 2015). The  
445 sensitive parameters, e.g. hydraulic conductivities ( $K_h$  and  $K_v$ ), field capacity ( $\theta_f$ ) in the soils,  
446 epikarst and deep zones, and canopy fraction ( $C_f$ ) in Table 2, were calibrated against  
447 observations of discharge within the initial ranges of the sensitive parameter in Table 2. In  
448 order to reduce equifinality effects, these sensitive parameters together with two additional  
449 parameters (fractionation constants of  $\tau_s$  and  $\tau_e$  in Table 2) are further calibrated against  
450 observations of isotopic ratios.

451 The modified Kling–Gupta efficiency (KGE) criterion (Kling et al., 2012) was used as  
452 the objective function for flow and isotope calibrations. The criterion balances how well the  
453 model captures the dynamics (correlation coefficient), bias (bias ratio) and variability  
454 (variability ratio) of the actual response (Schaefli and Gupta, 2007). The objective functions  
455 of KGE for the surface stream and underground channel were combined to formulate a single  
456 measure of goodness of fit. Targeted on the flow discharge, the objective function is  $KGE_Q =$   
457  $(KGE_{Q-sur} + KGE_{Q-und}) / 2$  (where  $KGE_{Q-sur}$  and  $KGE_{Q-und}$  are the objective functions for  
458 surface stream and underground channel discharges, respectively). Targeted on the isotopic  
459 concentration, the objective function is  $KGE_i = (KGE_{i-sur} + KGE_{i-und}) / 2$  (where  $KGE_{i-sur}$  and  
460  $KGE_{i-und}$  are the objective functions for isotopic concentrations for surface stream and  
461 underground channel, respectively).

462 A Monte Carlo analysis was used to explore the parameter space during calibration and  
463 provides insight to the resulting uncertainty. In order to derive a constrained parameter set,  
464 two iterations were carried out in the calibration. First, a total of 2000 different parameter  
465 combinations within the initial ranges was randomly generated as the possible parameter



466 combinations (Soulsby et al., 2015; Xie et al., 2018). After the first calibration using  $KGE_Q$   
467 and  $KGE_i > 0.3$  was used as a threshold for model rejection, and the range of each parameter  
468 was narrowed. Then, another 2000 different parameter combinations within the narrowed  
469 ranges were used as for the second calibration, and the parameter space was reduced by  
470 iteratively applying two criteria: 1) the discharge criterion discarded all parameter sets that  
471 obtain a  $KGE_Q < 0.75$ , and 2) the water stable isotope criterion discarded all parameter sets  
472 that obtain a  $KGE_i < 0.5$ . The retained parameter sets were further used for simulation of  
473 possible flow discharges and the tracer compositions, and their uncertainty bands. In addition  
474 to  $KGE$ , root mean squared error (RMSE) and absolute of average relatively error (aARE)  
475 were calculated for evaluation of the model performance.

476 After determining the best hydrological parameter set (it consists of the mean values of  
477 each parameter derived from the retained parameter sets after calibration), the N module  
478 parameters related to biogeochemical reactions (Table 3) were manually calibrated using the  
479 observed  $NO_3-N$  concentrations at the catchment outlets. The values of the biogeochemical  
480 parameters used in Thanapakpawin (2007) were taken as the initial values for model running.  
481 Then these parameters for biogeochemical reactions were calibrated against the best matching  
482  $NO_3-N$  concentrations measured at the outlets. Comparisons of the simulated and measured  
483  $NH_4-N$  concentrations at the catchment outlets were used as a “soft” validation of the  
484 simulations. This strategy of the model calibration was also used in other studies for the  
485 complex simulation of biogeochemical reactions (Zhang et al., 2016, 2017a).

486 The modelling period started on 1 March 2016, but calibration was initiated using  
487 available discharge data from 13 July 2016 and isotopes from 1 June 2016. The preceding

488 four months were therefore used as a spin-up period (the mean of precipitation isotope  
489 signatures over the sampling period was used for this) to fill storages, and initialise storage  
490 tracer and N concentrations.

491

## 492 **4. Results**

### 493 *4.1. Model performance*

494 The modelling results show that the discharge dynamics in surface stream and  
495 underground channel were mostly bracketed by the simulation ranges at the outlet though  
496 some discharges were not completely captured (Fig.7). The objective function values of the  
497 combined  $KGE_Q$  for flow discharge at the outlets were all greater than 0.75 for the 114  
498 retained parameter sets, with a maximal value of 0.81 and the mean of 0.77 over the study  
499 period. The maximal, mean and minimal objective function values were 0.8, 0.77 and 0.7,  
500 respectively, for surface stream discharge ( $KGE_{Q-sur}$ ), and 0.82, 0.78 and 0.72, respectively,  
501 for underground channel discharge ( $KGE_{Q-und}$ ). The mean of RMSE and aARE is 0.31 m<sup>3</sup>/s  
502 (0.23-0.39 m<sup>3</sup>/s) and 10% (6%~16%), respectively, for surface stream discharge, which is  
503 larger than 0.28 m<sup>3</sup>/s (0.21~0.35 m<sup>3</sup>/s) and 7% (4%~13%) for underground channel. The  
504 simulated results capture the surface stream flow during the heavy rainfall periods (Fig.7).

505 The simulated water stable isotope ratios show that the model generally reproduces the  
506 overall  $\delta D$  signal of surface stream and underground channel water during study period  
507 (Fig.8). The combined  $KGE_i$  for water stable isotope composition at the stream and  
508 underground channel outlets were all greater than 0.5, with a mean of 0.62 and maximal value  
509 of 0.67. The mean of RMSE and aARE is 8.9 ‰ (5.7-10.9 ‰) and 12% (8 ‰~19 ‰),

510 respectively, for surface stream discharge, which is larger than 5.6 ‰ (3.5~7.6 ‰) and 11 %  
511 (6 %~16 %) for underground channel. As is common in coupled flow-tracer models, the  
512 performance in the simulation of water stable isotopes was less satisfactory and more  
513 uncertain than for discharge (Table 4). There were some enriched “outliers” in underground  
514 channel water with high isotope values out of the uncertainty range (the maximum of  $\delta D$  less  
515 than -50 ‰). The most likely explanation for this is flooded paddy fields, which are  
516 extensively distributed in the depression during the growing season, this allows evaporative  
517 fractionation effects which are transferred to the channel network in larger events Zhang et al.,  
518 (2019).

519 Although the performance of the coupled flow-tracer model for isotope simulation was  
520 less accurate than for discharge simulation, targeting both the flow discharge and isotopic  
521 concentration (e.g. meeting  $KGE_Q \geq 0.75$  and  $KGE_i \geq 0.5$ ) can effectively narrow the  
522 parameter ranges and thus reduce equifinality effect of these additional parameters on the  
523 simulated results (Fig.9).

524 The calibrated parameters for modelled biogeochemical reactions for  $N$  are listed in  
525 Table 3. The modelled results with this parameter set show that the simulated daily  $NO_3-N$   
526 concentrations can generally capture the observations at the outlets of the surface stream and  
527 underground channel (Fig.10). The simulated uncertainty of  $NO_3-N$  is larger than that of  
528 discharge and isotopic profile as the model structure becomes more complex and the number  
529 of calibrated parameters increases. The  $KGE_{N-sur}$  and  $KGE_{N-und}$  for daily  $NO_3-N$   
530 concentrations were 0.45 and 0.5 at surface stream and underground outlets, respectively. The  
531 mean of RMSE and aARE is 1.06 mg/L and 14 % respectively for surface stream, both

532 greater than 0.37 mg/L and 12 %, respectively for underground channel. The larger deviation  
533 of the simulated N in surface river could result from complex flow regulation and  
534 biogeological processes in the reservoir (Wang et al., 2020).

535 The measured  $\text{NH}_4\text{-N}$  concentrations at the outlets were further used to test the model  
536 performance. Since the  $\text{NH}_4\text{-N}$  concentrations of water in the study area were very low ( $\sim 10^{-2}$   
537 mg/L) (smaller than the calculation errors of the mixing and biogeochemical processes of  
538  $\text{NH}_4\text{-N}$ ), the simulated results cannot capture variability but the magnitude of the simulated  
539 and measured concentrations is of the same order for both the surface stream and underground  
540 channel outlets (Fig.11). The mean measured and simulated  $\text{NH}_4\text{-N}$  concentrations are 0.05  
541 and 0.06 mg/L, and the total measured and simulated loadings of  $\text{NH}_4\text{-N}$  are 224 and 262 kg,  
542 respectively, for surface river during the observation period (a total of 30 days). For  
543 underground channel, both the mean measured and simulated  $\text{NH}_4\text{-N}$  concentrations are 0.05  
544 mg/L, and the total measured and simulated loadings of  $\text{NH}_4\text{-N}$  are 341 and 343 kg,  
545 respectively, over the observation period (a total of 38 days).

546

#### 547 *4.2. Vertical and spatial distributions of the simulated $\text{NO}_3\text{-N}$ storages*

548 Fig.12 shows the spatial distribution of simulated  $\text{NO}_3\text{-N}$  loadings (concentrations of  
549  $\text{NO}_3\text{-N}$  multiplied by the flux in each layer) in the three layers of the critical zone. Spatial  
550 variations of the  $\text{NO}_3\text{-N}$  loadings in soils are most marked because of spatial difference of soil  
551 thickness, hydraulic conductivity and land cover.  $\text{NO}_3\text{-N}$  loadings in the relatively thick soils  
552 in the western plain are mostly larger than those in the thin soils in the eastern mountains  
553 (Fig.12a). In spite of thin soils over the whole catchment, the soil layer was the largest  $\text{NO}_3\text{-N}$

554 store in the catchment (Fig.12). The average values of  $\text{NO}_3\text{-N}$  in the soil, epikarst and deep  
555 flow layers are 58.4, 18.6 and 15.3kg/ha, respectively. In each of the layers, the  $\text{NO}_3\text{-N}$   
556 loadings in the farm land are much larger than those in the forest areas (Fig.12d). For  
557 example, the annual  $\text{NO}_3\text{-N}$  loading is 452 and 40 t for the soil layers in the farm land and  
558 forest respectively. The greater  $\text{NO}_3\text{-N}$  loading in the farm land is mainly attributed to the  
559 high fertilization rates in this region (e.g. the  $\text{NO}_3\text{-Ns}$  for paddy soil and yellow soil were 67  
560 and 53 kg/ha, respectively).

561

#### 562 *4.3. Simulated exchanges of N fluxes in the critical zone and catchment N balance*

563 Fig.13 shows daily and cumulative net input and the simulated loss of N from 13 July  
564 2016 to 31 October 2017 in the catchment. Atmospheric deposition, litter fall and fixation  
565 show less seasonal variability. The much greater N input (the short lines in Fig 13) indicates  
566 fertilizer input in farm land, shown by a marked increase of the cumulative input occurred in  
567 the fertilizer period in May ~ early June. The greatest input results in a prolonged increase of  
568 N loading for the high discharge in the wet season from May to September in this catchment.

569 The simulated nitrification and denitrification rates of N over the study period clearly  
570 showed a seasonal variability with temperature and wetness in a year (Fig.14). The daily rates  
571 of nitrification and denitrification are much higher in wet season (0.34 and 0.21 kg N/ha for  
572 nitrification and denitrification, respectively) than in dry season (0.01 and 0.06 kg N/ha,  
573 respectively). The peaks of nitrification and denitrification occur in the fertilizer periods. The  
574 highest peaks of nitrification and denitrification rates (2.7 and 0.53 kg N/ha, respectively)  
575 correspond to the heaviest fertilization in May ~ early June.

576 The simulated annual N fluxes (including NO<sub>3</sub>-N and NH<sub>4</sub>-N) between the layers in the  
577 critical zones are shown in Fig.15. For the total input of N (1417t) from atmospheric  
578 deposition (149t), fertilizer (1220t), litter fall (42t) and fixation (6t) in the catchment during  
579 the study year, fertilizer accounts for 86 %. These inputs are mainly consumed by terrestrial  
580 plant uptake (~ 636t), accounting for about 45% of the total input of N. The remaining losses  
581 are from ammonia volatilization (~118t), denitrification (~396t), and surface channel retention  
582 (~31t), and exports from the catchment via the surface stream (58t) and underground channel  
583 (135t).

584 From the total input of N (1417t) to the soil layer, 254 t of N leaches into the underlying  
585 epikarst zone, and 97t of N is transported to the surface stream and subsurface channel, 636t  
586 of N is absorbed by plant, 278t is denitrified, and 83t is volatilized. Of the 254t of N which  
587 drains into the epikarst zone, nearly half of it (108t) is transported to the subsurface channel,  
588 118t of N is denitrified, 35t is volatilized, and only 15t drains into the deeper aquifer. The  
589 large flux of N from the epikarst to the subsurface channel results in greater annual export of  
590 N from underground channel (135t), compared to the surface stream (58t).

591

## 592 **5. Discussion**

### 593 *5.1. Uncertainty of the simulation with increased model complexity*

594 The hydrological-biogeochemical model in this study was developed by considering  
595 flow and N fluxes in the karst critical zone characterized by special geomorphologic  
596 conditions, such as fractured zone (epikarst) and sinkholes that interconnect with surface and  
597 subsurface streams. Even though there are still uncertainties for the modelling results,

598 particularly for the N simulations, the model can simulate the concurrent dynamics of  
599 hydrological, isotopic and N processes in the catchment. It was found that N loading is  
600 linearly proportional to discharge for both surface stream and underground channel at the  
601 catchment outlet (Fig.4), and thus capturing hydrological dynamics for the model, aided with  
602 detailed hydro-chemical observations, is essential for controlling the N-loading variations in  
603 this karst catchment. In order to capture hydrological dynamics and reduce uncertainties  
604 arising from increasing complexity of the model structure and associated parameterisation  
605 (e.g. increase of the vertical zones and the related parameters), we constrained hydrological  
606 module parameter ranges in the model calibration by using a combination of observations of  
607 flow discharges and isotopic concentrations. We found that although the isotope-aided model  
608 introduced two additional parameters, the detailed observations of isotopic concentrations can  
609 narrow the parameter ranges and thus reduce equifinality effect of parameters on the  
610 simulated results (Fig.7).

611 The relatively larger uncertainties of N simulations arise from increasing complexity of  
612 the model structure, and from observations of N and calibration procedures. For example, the  
613 N inputs were estimated from field surveys at some specific sites (e.g., the fertilizer and the  
614 fraction of bean production), from measurements in other areas (e.g., litter fall), and from  
615 other research (e.g., the referenced rate of annual N fixation from Smil (1999)). Even though  
616 high temporal resolution of N concentrations has been monitored at the catchment outlets,  
617 more detailed observations and field surveys of these inputs are required to reduce uncertainty  
618 in the complex hydrological and biogeochemical processes.

619 The parameter calibration in this study employs a step-wise procedure of targeting

620 simulation accuracies of outlet discharges and water stable isotope ratios for the hydrological  
621 module, and then the NO<sub>3</sub>-N concentrations for the biogeochemical module. The procedure is  
622 computationally efficient for complex model calibration in terms of the Monte Carlo  
623 framework, but it weakens interactions between hydrological and biogeochemical dynamics.  
624 In future research, simultaneous calibration of the hydrological-biogeological model  
625 parameters by combining use of hydrological observations, isotopic analysis (including N  
626 isotope analysis) and N concentrations may help further constrain the parameter ranges and  
627 reduce uncertainty of N simulations.

628

## 629 *5.2. N sources and pathways in karst landscapes*

630 Assessing N sources and transfer pathways is an evidence base for promoting efficient  
631 use of N and preventing N loss, thereby improving N management at the catchment scale  
632 (Pionke et al., 1996; Heathwaite et al., 2005; Jarvie et al., 2008, 2017; Kovacs et al., 2012).  
633 Our distributed model provides quantitative information on N sources and loads (Fig.15),  
634 which are essential for catchment managers who need to make evidence-based decisions on N  
635 pollution controls. In this catchment, about 61 % of N export occurred during the wet season,  
636 because of the large stream flow during that time. This is driven by the high water flux  
637 transporting large amounts of N from the soil reservoir into the epikarst and deep flow zone,  
638 and then into the surface and underground channels. Therefore, the quick response of water  
639 flow to rainfall usually leads to the concentrated export of N in karst catchments. Many  
640 studies have indicated that delivery times for soil water, shallow groundwater and deep  
641 groundwater to river systems range from years to decades in non-karst areas (Sanford and



642 Pope, 2013). The considerable contribution of N loading to streams from groundwater (e.g.  
643 67 % groundwater contributions to river N loading in Yongan catchment in southeast China)  
644 leads to a marked lag effect of N flux (Hu et al. 2018). However, the epikarst reservoir in the  
645 Houzhai catchment contributes the most N to the surface stream and underground channel  
646 (~45%, in Fig.15) through fractures/conduits in the karst, which implies the potential for a  
647 low hydrologic lag effect of N flux due to the high hydraulic conductivity of epikarst ( $5 \times 10^{-5}$  -  
648  $4 \times 10^{-4}$  m/s in Table 2).

649 The limited soils in karst areas are extremely important for sustaining crop and plant  
650 growth. The simulated spatial distributions of  $\text{NO}_3\text{-N}$  indicated that the main reservoirs and  
651 sources of N are located in the cultivated land of low lying plain and valley areas with  
652 relatively thick soil cover in southwest China. Meanwhile, the frequent, heavy fertilization  
653 accentuates N accumulation in the farm land, and this makes these areas the main sources of  
654 N loss during rainstorm periods. In addition, the soil properties and underlying rocks also  
655 have marked influences on N loading and export. Under the same effect of fertilization, the N  
656 loading of the soil reservoir in yellow soils in the dolostone was markedly lower than that  
657 with paddy soil in the limestone, because of the higher infiltration and percolation rates.

658 Sinkholes are another important transport and export pathway. Sinkholes sometimes  
659 function as storm drains because they directly link to the underlying aquifer systems  
660 (Tihansky, 1999). In the upstream area with more sinkholes, over 90 % of the N export was in  
661 the wet season (Yue, 2019). However, the importance of N flux through sinkholes in karst  
662 areas is a relatively under-researched topic in soil and water science.

663

664 *5.3. Implications for fertilization management in karst areas*

665 Agricultural non-point sources, such as organic and inorganic fertilizers, have been  
666 increasingly recognized as a major contributor to N pollution in catchments (Dupas et al.,  
667 2015). In many karst catchments worldwide, N fertilizer is a major contributor to aquifer  
668 contamination (Panno et al, 2001; Minet et al., 2017; Eller and Katz, 2017). In southwest  
669 China, one of the largest continuous karst areas in the world, researchers also identified  
670 agricultural activities as the predominant source of aquifer N, but found the contribution of  
671 atmospheric N to be negligible (Yang et al., 2013). Consequently, spatially and temporally  
672 targeted fertilization management is becoming more important for effective, catchment-wide  
673 reductions in N loss from land to water. The simulated N fluxes showed that the proportion of  
674 N uptake by crops was no more than 50 % of the fertilizer applied, which means there are  
675 marked N losses and/or accumulation in the karst system. Therefore, improving the efficiency  
676 of fertilization represents a priority for reducing the N losses and subsequent contamination of  
677 water. In addition, the main period of fertilizer application is usually in May in the study area  
678 (Yue et al., 2019), corresponding to the end of the dry season and beginning of the rainy  
679 season. Consequently, applied N will rapidly infiltrate to the deeper soil layers, the epikarst,  
680 and even the deep flow zone during heavy rainfall events leading to the N loss. Importantly  
681 when water levels in sub-surface conduits increase beyond sustaining the low flows from the  
682 karst aquifer, the water will flow into small fractures from conduits (Zhang et al., 2017b).  
683 Consequently, N transported will also enter the small fractures and accumulate, leading to  
684 extensive, potentially long-term contamination of the karst system. Elsewhere the karst  
685 system has been observed to delay N flux to streams during storm events and thereafter export

686 N at a more gradual rate distributed over the flood recession (Husic et al., 2018). To reduce  
687 the N loss and karst critical zone pollution (mainly in the epikarst), measures to reduce the N  
688 entering the underground system are critical for mitigating epikarst N loading, such as  
689 decreasing the N input during periods when there is strong hydraulic connectivity between  
690 soil and epikarst/deep flow zone. Therefore, fertilization may be more reasonable if timed for  
691 drier periods before the wet season starts or large storm events are forecast.

692 N management scenarios within karst catchments should not only consider the N fluxes  
693 within the surface or underground system but also the transformation of N between them via  
694 the sinkholes. Since a large number of sinkholes are located in the cultivated land of plain and  
695 valley areas, restricting fertilization around sinkholes to decrease the concentrated and fast  
696 loss of N is necessary for spatial zoning of agricultural activities.

697

## 698 **6. Conclusions**

699 Water and N transport in karst areas depend strongly on the structure of the critical zone  
700 and the karst flow system. In this study, a hydrological-biogeochemical model was developed  
701 by considering the effects of unique karstic characteristics on flow and N dynamics.

702 The model has been successfully applied in the karst catchment of Houzhai where  
703 detailed observation data of flow, stable isotopes and N concentrations, and geomorphological  
704 surveys for soil properties, fracture distribution and karst topography were available.  
705 Uncertainty analysis using Monte Carlo analysis and multi-objective calibration was used  
706 targeting initially flow and water stable isotopes, and then N simulations. Multiple sources of  
707 observations are used to identify main controlling factors of N loading, such as hydrological

708 dynamics in the catchment. The multi-objective calibration, combining discharge with water  
709 stable isotopes, can significantly constrain the parameters and reduce equifinality effect of  
710 parameters on the simulated results. The modelling results reveal functional effects of karst  
711 geomorphology and land use on spatio-temporal variations of hydrological processes and N  
712 transport, such as the large amount of N released from soil reservoirs to the epikarst (via  
713 fractures or sinkholes) and then exported to the underground channel. The modelling results  
714 also show regional differences of hydrological processes and N transport in relation to the  
715 distribution of soils, epikarst and groundwater aquifer controlled by geological conditions. In  
716 the limestone area of the south characterized by the thin soils, rich fractures and sinkholes, the  
717 flow and NO<sub>3</sub>-N loadings in the underground channel are about 2.3 and 2 times larger,  
718 respectively, than those in the north surface stream overlying the dolomite stone.

719       The large proportion of N draining into groundwater could lead to extensive, potentially  
720 long-term contamination of the karst system. Therefore, improving the efficiency of  
721 fertilization is an urgent need to reduce the N losses and contamination. It is worth noting that  
722 in karst landscapes with surrounding hills separated by star-shaped valleys, in the southwest  
723 of China, most sinkholes are distributed in the valleys covered by thick soil. These areas are  
724 often characterised by farmland, with high N inputs due to fertilizer applications. Therefore,  
725 improving agricultural management in valleys/depressions has a key role to play in reducing  
726 regional N loss and pollution in karst area.

727       The modelling indicates that uncertainty increases with model complexity and  
728 parameterisation. Strengthening the modelling capability particularly biogeochemical  
729 processes, is vital for understanding transport of N and other N components. Improvements to

730 the modelling could be achieved if supported by additional surveys of geological conditions  
731 to describe the strong heterogeneity of the karst structure in detail, and biogeochemical  
732 analysis, such as  $^{15}\text{N-NO}_3$ , to trace N sources and its transformation. Importantly, in addition  
733 to input-output observations, monitoring of hydrological and biogeochemical dynamics in  
734 different zones, such as vegetation, soils, epikarst and deep aquifer, can help adequate  
735 expressions of hydrological and biogeochemical processes in each medium and further  
736 improve the reliability of the modelling results.

737

738 **Acknowledgments.** This research was supported by The UK-China Critical Zone  
739 Observatory (CZO) Programme (41571130071/2), the National Natural Science Foundation  
740 of China (41971028, 41571020), the National Key Research and development Program of  
741 China (2016YFC0502602), and the UK Natural Environment Research Council  
742 (NE/N007468/1, NE/N007425/1). In addition, we thank the two anonymous reviewers and the  
743 editor for their constructive comments which significantly improved the manuscript.

744

## 745 **References**

- 746 Arnold, J.G., Srinivasan, R., Muttiah, R.S., Williams, J.R., 1998. LARGE AREA  
747 HYDROLOGIC MODELING AND ASSESSMENT PART I: MODEL  
748 DEVELOPMENT. *J. Am. Water Resour. Assoc.* 34, 73–89.
- 749 Barton, L., McLay, C.D.A., Schipper, L.A., Smith, C.T., 1999. Annual denitrification rates in  
750 agricultural and forest soils: a review. *Aust. J. Soil Res.* 37 (6), 1073-1093.
- 751 Bicknell, B.R., Imhoff, J.C., Kittle, J.L., Donigian, A.S., Johanson, R.C., 1993. Hydrological  
752 Simulation Program-Fortran (HSPF): User's manual for release 10.0. EPA-600/3-84-066.  
753 Environmental Research Laboratory, USEPA. Athens, GA.

- 754 Binkley, D., Cromack, K. Jr., Baker, D., 1994. Nitrogen fixation by Red Alder: biology, rates,  
755 and controls, in: Hibbs, D. (Ed.), *The Biology and Management of Red Alder*. Oregon  
756 State University Press, Corvallis. pp. 57-72.
- 757 Birkel, C., Soulsby, C., Tetzlaff, D., 2015. Conceptual modelling to assess how the interplay  
758 of hydrological connectivity, catchment storage and tracer dynamics controls  
759 nonstationary water age estimates. *Hydrol. Process.* 29, 2956–2969.
- 760 Bosch, N.S., Allan, J.D., 2008. The influence of impoundments on nutrient budgets in two  
761 catchments of Southeastern Michigan. *Biogeochemistry.* 87(3), 325–338.
- 762 Brooks, R.H., Corey, a T., 1964. Hydraulic properties of porous media, *Hydrology Papers*,  
763 Colorado State University. Pap. 3. Fort Collins CO.  
764 <https://doi:citeulike-article-id:711012>.
- 765 Chen, X., Zhang, Z., Soulsby, C., Cheng, Q., Binley, A., Jiang, R., Tao, M., 2018.  
766 Characterizing the heterogeneity of karst critical zone and its hydrological function: An  
767 integrated approach. *Hydrol. Process.* 32, 2932–2946.
- 768 Chen, X., Chen, C., Hao, Q., Zhang, Z., Shi, P., 2008. Simulation of Rainfall-Underground  
769 Outflow Responses of a Karstic Watershed in Southwest China with an Artificial Neural  
770 Network, in: *Sinkholes and the Engineering and Environmental Impacts of Karst*.  
771 American Society of Civil Engineers, Reston, VA, pp. 433–443.
- 772 Cheng, Q., 2008. Perspectives in Biological Nitrogen Fixation Research. *J. Integr. Plant Biol.*  
773 50, 786–798.
- 774 Cheng, Q., Chen, Xi, Chen, Xunhong, Zhang, Z., Ling, M., 2011. Water infiltration  
775 underneath single-ring permeameters and hydraulic conductivity determination. *J.*  
776 *Hydrol.* 398, 135–143.
- 777 David, M.B., Wall, L.G., Royer, T. V., Tank, J.L., 2006. Denitrification and the nitrogen  
778 budget of a reservoir in an agricultural landscape. *Ecol. Appl.* 16(6), 2177–2190.
- 779 Dupas, R., Delmas, M., Dorioz, J.-M., Garnier, J., Moatar, F., Gascuel-Oudou, C., 2015.  
780 Assessing the impact of agricultural pressures on N and P loads and eutrophication risk.  
781 *Ecol. Indic.* 48, 396–407.
- 782 Eller, K.T., Katz, B.G., 2017. Nitrogen Source Inventory and Loading Tool: An integrated  
783 approach toward restoration of water-quality impaired karst springs. *J. Environ. Manage.*  
784 196, 702–709.
- 785 Ferrant, S., Oehler, F., Durand, P., Ruiz, L., Salmon-Monviola, J., Justes, E., Dugast, P.,  
786 Probst, A., Probst, J.-L., Sanchez-Perez, J.-M., 2011. Understanding nitrogen transfer

- 787 dynamics in a small agricultural catchment: Comparison of a distributed (TNT2) and a  
788 semi distributed (SWAT) modeling approaches. *J. Hydrol.* 406, 1–15.
- 789 Ford, D.C., Williams, P.W., 1989. *Karst Geomorphology and Hydrology*. Unwin Hyman:  
790 London.
- 791 Godwin, D.C., Jones, C.A., Ritchie, J.T., Vlek, P.L.G., Youngdahl, L.J., 1984. The water and  
792 nitrogen components of the CERES models. *Proc. Int. Symp. Minim. Data Sets*  
793 *Agrotechnology Transf. Patancheru, India*.
- 794 Han, Z.W., Zhang, S., Wu, P., Cao, X.X., Tu, H., 2017. Distribution characteristics of  
795 nitrogen and phosphorus in waters and release flux estimation in the sediment of Caohai  
796 basin, Guizhou. *Chinese Journal of Ecology*.
- 797 Hartmann, A., Goldscheider, N., Wagener, T., Lange, J., Weiler, M., 2014. Karst water  
798 resources in a changing world: Review of hydrological modeling approaches. *Rev.*  
799 *Geophys.* 52, 218–242.
- 800 Heathwaite, A.L., Quinn, P.F., Hewett, C.J.M., 2005. Modelling and managing critical source  
801 areas of diffuse pollution from agricultural land using flow connectivity simulation. *J.*  
802 *Hydrol.* 304, 446–461.
- 803 Hénault, C., Germon, J.C., 2000. NEMIS, a predictive model of denitrification on the field  
804 scale. *Eur. J. Soil Sci.* 51, 257–270.
- 805 Hu, M., Liu, Y., Wang, J., Dahlgren, R.A., Chen, D., 2018. A modification of the Regional  
806 Nutrient Management model (ReNuMa) to identify long-term changes in riverine  
807 nitrogen sources. *J. Hydrol.* 561, 31–42.
- 808 Husic, A., Fox, J., Adams, E., Ford, W., Agouridis, C., Currens, J., Backus, J., 2019. Nitrate  
809 Pathways, Processes, and Timing in an Agricultural Karst System: Development and  
810 Application of a Numerical Model. *Water Resour. Res.* 55, 2079–2103.
- 811 Inamdar, S.P., Lowrance, R.R., Altier, L.S., Williams, R.G., Hubbard, R.K., 1999. Riparian  
812 Ecosystem Management Model (REMM): II. testing of the water quality and nutrient  
813 cycling component for a coastal plain riparian system. *Transactions of the ASAE*, 42 (6),  
814 1691-1707.
- 815 Jarvie, H.P., Johnson, L.T., Sharpley, A.N., Smith, D.R., Baker, D.B., Bruulsema, T.W.,  
816 Confesor, R., 2017. Increased Soluble Phosphorus Loads to Lake Erie: Unintended  
817 Consequences of Conservation Practices? *J. Environ. Qual.* 46, 123–132.
- 818 Jarvie, H.P., Withers, P.J.A., Hodgkinson, R., Bates, A., Neal, M., Wickham, H.D., Harman,  
819 S.A., Armstrong, L., 2008. Influence of rural land use on streamwater nutrients and their  
820 ecological significance. *J. Hydrol.* 350, 166–186.

- 821 Jones, A.L., Smart, P.L., 2005. Spatial and temporal changes in the structure of groundwater  
822 nitrate concentration time series (1935–1999) as demonstrated by autoregressive  
823 modelling. *J. Hydrol.* 310, 201–215.
- 824 Kelleher, C., Wagener, T., McGlynn, B., 2015. Model-based analysis of the influence of  
825 catchment properties on hydrologic partitioning across five mountain headwater  
826 subcatchments. *Water Resour. Res.* 51, 4109–4136.
- 827 Klimchouk, A., 2004. Towards defining, delimiting and classifying epikarst: Its origin,  
828 processes and variants of geomorphic evolution. *Speleogenes. Evol. Karst Aquifers.*
- 829 Kling, H., Fuchs, M., Paulin, M., 2012. Runoff conditions in the upper Danube basin under an  
830 ensemble of climate change scenarios. *J. Hydrol.* 424–425, 264–277.
- 831 Kovacs, A., Honti, M., Zessner, M., Eder, A., Clement, A., Blöschl, G., 2012. Identification  
832 of phosphorus emission hotspots in agricultural catchments. *Sci. Total Environ.* 433,  
833 74–88.
- 834 Kruse, S., Grasmueck, M., Weiss, M., Viggiano, D., 2006. Sinkhole structure imaging in  
835 covered Karst terrain. *Geophys. Res. Lett.* 33, L16405.
- 836 Li, C., Aber, J., Stange, F., Butterbach-Bahl, K., Papen, H., 2000. A process-oriented model  
837 of N<sub>2</sub>O and NO emissions from forest soils: 1. Model development. *J. Geophys. Res.*  
838 *Atmos.* 105, 4369–4384.
- 839 Li, C., Li, S.L., Yue, F.J., Liu, J., Zhong, J., Yan, Z.F., Zhang, R.C., Wang, Z.J., Xu, S., 2019.  
840 Identification of sources and transformations of nitrate in the Xijiang River using nitrate  
841 isotopes and Bayesian model. *Sci. Total Environ.* 646, 801–810.
- 842 Liu, C.Q., 2009. Biogeochemical processes and cycling of nutrients in the Earth's surface:  
843 Cycling of nutrients in soil–plant systems of karstic environments, Southwest China. (In  
844 Chinese) Science Press, Beijing, China.
- 845 Mahler, B.J., Garner, B.D., 2009. Using nitrate to quantify quick flow in a karst aquifer.  
846 *Ground Water.* 47(3),350-360.
- 847 McDonnell, J.J., Beven, K., 2014. Debates-The future of hydrological sciences: A (common)  
848 path forward? A call to action aimed at understanding velocities, celerities and residence  
849 time distributions of the headwater hydrograph. *Water Resour. Res.* 50, 5342–5350.
- 850 Minet, E.P., Goodhue, R., Meier-Augenstein, W., Kalin, R.M., Fenton, O., Richards, K.G.,  
851 Coxon, C.E., 2017. Combining stable isotopes with contamination indicators: A method  
852 for improved investigation of nitrate sources and dynamics in aquifers with mixed  
853 nitrogen inputs. *Water Res.* 124, 85–96.



- 854 Opsahl, S.P., Musgrove, M., Slattery, R.N., 2017. New insights into nitrate dynamics in a  
855 karst groundwater system gained from in situ high-frequency optical sensor  
856 measurements. *J. Hydrol.* 546, 179–188.
- 857 Panno, S., Hackley, K., Hwang, H., Kelly, W., 2001. Determination of the sources of  
858 nitrate contamination in karst springs using isotopic and chemical indicators. *Chem.*  
859 *Geol.* 179, 113–128.
- 860 Perrin, J., Jeannin, P.-Y., Zwahlen, F., 2003. Epikarst storage in a karst aquifer: a conceptual  
861 model based on isotopic data, Milandre test site, Switzerland. *J. Hydrol.* 279, 106–124.
- 862 Perrin, J., Jeannin, P.Y., Cornaton, F., 2007. The role of tributary mixing in chemical  
863 variations at a karst spring, Milandre, Switzerland. *J. Hydrol.* 332, 152–173.
- 864 Pi, F., 2017. Study on forest ecological stoichiometry and carbon, nitrogen and phosphorus  
865 cycle in Karst region of central Guizhou, Master's thesis, Guizhou University (in  
866 Chinese).
- 867 Pionke, H.B., Gburek, W.J., Sharpley, A.N., Schnabel, R.R., 1996. Flow and nutrient export  
868 patterns for an agricultural hill-land watershed. *Water Resour. Res.* 32, 1795–1804.
- 869 Piovano, T.I., Tetzlaff, D., Ala-aho, P., Buttle, J., Mitchell, C.P.J., Soulsby, C., 2018. Testing  
870 a spatially distributed tracer-aided runoff model in a snow-influenced catchment: Effects  
871 of multicriteria calibration on streamwater ages. *Hydrol. Process.* 32, 3089–3107.
- 872 Powers, S.M., Tank, J.L., Robertson, D.M., 2015. Control of nitrogen and phosphorus  
873 transport by reservoirs in agricultural landscapes. *Biogeochemistry.* 124(1- 3), 417–439.
- 874 Ranzini, M., Forti, M.C., Whitehead, P.G., Arcova, F.C.S., de Cicco, V., Wade, A.J., 2007.  
875 Integrated Nitrogen CAtchment model (INCA) applied to a tropical catchment in the  
876 Atlantic Forest, São Paulo, Brazil. *Hydrol. Earth Syst. Sci.* 11, 614–622.
- 877 Reddy, K.R., Khaleel, R., Overcash, M.R., Westerman, P.W., 1979. A Nonpoint Source  
878 Model for Land Areas Receiving Animal Wastes: I. Mineralization of Organic Nitrogen.  
879 *Trans. ASAE* 22, 0863–0872.
- 880 Sanford, W.E., Pope, J.P., 2013. Quantifying Groundwater's Role in Delaying Improvements  
881 to Chesapeake Bay Water Quality. *Environ. Sci. Technol.* 47, 13330–13338.
- 882 Saunders, D.L., Kalff, J., 2001. Nitrogen retention in wetlands, lakes and rivers.  
883 *Hydrobiologia.* 443(1/3), 205–212.
- 884 Schaefli, B., Gupta, H. V., 2007. Do Nash values have value? *Hydrol. Process.* 21,  
885 2075–2080.

- 886 Shaughnessy, A.R., Sloan, J.J., Corcoran, M.J., Hasenmueller, E.A., 2019. Sediments in  
887 Agricultural Reservoirs Act as Sinks and Sources for Nutrients over Various Timescales.  
888 *Water Resour. Res.* 55, 5985–6000.
- 889 Smil, V., 1999. Nitrogen in crop production: An account of global flows. *Global Biogeochem.*  
890 *Cycles* 13, 647–662.
- 891 Soulsby, C., Birkel, C., Geris, J., Dick, J., Tunaley, C., Tetzlaff, D., 2015. Stream water age  
892 distributions controlled by storage dynamics and nonlinear hydrologic connectivity:  
893 Modeling with high-resolution isotope data. *Water Resour. Res.* 51, 7759–7776.
- 894 Sprenger, M., Volkmann, T.H.M., Blume, T., Weiler, M., 2015. Estimating flow and transport  
895 parameters in the unsaturated zone with pore water stable isotopes. *Hydrol. Earth Syst.*  
896 *Sci.* 19, 2617–2635.
- 897 Thanapakpawin, P., 2007. Spatially-distributed modeling of hydrology and nitrogen export  
898 from watersheds. PHD's thesis, University of Washington
- 899 Thyer, M., Beckers, J., Spittlehouse, D., Alila, Y., Winkler, R., 2004. Diagnosing a  
900 distributed hydrologic model for two high-elevation forested catchments based on  
901 detailed stand- and basin-scale data. *Water Resour. Res.* 40.
- 902 Tihansky, A.B., 1999. Sinkholes, west-central Florida. L. Subsid. United States US Geol.  
903 *Surv. Circ.*
- 904 Wang, Z.J., Li, S.L., Yue, F.J., Qin, C.Q., Buckerfield, S., Zeng, J., 2020. Rainfall driven  
905 nitrate transport in agricultural karst surface river system: Insight from high resolution  
906 hydrochemistry and nitrate isotopes. *Agric. Ecosyst. Environ.* 291, 106787.
- 907 Wigmosta, M.S., Vail, L.W., Lettenmaier, D.P., 1994. A distributed hydrology-vegetation  
908 model for complex terrain. *Water Resour. Res.* 30, 1665–1679.
- 909 Wigmosta, M.S., Perkins, W.A., 2001. Simulating the effects of forest roads on watershed  
910 hydrology, in *Land Use and Watersheds: Human Influence on Hydrology and*  
911 *Geomorphology in Urban and Forest Areas*, Water Sci. Appl. Ser., vol. 2, edited by M.  
912 Wigmosta, and S. Burgess, pp. 127–143, AGU, Washington, D. C.
- 913 Williams, P.W., 2008. The role of the epikarst in karst and cave hydrogeology: A review. *Int.*  
914 *J. Speleol.* 37(1),1-10.
- 915 Xie, Y., Cook, P.G., Simmons, C.T., Partington, D., Crosbie, R., Batelaan, O., 2018.  
916 Uncertainty of groundwater recharge estimated from a water and energy balance model.  
917 *J. Hydrol.* 561, 1081–1093.

- 918 Yang, P., Yuan, D., Ye, X., Xie, S., Chen, X., Liu, Z., 2013. Sources and migration path of  
 919 chemical compositions in a karst groundwater system during rainfall events. *Chinese Sci.*  
 920 *Bull.* 58, 2488–2496.
- 921 Yang, Y. 2001. A study on the structure of karst aquifer medium and the groundwater flow in  
 922 Houzhai underground river basin. *Carsologica Sinica* 20(1). (In Chinese)
- 923 Yao, C.Q., 2006. Simulation of Watershed Land-Surface Hydrological Process and its  
 924 Integration with GIS. PHD's thesis, Beijing Normal University (in Chinese).
- 925 Yao, F., Sun, J., Tang, C., Ni, W., 2011. Kinetics of ammonium, nitrate and phosphate uptake  
 926 by candidate plants used in constructed wetlands, in: *Procedia Environmental Sciences.*  
 927 10, 1854-1861.
- 928 Yu, J.B., Yang, L.Z., Zhang, H.S., Fang, M.Z., Xing, F.M., 1990. The study of development  
 929 regularity of karst in China - Water resources evaluation and exploitation in karst region  
 930 in south of Puding in Guizhou Province. Science Press of China. (In Chinese).
- 931 Yue, F.J., Li, S.L., Liu, C.Q., Lang, Y.C., Ding, H., 2015. Sources and transport of nitrate  
 932 constrained by the isotopic technique in a karst catchment: an example from Southwest  
 933 China. *Hydrol. Process.* 29, 1883–1893.
- 934 Yue, F.-J., Waldron, S., Li, S.-L., Wang, Z.-J., Zeng, J., Xu, S., Zhang, Z.-C., Oliver, D.M.,  
 935 2019. Land use interacts with changes in catchment hydrology to generate chronic nitrate  
 936 pollution in karst waters and strong seasonality in excess nitrate export. *Sci. Total*  
 937 *Environ.* 696, 134062.
- 938 Zeng, J., 2018. Chemical characterization of rainwater and spatial-temporal variation of  
 939 nitrogen deposition in a small Karst catchment, Master's thesis, Guizhou University (in  
 940 Chinese).
- 941 Zhang, W., Li, Y., Zhu, B., Zheng, X., Liu, C., Tang, J., Su, F., Zhang, C., Ju, X., Deng, J.,  
 942 2018. A process-oriented hydro-biogeochemical model enabling simulation of gaseous  
 943 carbon and nitrogen emissions and hydrologic nitrogen losses from a subtropical  
 944 catchment. *Sci. Total Environ.*
- 945 Zhang, Y., Gao, Y., Yu, Q., 2017a. Diffuse nitrogen loss simulation and impact assessment of  
 946 stereoscopic agriculture pattern by integrated water system model and consideration of  
 947 multiple existence forms. *J. Hydrol.* 552, 660–673.
- 948 Zhang, Y., Shao, Q., 2018. Uncertainty and its propagation estimation for an integrated water  
 949 system model: An experiment from water quantity to quality simulations. *J. Hydrol.* 565,  
 950 623–635.

- 951 Zhang, Y.Y., Shao, Q.X., Ye, A.Z., Xing, H.T., Xia, J., 2016. Integrated water system  
952 simulation by considering hydrological and biogeochemical processes: model  
953 development, with parameter sensitivity and autocalibration. *Hydrol. Earth Syst. Sci.* 20,  
954 529–553.
- 955 Zhang, Z., Chen, X., Cheng, Q., Soulsby, C., 2019. Storage dynamics, hydrological  
956 connectivity and flux ages in a karst catchment: conceptual modelling using stable  
957 isotopes. *Hydrol. Earth Syst. Sci.* 23, 51–71.
- 958 Zhang, Z., Chen, X., Ghadouani, A., Shi, P., 2011. Modelling hydrological processes  
959 influenced by soil, rock and vegetation in a small karst basin of southwest China. *Hydrol.*  
960 *Process.* 25, 2456–2470.
- 961 Zhang, Z., Chen, X., Soulsby, C., 2017b. Catchment-scale conceptual modelling of water and  
962 solute transport in the dual flow system of the karst critical zone. *Hydrol. Process.* 31,  
963 3421–3436.
- 964 Zhang, Z., Chen, Xi, Chen, Xunhong, Shi, P., 2013. Quantifying time lag of epikarst-spring  
965 hydrograph response to rainfall using correlation and spectral analyses. *Hydrogeol. J.* 21,  
966 1619–1631.
- 967 Zhang, Z.C., Chen, X., Liu, J.T., Peng, T., Shi, P., Yan, X.L., 2012. Influence of terrain on  
968 epikarst in karst mountain- A case study of Chenqi catchment. *Earth and environment*,  
969 40(2):137-143. (In Chinese)
- 970
- 971

1  
2  
3  
4  
5  
6  
7  
8  
9  
10  
11  
12  
13  
14  
15  
16  
17  
18  
19  
20  
21

Table 1 Statistical summary of discharge, water stable isotope data, NO<sub>3</sub>-N concentration at surface stream and underground channel outlets.

Obs	Surface Stream					Underground Channel				
	Max	Min	Mean	Mode	CV	Max	Min	Mean	Mode	CV
Discharge (m <sup>3</sup> /s)	6.87	0.01	0.32±0.11	0.05	2.69	3.13	0.21	0.79±0.06	1.38	0.63
δD (‰)	-33.7	-77.6	-57.2±0.5	-48.2	0.1	-42	-71.5	-57.4±0.5	-58.8	0.07
NO <sub>3</sub> -N (mg/L)	10.71	0.72	3.15±0.25	3.44	0.48	9.78	2.47	4.13±0.33	3.98	0.21

CV: Coefficient of Variation; ± refers to measured errors

22

23

24 Table 2 Ranges of hydrological parameters and fractionation coefficients for random  
 25 sampling. (\* represents the initial range for the first sampling). The values in brackets  
 26 represent the mean of the best 114 parameter sets after calibration.

	Parameter	Range		Parameter	Range
Yellow soil	$K_h$ (m/s)	$1 \times 10^{-6} - 1 \times 10^{-4} *$ $5 \times 10^{-6} - 5 \times 10^{-5}$ ( $2 \times 10^{-5}$ )	Epikarst	$K_h$ (m/s)	$1 \times 10^{-5} - 1 \times 10^{-3} *$ $2 \times 10^{-5} - 2 \times 10^{-4}$ ( $5 \times 10^{-5}$ )
	$K_v$ (m/s)	$1 \times 10^{-6} - 1 \times 10^{-4} *$ $2 \times 10^{-6} - 2 \times 10^{-5}$ ( $1 \times 10^{-5}$ )		$K_v$ (m/s)	$1 \times 10^{-5} - 1 \times 10^{-3} *$ $7 \times 10^{-5} - 6 \times 10^{-4}$ ( $4 \times 10^{-4}$ )
	$\theta_f$	0.1 – 0.5 * 0.2 – 0.37 (0.35)		$\theta_f$	0.01 – 0.15 * 0.01 – 0.1 (0.02)
Paddy soil	$K_h$ (m/s)	$1 \times 10^{-7} - 5 \times 10^{-5} *$ $3 \times 10^{-6} - 2 \times 10^{-5}$ ( $1 \times 10^{-5}$ )	Deep flow zone	$K_h$ (m/s)	$1 \times 10^{-7} - 1 \times 10^{-5} *$ $3 \times 10^{-6} - 8 \times 10^{-6}$ ( $4 \times 10^{-6}$ )
	$K_v$ (m/s)	$1 \times 10^{-7} - 5 \times 10^{-5} *$ $1 \times 10^{-6} - 1 \times 10^{-5}$ ( $9 \times 10^{-6}$ )		$K_v$ (m/s)	$1 \times 10^{-7} - 1 \times 10^{-5} *$ $2 \times 10^{-6} - 9 \times 10^{-6}$ ( $3 \times 10^{-6}$ )
	$\theta_f$	0.1 – 0.5 * 0.25 – 0.42 (0.38)		$\theta_f$	0.01 – 0.15 * 0.01 – 0.05 (0.01)
Lime-stone soil	$K_h$ (m/s)	$1 \times 10^{-6} - 5 \times 10^{-4} *$ $1 \times 10^{-5} - 1 \times 10^{-4}$ ( $6 \times 10^{-5}$ )	Forest		0.5 – 1 * 0.6 – 0.9 (0.85)
	$K_v$ (m/s)	$1 \times 10^{-6} - 5 \times 10^{-4} *$ $1 \times 10^{-5} - 8 \times 10^{-5}$ ( $4 \times 10^{-5}$ )	Farm land	$C_f$	0.5 – 1 * 0.5 – 0.9 (0.6)
	$\theta_f$	0.1 – 0.5 * 0.15 – 0.31 (0.18)			
Fractionation coefficient	$\tau_s$	1 – 5 * 1 – 3 (2.8)		$\tau_e$	1 – 5 * 1 – 2 (1.6)

27

28

29

30

31

32  
33  
34  
35  
36  
37  
38  
39  
40  
41  
42  
43  
44  
45  
46  
47  
48  
49  
50  
51  
52  
53  
54  
55  
56  
57  
58  
59  
60  
61  
62  
63  
64  
65

Table 3 Calibrated parameters for biogeochemical reaction of N.

Parameters	Forest	Farm land	Soil & Epikarst		Surface channel			
$N_f$ (kg/ ha-yr)	-	40	$D_{st}$	0.6	$\emptyset$	0.35		
$Num$ (day)	180	160	$R_{hs}$	0.5				
$Nam$ (mg /m <sup>2</sup> )	3000	800	$O_t$	5				
$Au$ (kg)	$3.6 \times 10^{-3}$	$3.7 \times 10^{-3}$	$N_a$	L-s	0	L-s	0.01	
$Aum$ (kg)	$3.9 \times 10^{-4}$	$4.02 \times 10^{-4}$		P-s	0.01	$A_a$	P-s	0.03
$C/N$	25	40		Y-s	0.01		Y-s	0.03

L-s: Limestone soil, P-s: Paddy soil, Y-s: Yellow soil.

66 Table 4 Performance metrics of discharge,  $\delta D$  and  $[NO_3-N]$  for surface stream and  
 67 underground channel at catchment outlet.

Performance metrics		Surface stream			Underground channel		
		Discharge	$\delta D$	$[NO_3-N]$	Discharge	$\delta D$	$[NO_3-N]$
RMSE	Max	0.39	10.9	-	0.35	7.6	-
	Min	0.23	5.7	-	0.21	3.5	-
	Mean	0.31	8.9	1.06	0.28	5.6	0.37
aARE	Max	0.16	0.19	-	0.13	0.16	-
	Min	0.06	0.08	-	0.04	0.06	-
	Mean	0.10	0.12	0.14	0.07	0.11	0.12
KGE	Max	0.80	0.65	-	0.82	0.7	-
	Min	0.70	0.44	-	0.72	0.51	-
	Mean	0.77	0.53	0.45	0.78	0.61	0.5

68 RMSE represents root mean squared error ( $m^3/s$ , ‰ and mg/L for discharge, deuterium ratio and  $[NO_3-N]$ ,  
 69 respectively), aARE represents the absolute of average relatively error, and KGE represents efficiency.

70

71

72



Figure captions

- 1
- 2 Figure 1 Topography, surface stream and underground channel network, and sinkhole  
3 location in Houzhai watershed. The size of dots represents the drainage area controlled by  
4 sinkholes and the black number represents the sinkholes in the eastern mountainous area.  
5
- 6 Figure 2 Distribution of karstic critical zone structure for land use/cover (a), soils (b), epikarst  
7 (c), and aquifer geology (d) in Houzhai catchment.  
8
- 9 Figure 3 Time series of rainfall, discharge (Q),  $\delta D$  and  $[NO_3-N]$  of surface stream (S) and  
10 underground channel (U) at the watershed outlets.  
11
- 12 Figure 4 Relationship between daily  $NO_3-N$  loading and discharge for surface stream (S) and  
13 underground channel (U) at the catchment outlets.  
14
- 15 Figure 5 Dual-isotope plot showing the flow water isotope data at catchment outlet.  
16
- 17 Figure 6 Schematic representation of the distributed hydrological-N model in karst watershed  
18 (D-SEMK).  $Q_{sur}$ : overland flow;  $Q_s$ : subsurface flow in soil zone;  $Q_e$ : subsurface flow in  
19 epikarst zone;  $Q_d$ : flow in deep flow zone;  $Q_{sinkhole}$ : flow draining through sinkholes into  
20 underground conduit; N: nutrient concentration.  
21
- 22 Figure 7 The simulated and observed discharges at surface stream outlet (a) and underground  
23 channel outlet (b) over the study period. Note: Observations are shown with black symbols  
24 while the red line displays mean of the simulations for the 114 retained parameter sets after  
25 calibration.  
26
- 27 Figure 8 The simulated and observed deuterium ratio in the surface stream (a) and  
28 underground channel outlets (b) over the study period. Note: Measurements are shown with  
29 black symbols while the red line displays mean of the simulations for the remaining  
30 parameter sets.  
31
- 32 Figure 9 Comparison of the calibrated parameters for hydrological module that the discharge  
33 target meets  $KGE_Q \geq 0.75$  and the combination target of discharge and isotopic  
34 concentration meets  $KGE_Q \geq 0.75$  and  $KGE_i \geq 0.5$ .  
35
- 36 Figure 10 The simulated and observed  $NO_3-N$  concentrations (a) and the correlation between  
37 them (b) for surface stream and underground channel over the study period.  
38
- 39 Figure 11 The simulated and measured  $NH_4-N$  concentrations at surface stream (a) and  
40 underground channel (b) over the study period.  
41
- 42 Figure 12 The simulated spatial distribution of mean  $NO_3-N$  loadings in each layer during the

43 study period in Houzhai catchment. (a) soil layer, (b) epikarst, (c) deep flow zone, and (d)  
44 the annual  $\text{NO}_3\text{-N}$  loading in each store with different land cover.

45

46 Figure 13 Daily (a) and cumulative (b) inputs and losses of N from Houzhai catchment.

47

48 Figure 14 Simulated daily nitrification and denitrification of N

49

50 Figure 15 Simulated annual N fluxes and loadings in each modelled reservoir. The karst  
51 system of the catchment is in the dotted wire frame. Red hollow arrows represent the  
52 annual N flux into and out the system. The coloured solid arrows represent the annual N  
53 flux within the karst system. Note: **Ap**: Atmospheric deposition; **Fer**: Fertilizer; **Lit**: Litter  
54 Fall; **Fix**: Fixation; **Av**: Ammonia volatilization; and **Ret**: Surface channel retention.

55

56

57

58

59

60

61

62

63

64

65

66

67

68

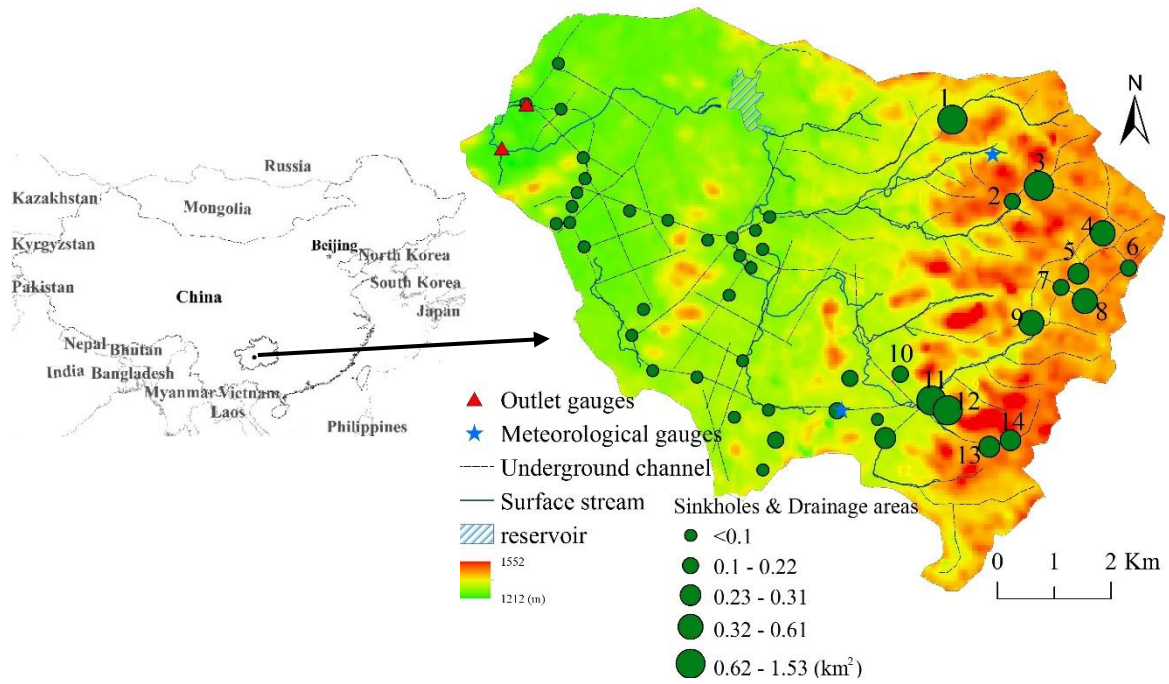
69

70

71

72

73



74

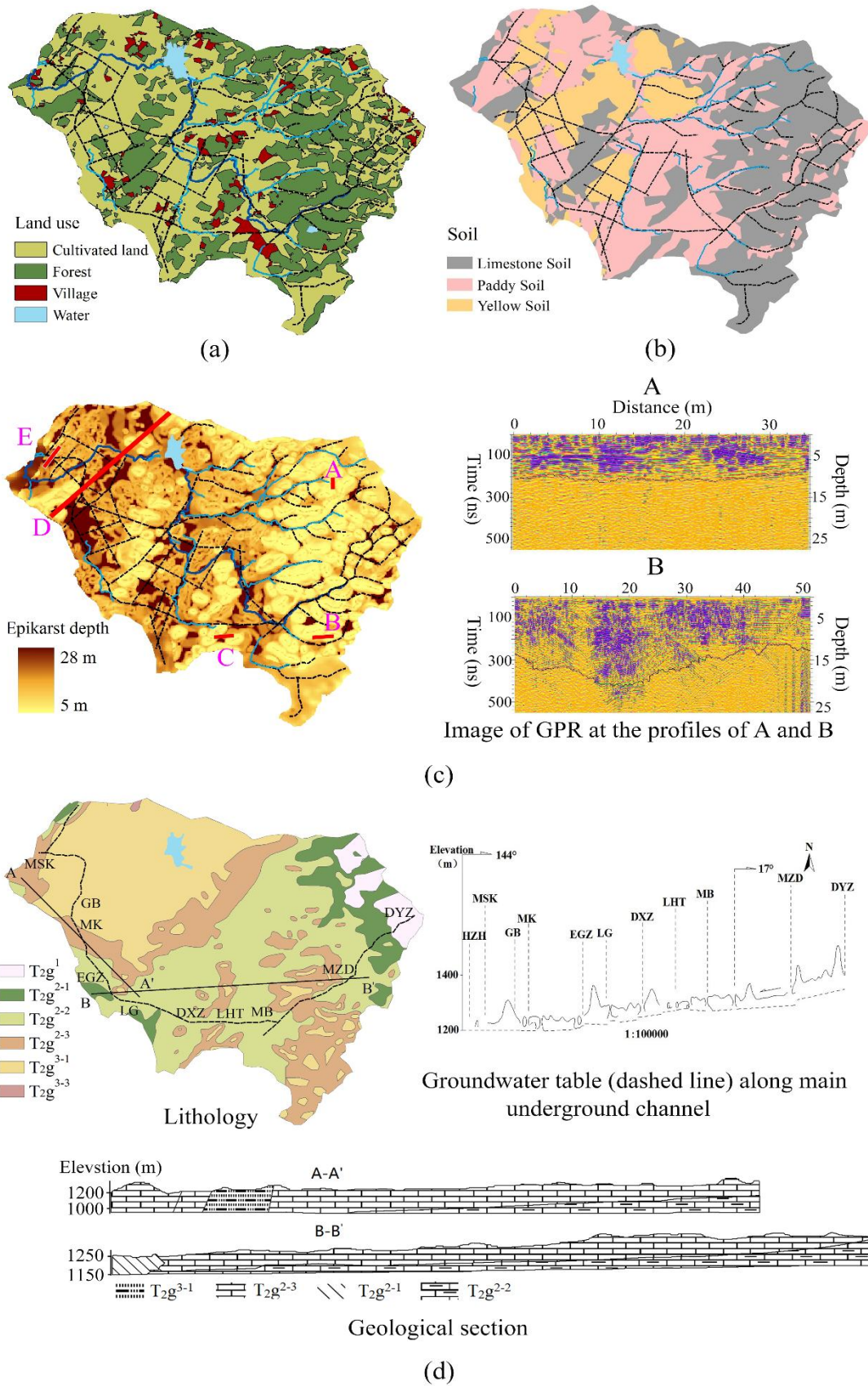
75

76

77

78

Figure 1 Topography, surface stream and underground channel network, and sinkhole location in Houzhai watershed. The size of dots represents the drainage area controlled by sinkholes and the black number represents the sinkholes in the eastern mountainous area.



79

80 Figure 2 Distribution of karstic critical zone structure for land use/cover (a), soils (b), epikarst

81

(c), and aquifer geology (d) in Houzhai catchment.

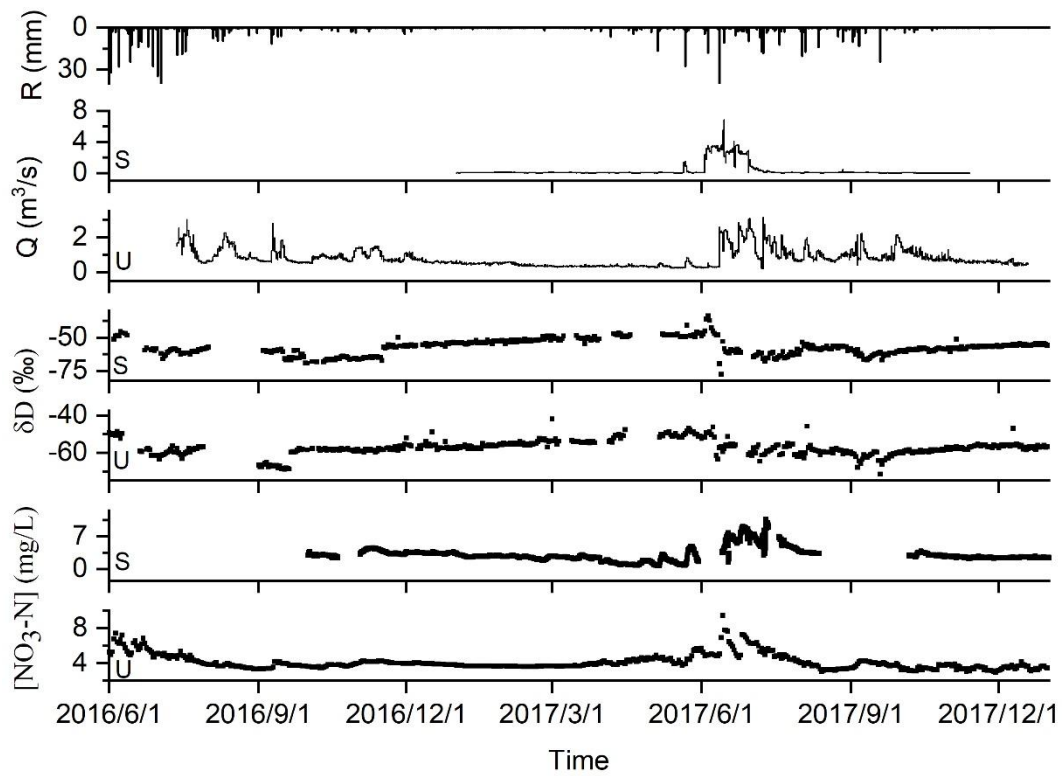
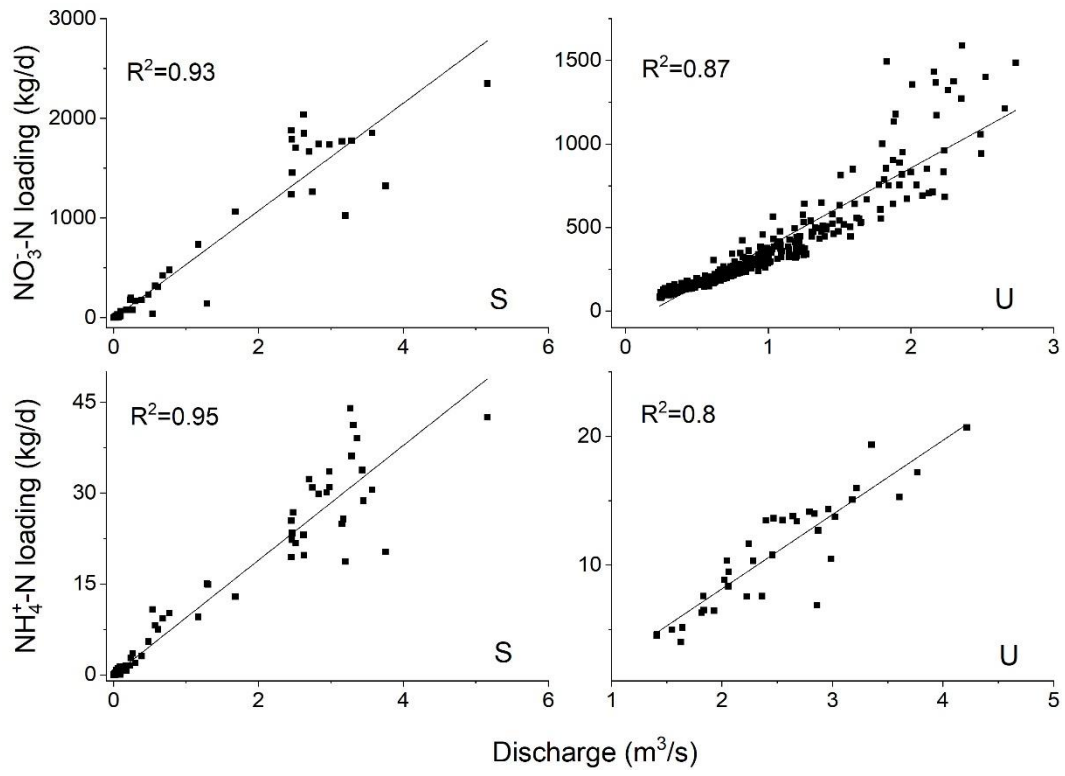


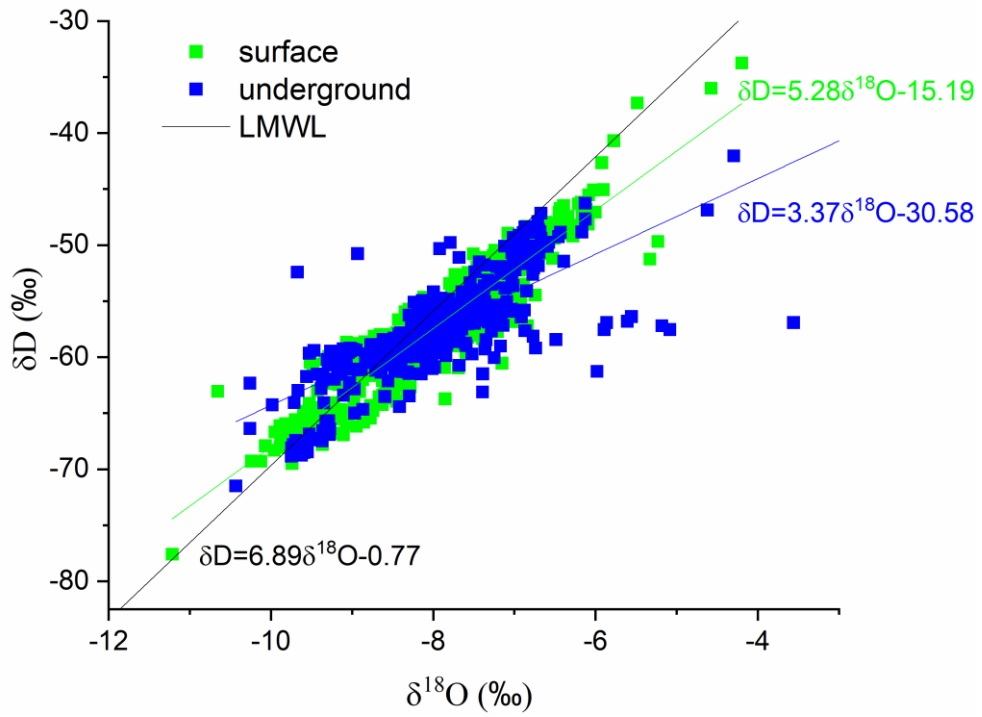
Figure 3 Time series of rainfall, discharge (Q),  $\delta D$  and  $[NO_3-N]$  of surface stream (S) and underground channel (U) at the watershed outlets.

82  
83  
84  
85  
86  
87  
88  
89  
90  
91  
92  
93  
94  
95  
96  
97  
98  
99  
100



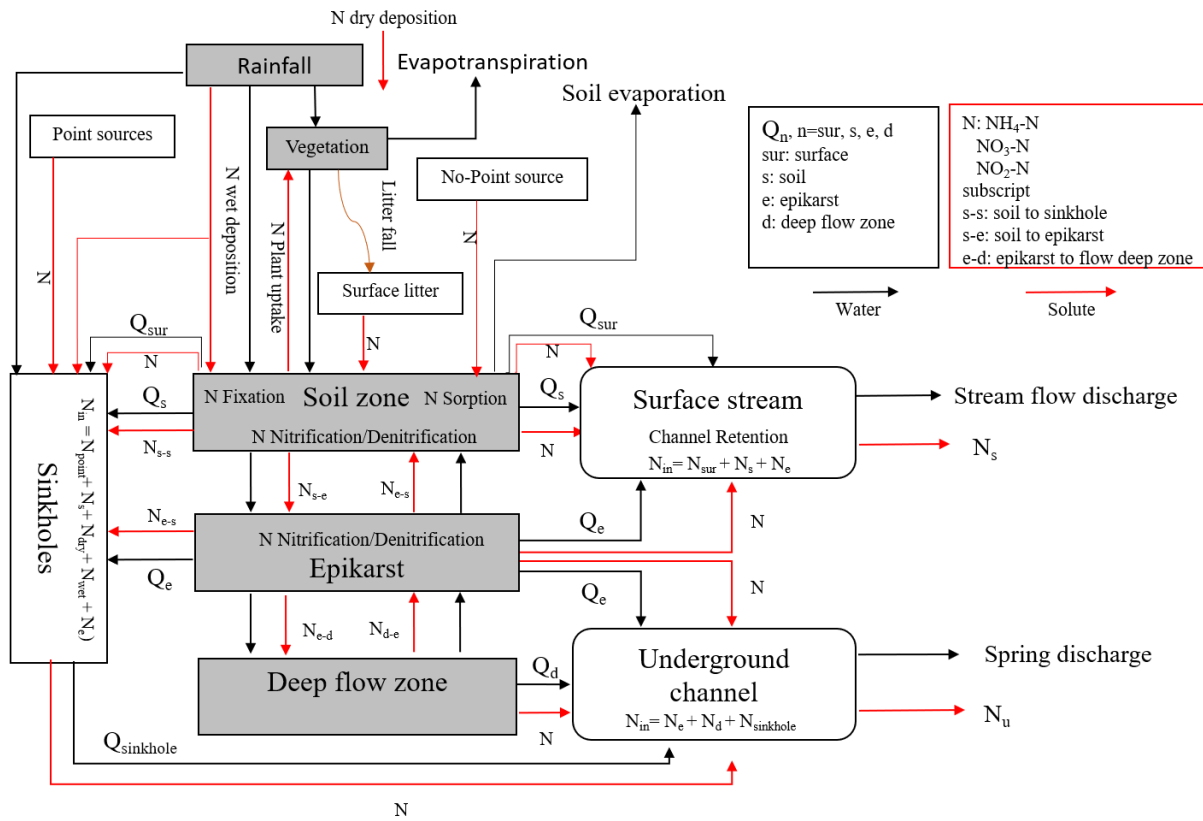
101  
 102  
 103  
 104  
 105  
 106  
 107  
 108  
 109  
 110  
 111  
 112  
 113  
 114  
 115  
 116  
 117  
 118  
 119  
 120  
 121  
 122

Figure 4 Relationship between daily  $\text{NO}_3\text{-N}$  loading and discharge for surface stream (S) and underground channel (U) at the catchment outlets.



123  
 124  
 125  
 126  
 127  
 128  
 129  
 130  
 131  
 132  
 133  
 134  
 135  
 136  
 137  
 138  
 139  
 140  
 141  
 142  
 143  
 144  
 145  
 146  
 147  
 148  
 149

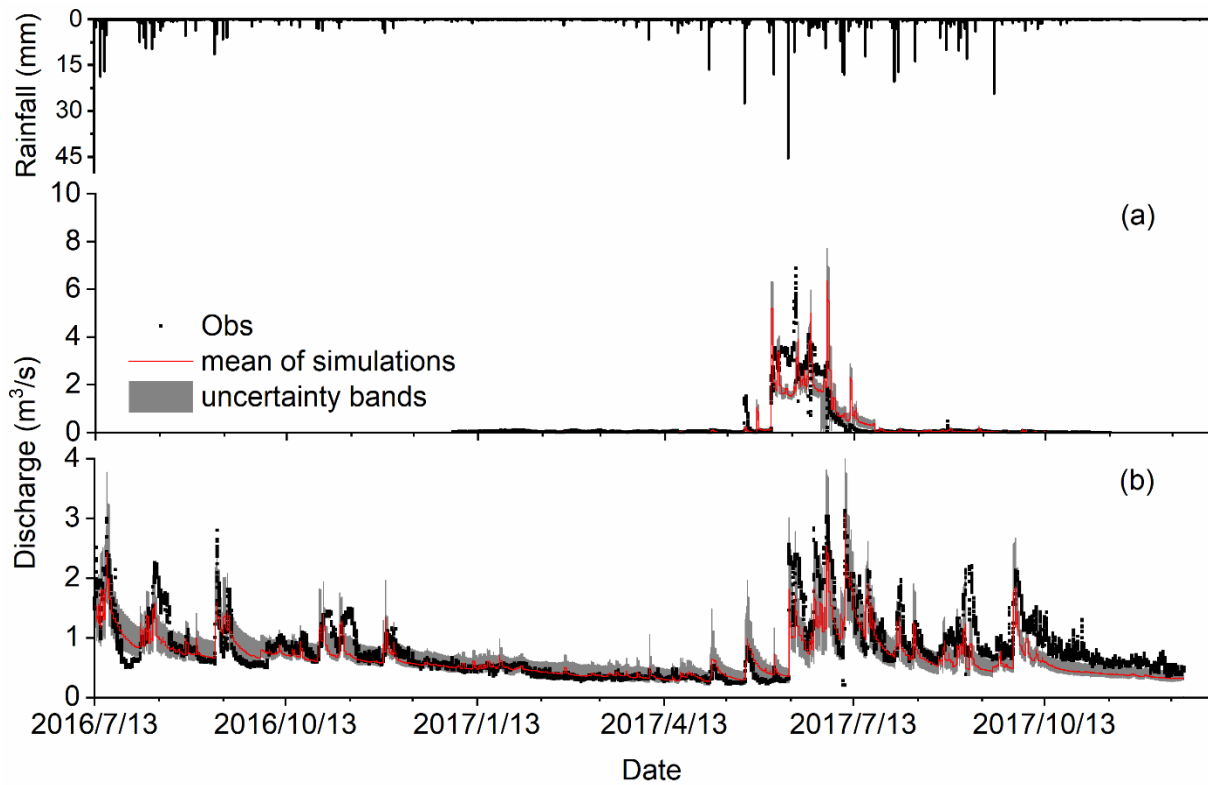
Figure 5 Dual-isotope plot showing the flow water isotope data at catchment outlet.



151  
 152  
 153  
 154  
 155  
 156  
 157  
 158  
 159  
 160  
 161  
 162

Figure 6 Schematic representation of the distributed hydrological-N model in karst watershed (D-SEMK).  $Q_{sur}$ : overland flow;  $Q_s$ : subsurface flow in soil zone;  $Q_e$ : subsurface flow in epikarst zone;  $Q_d$ : flow in deep flow zone;  $Q_{sinkhole}$ : flow draining through sinkholes into underground conduit;  $N$ : nutrient concentration.





163

164

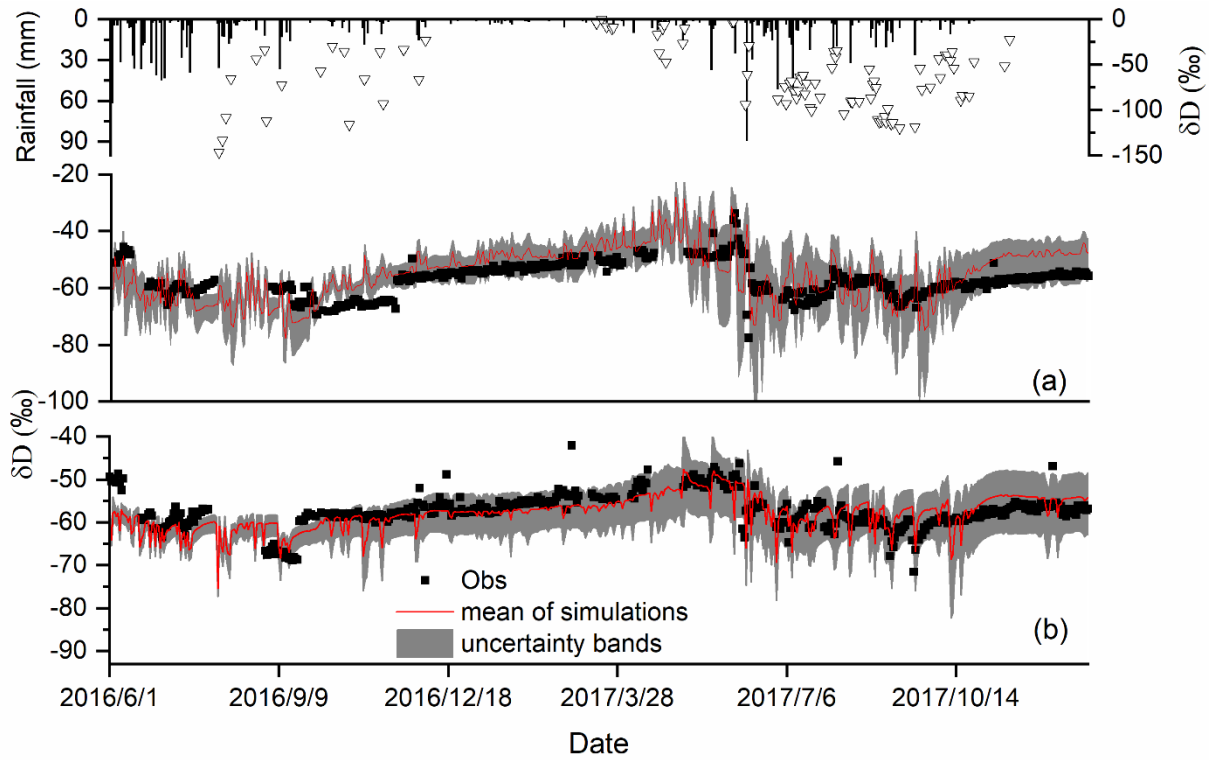
165 Figure 7 The simulated and observed discharges at surface stream outlet (a) and underground  
 166 channel outlet (b) over the study period. Note: Observations are shown with black symbols  
 167 while the red line displays mean of the simulations for the 114 retained parameter sets after  
 168 calibration.

169

170

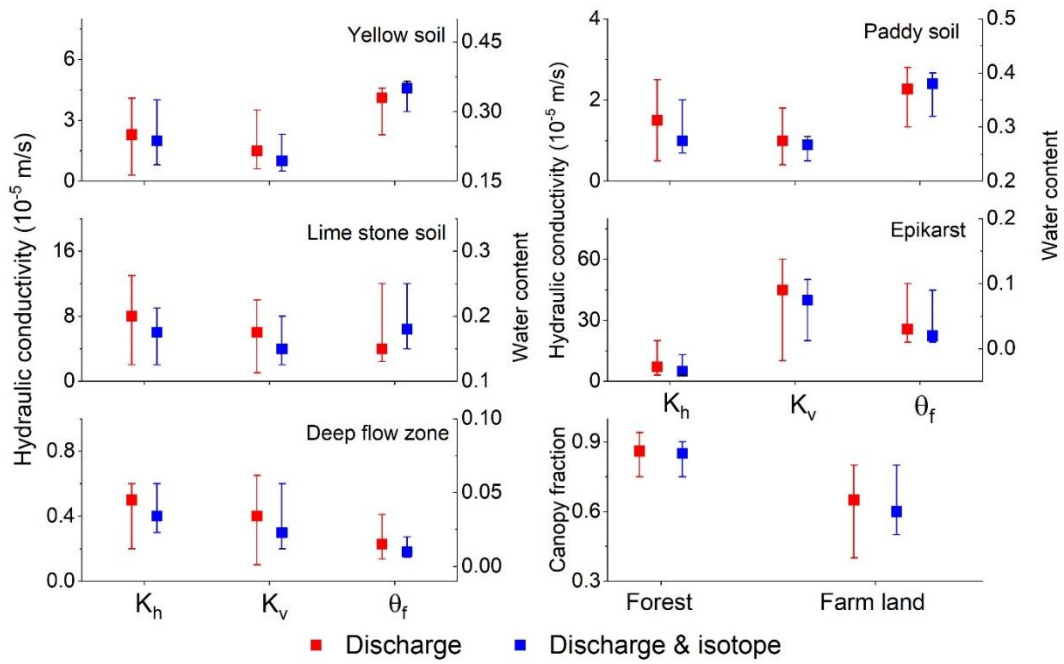
171

172



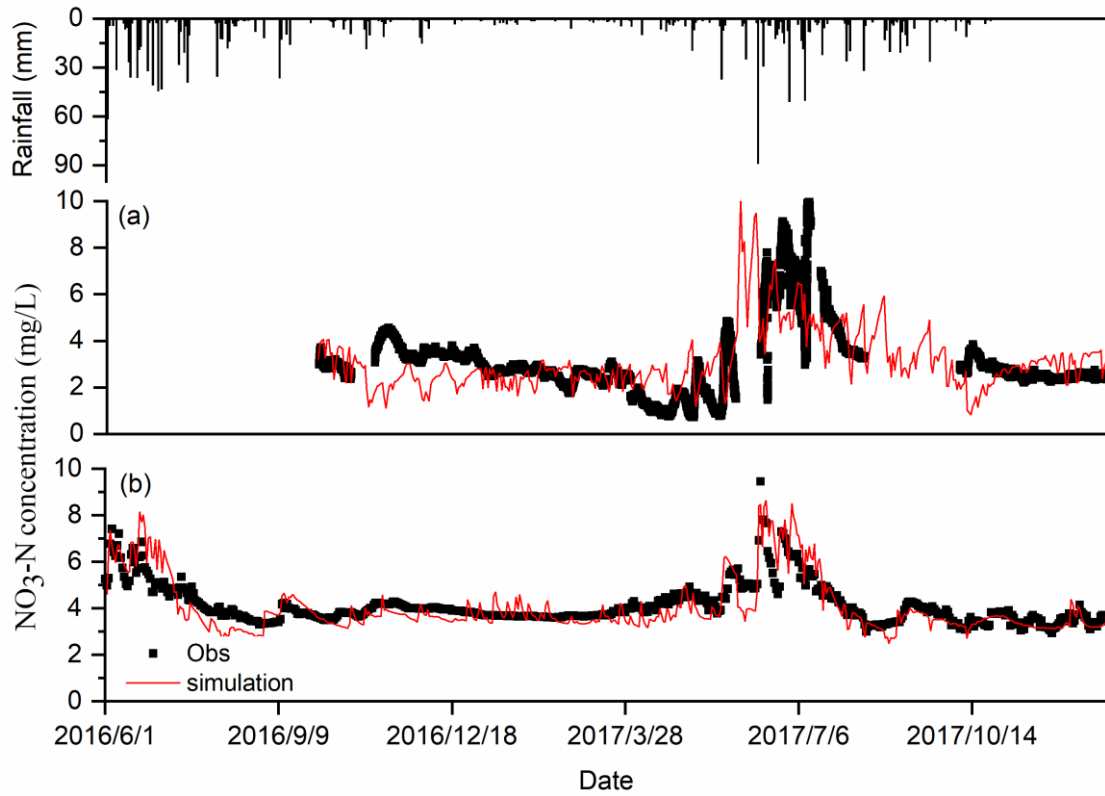
173  
 174  
 175  
 176  
 177  
 178  
 179  
 180  
 181  
 182  
 183  
 184  
 185  
 186  
 187  
 188  
 189  
 190

Figure 8 The simulated and observed deuterium ratio in the surface stream (a) and underground channel outlets (b) over the study period. Note: Measurements are shown with black symbols while the red line displays mean of the simulations for the remaining parameter sets.

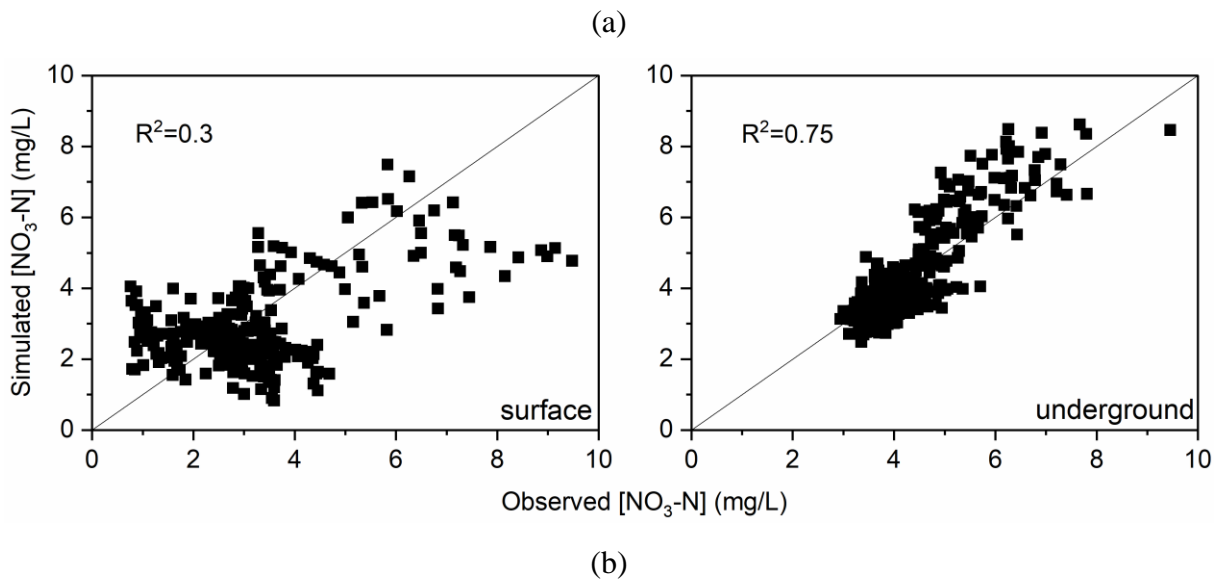


191  
 192  
 193  
 194  
 195  
 196  
 197  
 198  
 199  
 200  
 201  
 202  
 203  
 204  
 205  
 206

Figure 9 Comparison of the calibrated parameters for hydrological module that the discharge target meets  $KGE_Q \geq 0.75$  and the combination target of discharge and isotopic concentration meets  $KGE_Q \geq 0.75$  and  $KGE_i \geq 0.5$ .

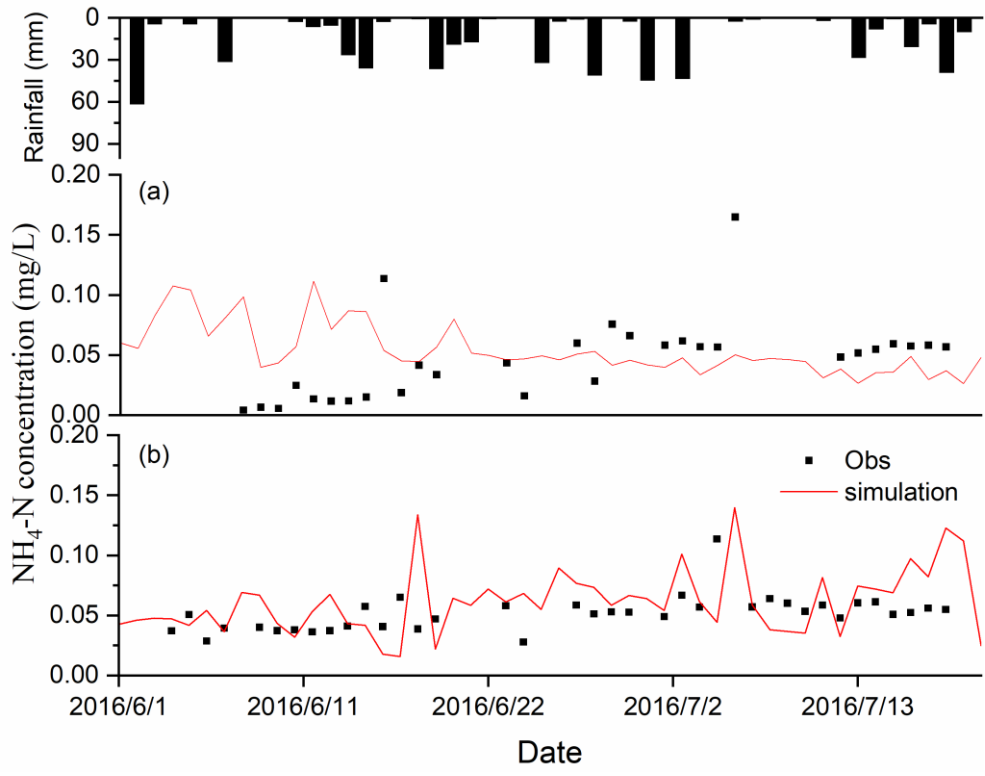


207  
208



209  
210  
211  
212  
213  
214

Figure 10 The simulated and observed  $\text{NO}_3\text{-N}$  concentrations (a) and the correlation between them (b) for surface stream and underground channel over the study period.



215

216

217 Figure 11 The simulated and measured NH<sub>4</sub>-N concentrations at surface stream (a) and  
 218 underground channel (b) over the study period.

219

220

221

222

223

224

225

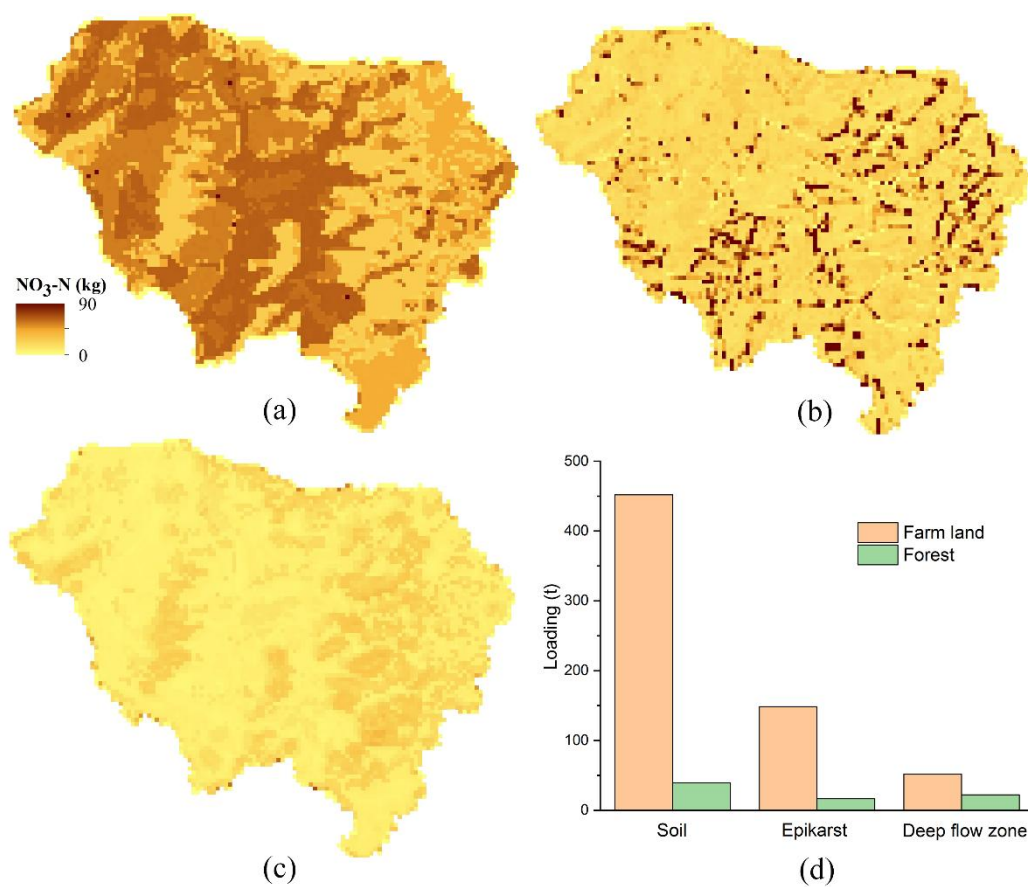
226

227

228

229

230



231

232

233 Figure 12 The simulated spatial distribution of mean NO<sub>3</sub>-N loadings in each layer during the  
234 study period in Houzhai catchment. (a) soil layer, (b) epikarst, (c) deep flow zone, and (d)  
235 the annual NO<sub>3</sub>-N loading in each store with different land cover.

236

237

238

239

240

241

242

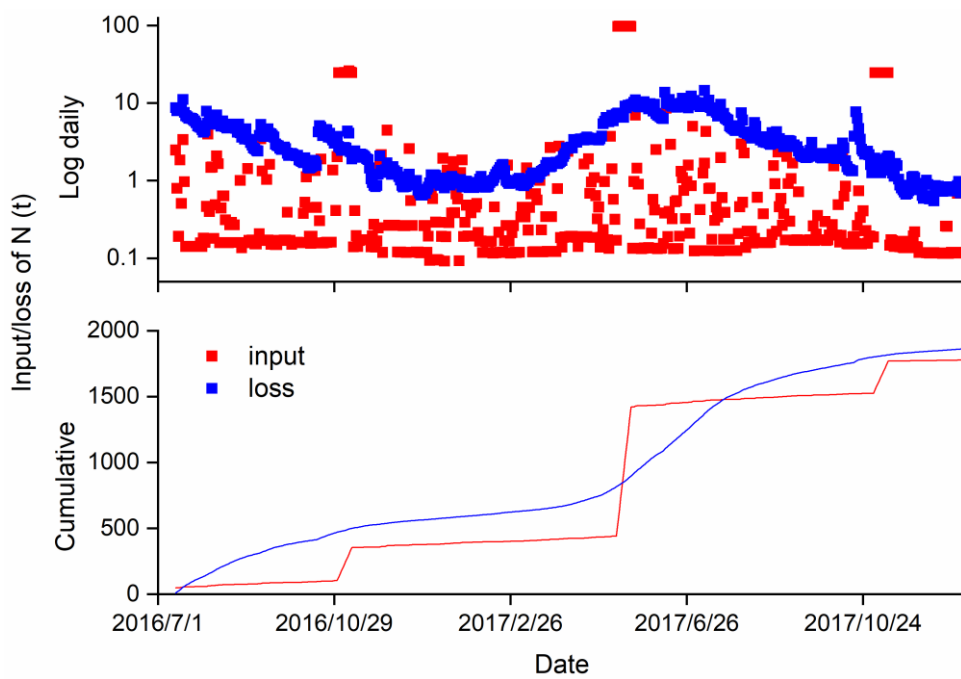
243

244

245

246

247



248

249

250 Figure 13 Daily (a) and cumulative (b) inputs and losses of N from Houhzai catchment.

251

252

253

254

255

256

257

258

259

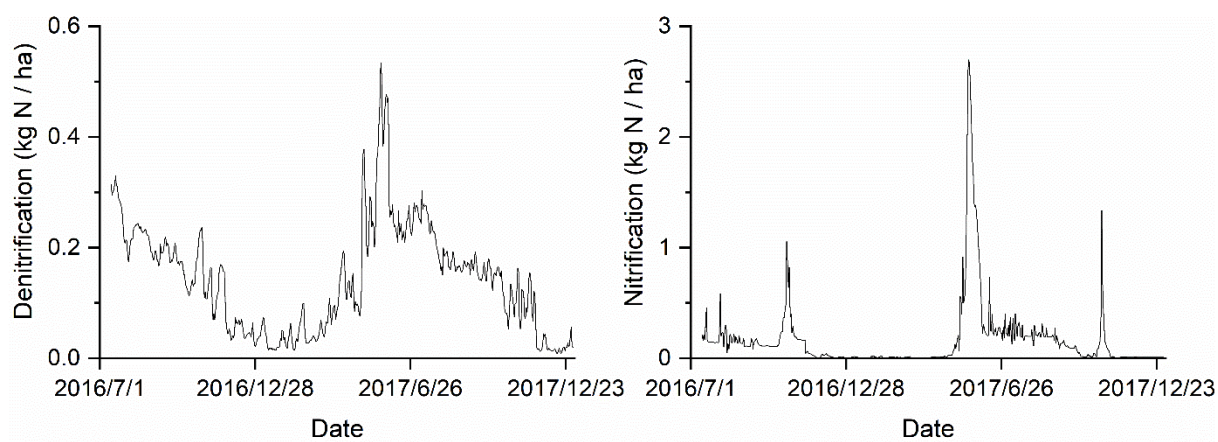
260

261

262

263

264



265

266

Figure 14 Simulated daily nitrification and denitrification of N

267

268

269

270

271

272

273

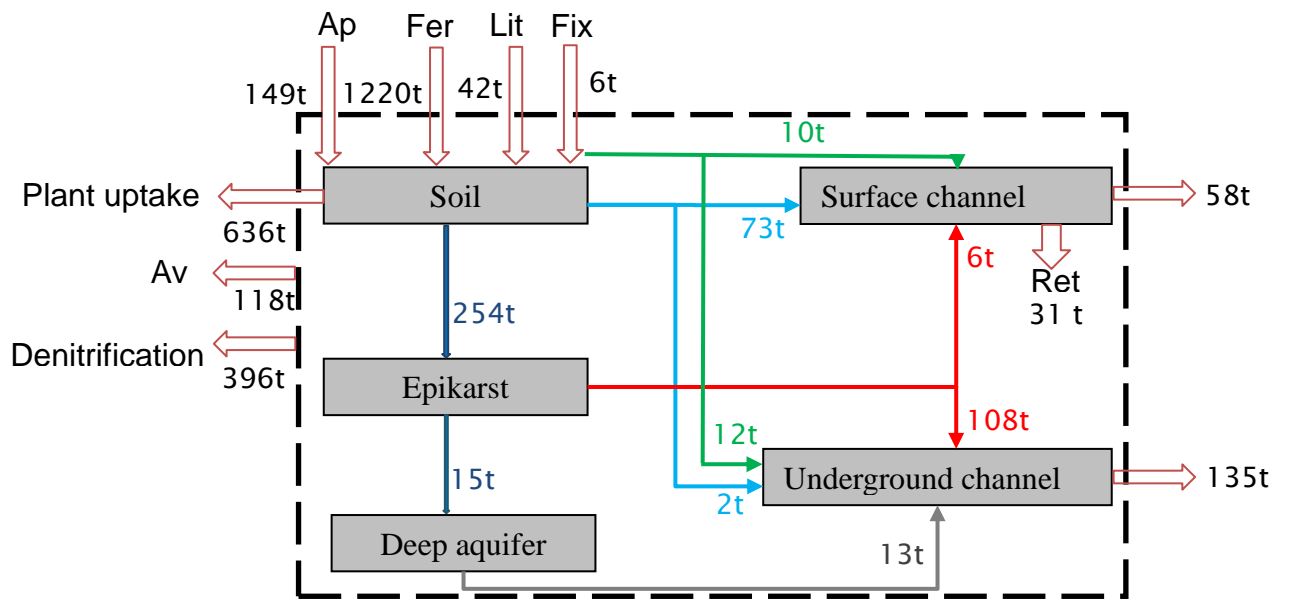
274

275

276



277  
 278  
 279  
 280  
 281



282  
 283  
 284  
 285  
 286  
 287  
 288  
 289  
 290  
 291  
 292  
 293  
 294  
 295

Figure 15 Simulated annual N fluxes and loadings in each modelled reservoir. The karst system of the catchment is in the dotted wire frame. Red hollow arrows represent the annual N flux into and out the system. The coloured solid arrows represent the annual N flux within the karst system. Note: **Ap**: Atmospheric deposition; **Fer**: Fertilizer; **Lit**: Litter Fall; **Fix**: Fixation; **Av**: Ammonia volatilization; and **Ret**: Surface channel retention.

**Declaration of interests**

The authors declare that they have no known competing financial interests or personal relationships that could have appeared to influence the work reported in this paper.

The authors declare the following financial interests/personal relationships which may be considered as potential competing interests:

**Zhikai Zhang:** Conceptualization, Methodology, Software, Writing - Original Draft; **Xi Chen:** Conceptualization, Writing- Reviewing and Editing, Supervision; **Qinbo Cheng:** Investigation, Data curation; **Siliang Li:** Validation, Conceptualization; **Fujun Yue** and **Tao Peng:** Data curation, Resources; **Susan Waldron** and **David Oliver:** Writing- Reviewing and Editing, Visualization; **Chris Soulsby:** Writing- Reviewing and Editing, Supervision.